Aachener Verfahrenstechnik Series
AVT.CVT – Chemical Process Engineering
Volume 23 (2022)

Franziska Maria Dorothee Gertrud Hagemann

Model Based Design and Optimization of High Capacitive Membrane Adsorbers

DOI: 10.18154/RWTH-2022-00218

Model Based Design and Optimization of High Capacitive Membrane Adsorbers

Modellbasiertes Design und Optimierung von hochkapazitiven Membranadsorbern

Von der Fakultät für Maschinenwesen der Rheinisch-Westfälischen Technischen Hochschule Aachen zur Erlangung des akademischen Grades einer Doktorin der Ingenieurwissenschaften genehmigte Dissertation

vorgelegt von

Franziska Maria Dorothee Gertrud Hagemann

Berichter/in:
Univ.-Prof. Dr.-Ing. Matthias Wessling
Assoc. Prof. Dr.-Ing. Cristiana Boi

Tag der mündlichen Prüfung: 11.10.2021

Parts of this dissertation have been published. Reproduced from:

Franziska Hagemann, Patrick Adametz, Matthias Wessling, Volkmar Thom
Modeling hindered diffusion of antibodies in agarose beads considering pore size reduction due to adsorption,
Journal of Chromatography A, 2020 DOI: 10.1016/j.chroma.2020.461319

Franziska Hagemann, Denis Wypysek, Kristina Baitalow, Patrick Adametz, Volkmar Thom, Matthias Wessling
Why device design is crucial for membrane adsorbers,
Journal of chromatography open, 2021 DOI: 10.1016/j.jcoa.2021.100029

Titel: Model Based Design and Optimization of High Capacitive Membrane Adsorbers

Author: Franziska Maria Dorothee Gertrud Hagemann

Reihe: Aachener Verfahrenstechnik Series
AVT.CVT - Chemical Process Engineering
Volume: 23 (2022)

Herausgeber: Aachener Verfahrenstechnik
Forckenbeckstraße 51
52074 Aachen
Tel.: +49 (0)241 8097717
Fax.: +49 (0)241 8092326
E-Mail: secretary.cvt@avt.rwth-aachen.de
http://www.avt.rwth-aachen.de/AVT

Volltext verfügbar: 10.18154/RWTH-2022-00218

Acknowledgement

An dieser Stelle möchte ich bei allen bedanken, die mich beim Gelingen dieser Doktorarbeit unterstützt haben.

Mein besonderer Dank gilt meinem Doktorvater, Prof. Dr.-Ing. Matthias Wessling, für seine ausgezeichnete Unterstützung aus der Ferne und die produktiven Gespräche.

Ich danke der Firma Sartorius, insbesondere meinem Mentor Dr. Dieter Melzner für seine persönliche Förderung und das Schaffen einer Promotionsstelle. Außerdem möchte ich mich bei meinen Vorgesetzten Dr. Louis Villain und Dr. Volkmar Thom für ihre hervorragende Unterstützung und das kooperative Klima bedanken.

Für den außerordentlich guten fachlichen Austausch möchte ich Patrick danken! Danke auch dafür, dass Du immer Zeit gefunden hast. Für den Zugang zu CFD Simulationen möchte ich mich bei meinem Kollegen Christian Becker bedanken. Der Gruppe von Eric von Lieres möchte ich für ihre Hilfe mit CADET danken. Sam, Juliane und Will - ohne Euch hätte die Einarbeitung wesentlich länger gedauert. Außerdem möchte ich meinen Kollegen bei Sartorius und an der CVT meinen Dank aussprechen, die mich mit vielen Tipps, produktiven Gesprächen und tollen Anregungen begleitet haben.
Ein großes Dankeschön an die Praktikanten und Abschlussarbeiter, die ich während meiner Promotionszeit betreut habe. Durch Euch hatte ich die Möglichkeit weiter über den Tellerrand zu gucken und noch tiefer in die Materie zu gehen.

Meinen Eltern, meinen Verwandten und meinen Freunden danke ich. Euer Rückhalt während meiner Zeit in Göttingen war unglaublich wichtig für mich. Danke, Maik, für Deine Unterstützung und die kritischen Fragen, die mich an mancher Stelle weiter gebracht haben.

Be less curious about people and more curious about ideas.

- Marie Curie

Contents

Abstract

In order to isolate cell derived target molecules from the respective fermentation broth, faster and more efficient unit operations are required. Due to mass transfer limitations, resin chromatography typically shows a strong dependence of the binding capacity on the residence time and is therefore limited in separation velocity. Small particles cause thinner convective channels and therefore create a higher pressure drop over the chromatographic bed.
Convective chromatography e.g. based on membranes, is a promising approach, representing nearly residence time independent separation processes with respect to the binding capacity, yielding high process productivity. Due to the inherent structural properties of purely convective separation media, the specific surface area and thus the binding capacity often become limiting factors.
Membrane adsorbers with a biporous structure can improve the downstream process in bioprocesses, because mass transfer limitations are drastically reduced compared to conventional resin chromatography materials. Convective pores enable fast mass transfer and diffusive pores in the membrane bridges provide surface for binding. The diffusive pathways in membranes are much smaller than conventional bead diameters, allowing higher flow rates in the process.
The aim of this thesis is the model based optimization of such membrane adsorbers. The membrane is optimized regarding bed height, convective porosity, permeability, diffusive pore structure and the length of diffusive pathway. The impact of the target molecule size and the flow rate are taken into account.
The diffusive pore structure was modeled with a cubic grid model, which provides information of the pore and filament diameters. Pore diffusion coefficients were determined using the general rate model.
Due to the large diameter to bed height ratio of membrane adsorbers, the adequate flow distribution is very important. Therefore, residence time distributions (RTD) of the devices were investigated using CFD simulations. The impact of bed height and dead volume in the devices was analyzed. Moreover, the influence of the housing and the membrane on the RTD of the total device were separated using CFD simulations.
It was possible to simulate experimentally obtained membrane adsorber breakthrough curves with a modification of the general rate model. This model was used to determine productivities of different potential membrane adsorber configurations.
The process productivity is increased by the factor of 90 for an optimized membrane adsorber compared to conventional state of the art resin processes, assuming an ideal flow distribution. The current status membrane material is already 22 times better than the resin process.

Zusammenfassung

Um Biomoleküle aus Fermentationsbrühe zu isolieren, ist ein schneller und effizienter Downstreamprozess erforderlich. Aufgrund von diffusiven Stofftransportbeschränkungen zeigt Resinchromatographie typischerweise eine starke Abhängigkeit der Bindungskapazität von der Verweilzeit und ist daher in der Trenngeschwindigkeit begrenzt. Kleine Partikel haben kleinere konvektive Zwischenräume und daher einen höheren Druckabfall über dem Chromatographiebett zur Folge. Die konvektive Chromatographie, die beispielsweise auf Membranen basiert, ist ein vielversprechender Ansatz, der nahezu verweilzeitunabhängige Trennprozesse in Bezug auf die Bindungskapazität darstellt und eine hohe Prozessproduktivität ermöglicht. Aufgrund der Struktureigenschaften rein konvektiver Trennmedien wird die spezifische Oberfläche und damit die Bindungskapazität oft zu einem limitierenden Faktor.
Membranadsorber mit biporöser Struktur können die Einschränkungen des Stofftransports im Vergleich zu konventionellen Resinchromatographiematerialien drastisch reduzieren. Konvektive Poren ermöglichen einen schnellen Stofftransport und diffusive Poren in den Membranstegen bieten Oberfläche für die Bindung. Die diffusiven Strecken in Membranen sind viel kleiner als herkömmliche Partikelradien, was höhere Flussraten im Prozess ermöglicht.
Das Ziel dieser Arbeit ist die modellbasierte Optimierung solcher biporöser Membranadsorber. Die Membran wird hinsichtlich Betthöhe, konvektiver Porosität, Permeabilität, diffusiver Porenstruktur und der Länge des Diffusionsweges optimiert. Der Einfluss der Zielmolekülgröße und der Durchflussrate wird berücksichtigt.
Sowohl die diffusive als auch die konvektive Porenstruktur wurde mit einem Gittermodell modelliert, das Informationen über die Poren- und Filamentdurchmesser liefert. Die Porendiffusionskoeffizienten wurden mit dem *General Rate Model* bestimmt.
Aufgrund des großen Durchmesser- zu Betthöhenverhältnisses von Membranadsorbern und des geringen Druckverlusts über die Membran ist eine adäquate Flussverteilung sehr wichtig. Daher wurden die Verweilzeitverteilungen (RTD) der Devices mit Hilfe von CFD-Simulationen untersucht. Der Einfluss von Betthöhe und Totvolumen in den Devices wurde analysiert. Außerdem wurde der Einfluss des Gehäuses und der Membran auf die RTD des gesamten Devices mit Hilfe von CFD-Simulationen getrennt.
Es war möglich, experimentell erhaltene Membranadsorber-Durchbruchskurven mit einer Modifikation des *General Rate Models* zu simulieren, um die Produktivität verschiedener potenzieller Membranadsorberkonfigurationen zu bestimmen.
Die Prozessproduktivität wird für einen optimierten Membranadsorber im Vergleich zu konventionellen Resinprozessen um den Faktor 90 erhöht, wobei eine ideale Strömungsverteilung vorausgesetzt wird. Das Membranmaterial im aktuellen Zustand ist bereits 22 mal besser als das Resinverfahren.

Nomenclature

Abbreviations

ABT	Agarose Bead Technology	
AM1	Agarose membrane 1	
AM2	Agarose membrane 2	
CHO	Epithelial cell line frome the ovary of the Chinese hamster	
CM	Cellulose membrane	
CSTR	Continuously stirred tank reactor	
CV	Column volume	
DBC	Dynamic binding capacity	$[g/L_{bed}]$
DPFR	Dispersed plug flow reactor	
EBC	Equilibrium binding capacity	
FITC	Florescein Isothiocyanate-Dextran	
HETP	Height equivalent of a theoretical plate	
i.d.	Inner diameter	
IgG	Imunoglobulin G	
iSEC	Inverse size exclusion	
LP15	Laboratory device	
MSS	Mab select sure resin from GE	
MV	Membrane volume	
PBS	Phosphate-buffered saline	
REM	Raster electron microscopy	
RTD	Residence time distribution	
SBC	Static binding capacity	$[g/L_{bed}]$

Dimensionless Parameters

Bodenstein number	$\mathrm{Bo} = uL/D_{ax}$
Reynolds number	$\mathrm{Re} = u_{int} d_p \rho/\eta_0$
Schmidt number	$\mathrm{Sc} = \eta/(\rho D_0)$
Sherwood number	$\mathrm{Sh} = k_f \cdot d_p/D_0$

Greek Symbols

δ	Film thickness	[m]
η	Dynamic viscostiy	[kg/m.s]
μ_t	First moment of area	[−]
ν	Kinematic viscosity	[m^2/s]
ω	Frequency in Fourier transform	[−]
$\omega_{agarose}$	Agarose mass fraction in the filament	[−]
ϕ	Fiber volume fraction	[−]
ρ	Density	[kg/m^3]
ρ_s	Specific adsorptive surface density	[mg/m^2]
σ	Stress	[kg/m.s]
σ_t	Second moment of area	[−]
τ	Fluid dynamic residence time $V/\dot{V}$	[s]
τ	Tortuosity	[−]
τ_{eff}	Residence time in the membrane pores $V\varepsilon_c/\dot{V}$	[s]
ε	Strain	[−]
$\varepsilon_{acetone}$	Porosity for acetone	[−]
ε_c	Convective porosity	[−]
ε_{dex}	Porosity for dextranes	[−]
ε_{IgG}	Diffusive porosity for IgG	[−]
ε_{max}	Maximum porosity	[−]
ε_{min}	Minimum porosity	[−]
ε_p	Diffusive porosity	[−]
ε_t	Total porosity of the column	[−]
φ	Polymer volume fraction	[−]

Symbols

Δh	Length variation	[m]
Δp	Pressure drop	[kg/m.s^2]
$\dot{m}$	Mass flow	[kg/s]
$\dot{n}$	Molar flow	[mol/s]
$\dot{V}$	Flow rate	[m^3/s]
A	Area	[m^2]
A	Coefficient in Ogston model	[−]
A	Van Deemter coefficient	[−]
a	Farazdaghi-Harris parameter	[−]

a	Marck-Houwing-Sakurada parameter	$[-]$
a	Pore shape constant	$[-]$
B	Van Deemter coefficient	$[-]$
b	Farazdaghi-Harris parameter	$[-]$
C	Van Deemter coefficient	$[-]$
c	Concentration	$[\mathrm{kg/m^3}]$
c	Farazdaghi-Harris parameter	$[-]$
c_{agarose}	Agarose gel concentration (w/v)	$[\mathrm{kg/m^3}]$
c_{in}	Inlet concentration	$[\mathrm{kg/m^3}]$
c_{p}	Concentration inside the particle pores	$[\mathrm{kg/m^3}]$
$c_{\mathrm{s+d}}$	Concentration signal of system and device	$[\mathrm{kg/m^3}]$
c_{s}	Concentration on the pore surface	$[\mathrm{kg/m^3}]$
c_{s}	Concentration signal of the system	$[\mathrm{kg/m^3}]$
D	Diffusion coefficient	$[\mathrm{m^2/s}]$
d	Diameter	$[\mathrm{m}]$
D_0	Molecular diffusivity in bulk	$[\mathrm{m^2/s}]$
D_{app}	Apparent diffusion coefficient	$[\mathrm{m^2/s}]$
D_{ax}	Axial disperion coefficient	$[\mathrm{m^2/s}]$
d_{bridge}	Membrane bridge diameter	$[\mathrm{m}]$
$d_{\mathrm{c,0}}$	Initial convective pore diameter	$[\mathrm{m}]$
$d_{\mathrm{c,pore}}$	Convective pore diameter	$[\mathrm{m}]$
D_{eff}	Effective diffusion coefficient	$[\mathrm{m^2/s}]$
$d_{\mathrm{fil,2}}$	Agarose filamet diameter + protein A	$[\mathrm{m}]$
$d_{\mathrm{fil,apparent}}$	Agarose filamet diameter + protein A + IgG	$[\mathrm{m}]$
d_{fil}	Agarose filamet diameter	$[\mathrm{m}]$
d_{h}	Hydrodynamic diameter	$[\mathrm{m}]$
d_{jun}	Diameter of agarose filament junctions	$[\mathrm{m}]$
d_{pore}	Pore diameter	$[\mathrm{m}]$
D_{p}	Pore diffusion coefficient	$[\mathrm{m^2/s}]$
d_{p}	Particle diameter	$[\mathrm{m}]$
D_{s}	Surface diffusion coefficient	$[\mathrm{m^2/s}]$
E	Peak function	$[1/\mathrm{s}]$
E	Young's modulus	$[\mathrm{kg/m.s^2}]$
F	Force	$[\mathrm{N}]$
F_{ab}	Fragment antigen binding	
F_{acc}	Pore accessibility factor	$[-]$

F_c	Fragment crystallizable region	
g	Gravity factor	$[m/s^2]$
h	Bed height	$[m]$
h	Gap between membrane and housing	$[m]$
K	Langmuir coefficient	$[L/g]$
k	Marck-Houwing-Sakurada parameter	$[-]$
k_{ad}	Adsorption constant	$[L/g.s]$
k_B	Boltzmann constant	$[J/K]$
k_{des}	Adsorption rate constant	$[1/s]$
K_D	Distribution coefficient	$[-]$
k_f	Film diffusion coefficient	$[m/s]$
L	Length	$[m]$
L_c	Column length	$[m]$
L_{diff}	Diffusive length	$[m]$
L_{tube}	Tube length	$[m]$
M	Fitting parameter in the model of Ham and Platzer	$[-]$
m	Mass	$[kg]$
m_{bound}	Bound mass	$[kg]$
M_W	Molar mass	$[g/mol]$
N	Fitting parameter in the model of Ham and Platzer	$[-]$
N	Number of filaments	$[-]$
N	Number of membrane layers	$[-]$
N	Number of theoretical plates	$[-]$
P	Permeability	$[mD]$
q	Load of the stationary phase	$[g/L_s]$
q_{max}	Maximum load of the stationary phase	$[g/L_s]$
q_s	Load of the stationary phase's surface	$[g/L_s]$
R	Diffusive particle's radius	$[m]$
r	Radial coordinate	$[m]$
r_f	Filament radius	$[m]$
r_{pore}	Pore radius	$[m]$
r_p	Particle radius	$[m]$
r_s	Stokes radius of the diffusing molecule	$[m]$
S_V	Specific surface	$[m^2/m^3]$
T	Temperature	$[K]$
t	Time	$[s]$

t_k	Fitting parameter in the model of Ham and Platzer	$[-]$
t_{max}	Fitting parameter in the model of Ham and Platzer	$[-]$
t_{min}	Fitting parameter in the model of Ham and Platzer	$[-]$
t_{plant}	Dead time of the plant	$[s]$
$t_{process}$	Process time	$[s]$
t_R	Retention time (residence time in chrom. columns)	$[s]$
t_{total}	Total retention time including plant	$[s]$
u	Superficial velocity	$[m/s]$
u_{int}	Interstitial velocity in the packed column	$[m/s]$
V	Volume	$[m^3]$
$V_{agarose}$	Agarose volume	$[m^3]$
$V_{convective}$	Convective volume	$[m^3]$
V_c	Column volume	$[m^3]$
V_{fil}	Filament volume	$[m^3]$
V_{int}	Interstitial volume	$[m^3]$
V_m	Membrane volume	$[m^3]$
$V_{particle}$	Particle volume	$[m^3]$
V_{pore}	Pore volume	$[m^3]$
V_R	Retention volume	$[m^3]$
V_{solid}	Solid volume	$[m^3]$
$V_{stat.phase}$	Stationary phase volume	$[m^3]$
x	Spatial coordinate	$[-]$
z	Spatial coordinate	$[-]$

List of Figures

List of Tables

1. Introduction

1

Biotherapeutics, such as antibodies, virus-like particles, or viral vectors, are produced from living cells or cell parts in bioprocesses. In the downstream part of the process, which is mainly categorized into a *capture*, a *purification* and a *polishing* step, target substances are separated and purified, cf. Figure 1.1. Chromatography is primarily employed in these three steps, as large volumes of a solute with a relatively low concentration of target molecules can be processed, and high separation efficiencies are achieved compared to other separation technologies such as extraction. In chromatography, the separation of a mixture takes place between a stationary and a mobile phase. [Cart2010]

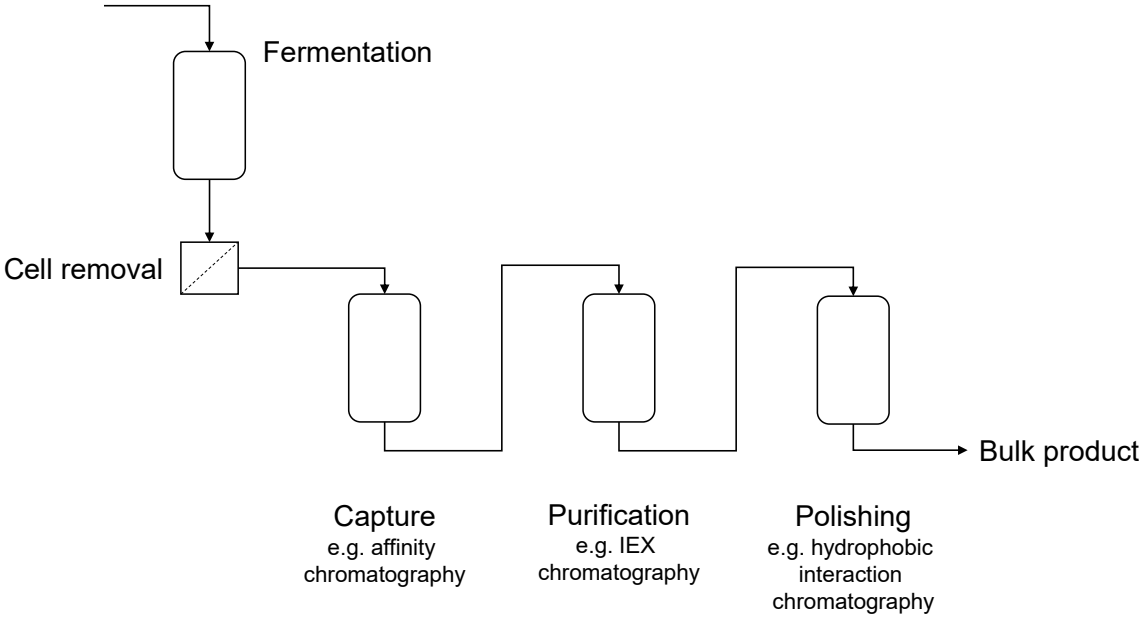

Figure 1.1.: Generalized downstream flow sheet for the purification of biotherapeutics, adapted from Carta and Jungbauer [Cart2010]

Traditionally, porous particles, also known as resins, are used as stationary phase, providing a high specific surface for binding. In Figure 1.2 a packed column with the occurring mass transfer phenomena is shown schematically. A wide range of stationary phase materials is available on the market [Schm2006]. Cross-linked agarose is a classical polymer resin material, most widely used in antibody purifications. Agarose beads are easily brought into shape and allow a broad range of controllable sizes and porosities. Moreover, agarose shows little unspecific binding, and good activation and modification properties [Schm2006]. This is why this material is used for the investigations in this work.
Despite the high specific surface for binding, resin chromatography suffers from high residence times due to a diffusive mass transfer limitation inside the diffusive

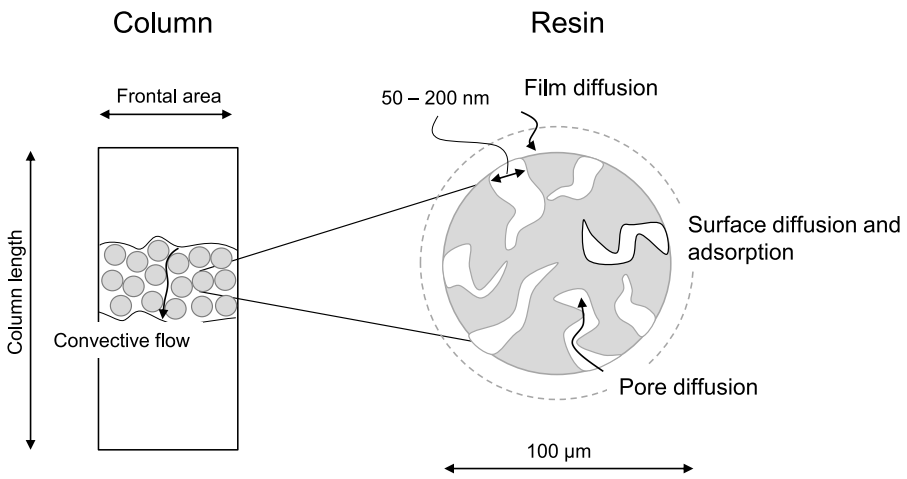

Figure 1.2.: Schematic representation of a resin packed column with indication of occurring mass transfer phenomena. Resin particle diameters are in the range of $\approx 50\,\mu$m and diffusive pores have diameters of $\approx 50 - 200\,$nm

pores. This leads to limited productivity of the process. The mass transfer limitation results from long diffusive pathways ($50\,\mu$m) and small diffusive pore diameters ($50 - 200\,$nm). A reduction of the resin diameter would lead to packing difficulties and a high-pressure drop over the column, causing mechanic stability problems.

To overcome these limitations, materials with shorter diffusive pathways, as monoliths, perfusion material, or membrane adsorbers, have been developed. As this work is about the model-based design of high capacitive membrane adsorbers, this alternative is focused. In conventional membrane adsorbers, the binding sites for the target molecules are directly attached to the convective pore walls, cf. Figure 1.3 (left). Therefore, these membranes are suitable for purifying large biomolecules at high flow rates without losing binding capacity. However, the specific surface for binding is low, as is the static binding capacity, compared to resin material. A reduction of the convective pore size would lead to higher binding capacities but also to a drastic increase of pressure drop over the membrane bed and potentially also fouling due to relatively small convective pores that might be blocked. Hence, only small bed heights are possible, which causes scaling and fluid distribution problems. The binding capacity of convective membrane adsorbers can be increased by applying a porous hydrogel layer on the convective pore surface, cf. Figure 1.3 (middle). Such adsorbers, as, e.g., Sartobind from Sartorius (Germany), are commercially available. A further increase of the capacity is achieved by porous membrane bridges currently developed at Sartorius Stedim Biotech, cf. Figure 1.3 (right). Due to short diffusive pathways, the dynamic binding

capacity is only reduced by high flow rates. The low residence time is not sufficient for total penetration, so that only the outer layers of the stationary phase are used for adsorption. Using similar convective and diffusive porosities as in resin packed columns, the membrane adsorber is no longer limited regarding binding capacity.

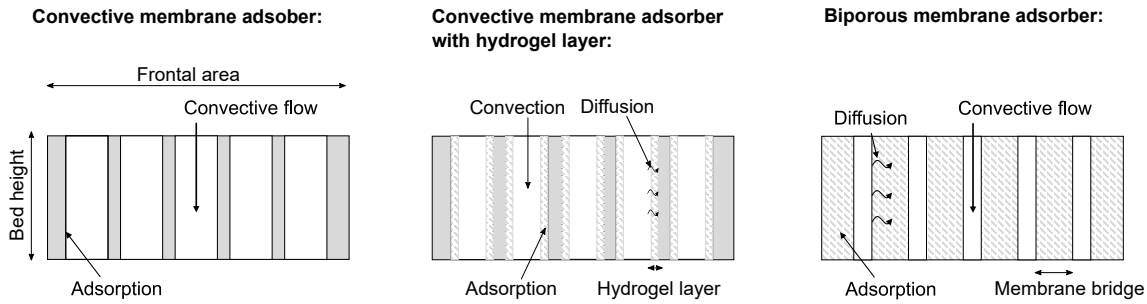

Figure 1.3.: Membrane adsorber materials

Membrane adsorber devices are usually available in an axial or radial configuration. In an axial device, several membranes are stacked, and the flow goes from top to bottom. In a radial device, the membrane is wound around a cylinder core and is typically flown through from outside to inside. The ratio of frontal area to bed height in both types is usually much smaller then in chromatography columns. Therefore, non-uniform flow distribution may impact the product's breakthrough curve and lead to a reduction of productivity.

This work aims to optimize the design of the membrane material regarding productivity, utilizing the binding sites, and its mechanic stability using mathematical models. To this end, the membrane parameters (bed height, permeability, and convective porosity), as well as the stationary phase parameters (the membrane bridge diameter, the diffusive porosity, and the diffusive mass transfer), are optimized using mathematical models. In this work, the focus is on the affinity chromatography of the target molecule immunoglobulin G (IgG) and the ligand protein A, which is performed in the *capture step*. Due to its interaction with the human immune system, IgG is therapeutically applicable and the most popular monoclonal antibody [Dijk2001]. In a majority of cases, protein A is used as a ligand on the stationary phase of the chromatography step [Gott2009; Shuk2007; Mari2012]. An outlook on the impact of larger molecules on the membrane design is given.

Previous publications in student thesis

This thesis' content and results emanate from research conducted under the affiliation and position of the author as scientist at Sartorius Stedim Biotech GmbH and PhD candidate at RWTH Aachen University. The work comprises data based on the following student theses:

- Olgun Aktuk, Bachelor Thesis, 2018, *Determination of pore size distribution and porosity of chromatographic media for antibody purification*, RWTH Aachen University
- Sebastian Mädler, Bachelor Thesis, 2019, *Investigation of mass transfer in porous particles on the basis of breakthrough curves*, Technische Universität Dresden
- Danchen Zhang, Bachelor Thesis, 2020, *Characterization of flow and residence time distribution in membrane chromatography devices using CFD*, RWTH Aachen University
- Robert Blaszczyk, Bachelor Thesis, 2020, *Simulative investigation of the membrane housing influence of a lab device on the residence distribution*, RWTH Aachen University
- Johannes Schäfer, Master Thesis, 2020, *Characterization and simulation of the chromatographic performance of novel membrane adsorbers*, Technische Hochschule Mittelhessen

2. Structure of the thesis

2

Figure 2.1 shows the designing procedure used in this work. The motivation to use models for the optimization of the membrane material is, that experiments of different membrane configurations, even of those that cannot be produced yet, can be performed. Moreover, modeling saves time, resources and costs.

In the first part of this work the diffusive pore structure and with it, the trade-off between binding capacity and diffusive mass transfer is investigated, using conventional agarose resins. Flow rates are adapted to resin processes resulting in residence times of $4 - 6\,\mathrm{min}$. The agarose structure is described by a simple geometric model, which is capable to predict the specific surface and with that binding capacities. Diffusion coefficients were determined from a breakthrough curve model which was fitted to experimentally obtained breakthrough curves.

In the second part, the hydrodynamics and the flow distribution in test devices are investigated by experiments and CFD simulations. The flow distribution in the membrane adsorber device has an important impact on the quality of the breakthrough curve: In case of ideal distribution, the breakthrough curve is only affected by mass transfer phenomena. A membrane adsorber with non-ideal flow distribution leads to areas with high throughput where the binding sites are quickly occupied. Breakthrough occurs and the process is stopped, even though other areas of the membrane, which have less throughput still have available binding sites. An acetone tracer is used to investigate the impact of dead volume, bed height, porosity and permeability on the residence time distribution. Moreover, the impact of the housing and the membrane, which together make up the device, on the residence time distribution are investigated separately.

In part three, membrane adsorber breakthrough curves are modeled, using a modification of the general rate model. At first, breakthrough curves of a membrane which is currently under development are experimentally recorded for different flow rates and device configurations. The experimental data were then simulated. In the considered work areas, the model describes the experimental data and therefore, dynamic binding capacity at $10\,\%$ breakthrough can be predicted.

In part four, the design of the membrane adsorber is optimized. The membrane bridge diameter highly impacts the limitation of diffusive mass transfer and therefore, the steepness of the breakthrough curve. Hence, the trade-off between

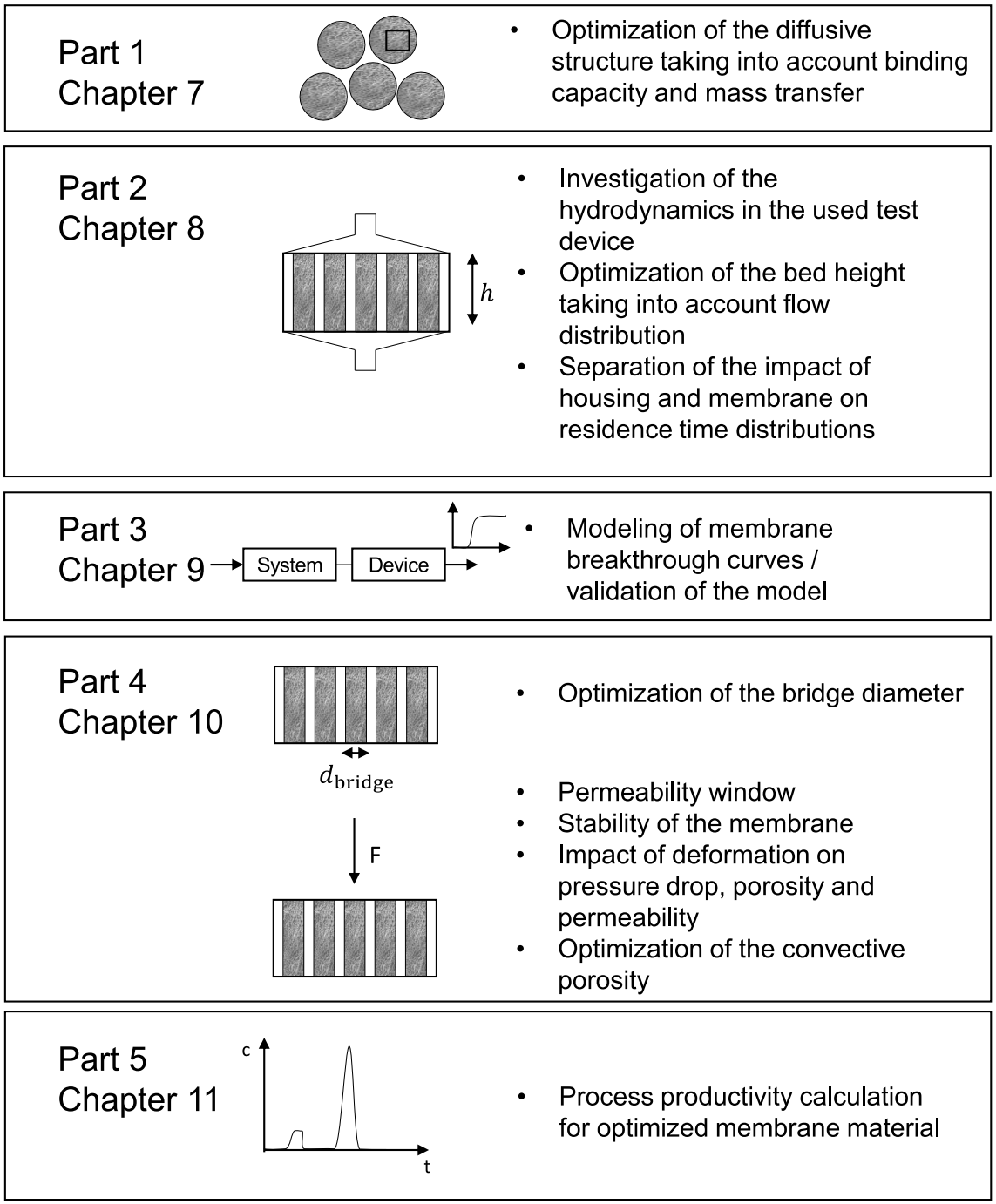

Figure 2.1.: Flow chart leading through this work

fast mass transfer and available surface for binding is investigated. Moreover, a closer look is taken on the impact of permeability and membrane deformation. At the end of part four, the convective porosity of the membrane adsorber is optimized.

A productivity potential analysis for a model process is performed in part five. To this end, a 3 mL membrane adsorber device is modeled, including the impact of the chromatographic system and the hydrodynamics. A productivity study of the membrane beds is performed for several configurations, in order to optimize the process flow rate and to determine the potential of biporous membrane adsorbers.

3. State of the art

3.1. Chromatography

Chromatography is a thermal separation process [Satt1995]. Components that are solved in a fluid (gas or liquid) are separated between a mobile and a stationary phase (liquid or solid). There are two types of chromatographic processes: In analytical chromatography, the focus lies on the qualitative and quantitative determination of a component. In contrast to that, in preparative chromatography it is the aim to isolate and purify products in large scale and recover them in the same condition they were in before the separation. It is used for the purification of complex macromolecular biopharmaceuticals. [Schm2006; Goed2006a]

3.1.1. Binding types and mechanisms

Two binding types can be distinguished [Ever1972]: Physisorption is a weak binding, which is based on Van der Waals forces where maintain their chemical identity. Chemisorption is a stronger binding which is caused by valence forces and is equivalent to chemical binding. The adsorption processes in preparative chromatography are based on physisorption, as the chemical integrity of the target molecule is required. Different separations mechanisms are summarized in the Appendix A.1.1.

3.1.2. Chromatograms

The resulting chromatograms for analytical and preparative capture chromatography are presented in this section.

Analytical chromatography Basic information, such as the concentration of a component in the solution, which is derived from the peak area and its residence time, which is calculated from the position of the peak's gravity center, is given in a chromatogram, cf. Figure 3.1.
Components of a solution often have different retention times, depending on the strength and mechanism of the interaction with the stationary phase, and therefore can be separated by chromatography. The retention time of the tracer only in the column is $t_R = t_{total} - t_{plant}$. For further calculations, the chromatogram has to be adjusted by subtracting the plant residence time. In case of symmetrical peaks shapes, the retention time can be determined by the peak maximum. For

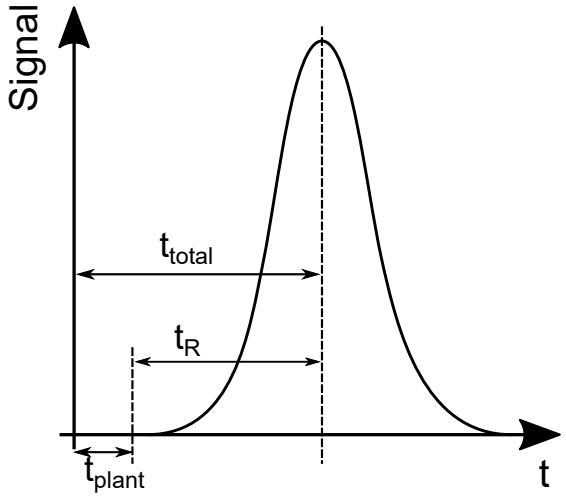

Figure 3.1.: Analytical chromatogram with residence times

asymmetrical peaks the retention time has to be calculated with the method of moments from the point of gravity, Equation A.1. The dead time of the plant (or system) and column (t_{total}) is the time, a non-retained substance needs from injection to the point of detection.

Preparative chromatography The chromatogram of preparative capture chromatography shows the breakthrough and the elution of the target molecule, cf. Figure 3.2.

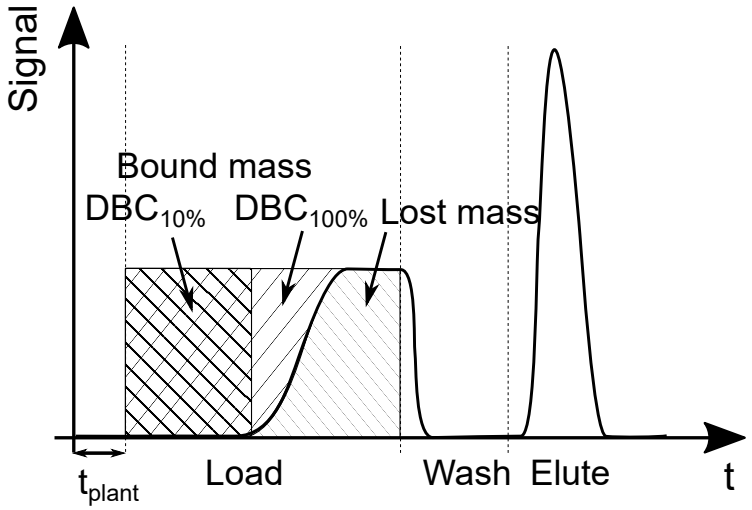

Figure 3.2.: Preparative chromatogram with binding and elution phase

The process is divided into different steps:

Column equilibration: The column is washed with equilibration buffer.

Load: The column is loaded with a solution containing the target molecule and other components. The target molecule is bound onto the stationary phase. When the stationary phase is saturated breakthrough occurs. The area above the curve is the bound mass on the column, also called dynamic binding capacity at 100 % breakthrough ($DBC_{100\%}$). The area below the curve is unbound mass that leaves the column. For this reason, processes are usually stopped, when breakthrough occurs. The performance of preparative chromatography medium is often evaluated at the point where 10 % of feed concentration is reached at the column outlet. The dynamic binding capacity at that point is called $DBC_{10\%}$. In an industrial process, the loading step is stopped as soon as 80 % of $DBC_{10\%}$ breakthrough are detected, in order not to lose valuable product.

Wash: In the washing step, all unbound molecules are washed out of the column.

Elute: By e.g. a pH shift in affinity chromatography or a change of the salt content in ion exchange chromatography, the bound molecules elute from the stationary phase. In order to obtain a high concentration the peak should be as narrow as possible. The less elution buffer is used, the higher the concentration of the target molecule.

Cleaning in place (CIP): The chromatographic medium is stripped with different buffers to remove all bound contaminants.

The productivity of the process is calculated with the following equation:

$$P = \frac{m_{\text{bound}}}{V_{\text{stat. phase}} \cdot t_{\text{process}}}. \tag{3.1}$$

The productivity of the overall process can be increased by an optimization of the loading step, which depends on the slope of the breakthrough curve. In case of a flat breakthrough curve, breakthrough occurs earlier and the process has to be stopped. The slope of breakthrough curve depends on the hydrodynamic of the surrounding system (tubes and valves), on the hydrodynamic in the fluid distributor and collector, on the binding capacity and on mass transfer phenomena inside the

chromatographic bed. The impact of mass transfer effects on the breakthrough curve is further precised in Appendix A.1.2.

3.1.3. Characterization of column efficiency

A useful approach to characterize peak broadening related to column characteristics, is the determination of the height equivalent of a theoretical plate (HETP). In the classical plate model of Martin and Synge [Mart1941] the column is treated as a series of equilibrium stages. The more stages, the higher the efficiency of the column. However, this model explains quantitatively the relation between HETP and column efficiency, it is inadequate for tailing peaks or non-linear adsorption isotherms [Cart2010]. Further models are summarized in the Appendix A.1.3.
The determination of the HETP is based on the dynamic response of a Dirac tracer signal under isocratic conditions (no concentration gradient). A high column efficiency leads to a sharp response peak, whereas a low efficiency results in a broad one. Next to a small peak that can be treated as a delta function, a strictly linear adsorption equilibrium is required [Cart2010]. For affinity chromatography, an acetone tracer or the target molecule under non-binding conditions, is used to characterize the bed packing and the hydrodynamic of the system. The HETP can be calculated from the following equation:

$$\mathrm{HETP} = \frac{\sigma_t^2 \cdot L}{\mu_t^2} = \frac{L}{N}, \tag{3.2}$$

where L is the column length, N the plate number, μ_t the residence time, which is calculated with the first and σ^2 the second statistical moment. First and second statistical moment are defined in Appendix A.1.3. The influence of different band broadening parameters on the overall efficiency of a column is described by van Deemter, Zuiderweg and van Klinkenberg [Deem1956], cf. Figure 3.3:

$$\mathrm{HETP}_i = A_i + \frac{B_i}{u_{\mathrm{int}}} + C_i \cdot u_{\mathrm{int}}. \tag{3.3}$$

A mainly describes eddy diffusion which results from packing imperfections and particle size distributions. Influence of axial diffusion in the fluid phase, which is often times neglected, except for large particles in preparative chromatography, is

described by $\frac{B}{u_{\text{int}}}$. The third term, $C \cdot u_{\text{int}}$, describes the increasing influence of the mass transfer resistance at higher velocity.

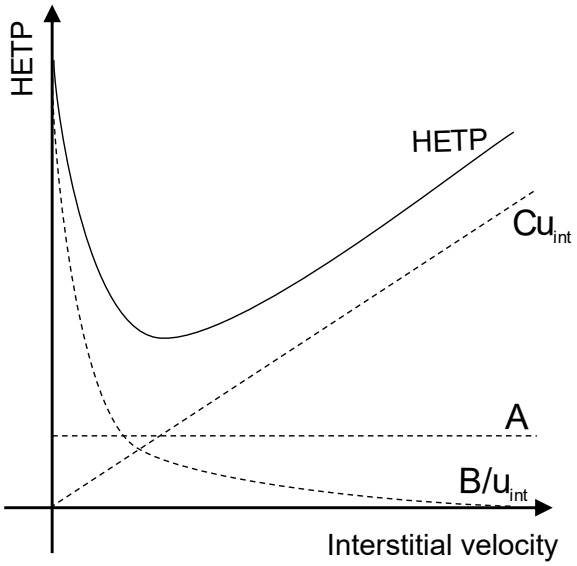

Figure 3.3.: Influence of the interstitial velocity on the HETP value

From the van Deemter curve, the optimum flow rate for the processing of a column can be determined. The best separation quality is obtained at the curve's minimum. The HETP is different for every tracer molecule and HETP measurements under non-binding conditions are not representative for binding conditions. In most likely case of a non-linear isotherm, HETP requires a model to distinguish between band broadening due to dispersive factors and due to thermodynamics.

3.1.4. Target molecules

Chromatography in downstream processes is used for the purification of many different bio-pharmaceutical molecules, such as monoclonal antibodies, virus-like particles or viral vectors.

Immunoglobulin G

The amount of monoclonal antibodies (mAbs) in biotherapeutics has increased since the 1980s and they have become an important medical product. [Ecke2015; Lamb2016; Liu2014; Moul2016] Monoclonal antibodies are identical antibodies that recognize the same epitope of an antigen. Polyclonal antibodies, on the contrary, represent a mixture of antibodies that are specific for one of the different

epitopes of an antigen. Antibodies, also called immunoglobulins (Ig), are the answer of the immune system on antigens. There are five classes of immunoglobulin: IgG, IgA, IgM, IgD and IgE. The most popular monoclonal antibody is IgG. Due to its interaction with the human immune system, it is therapeutically applicable [Dijk2001]. The structure of IgG is presented in Figure 3.4.

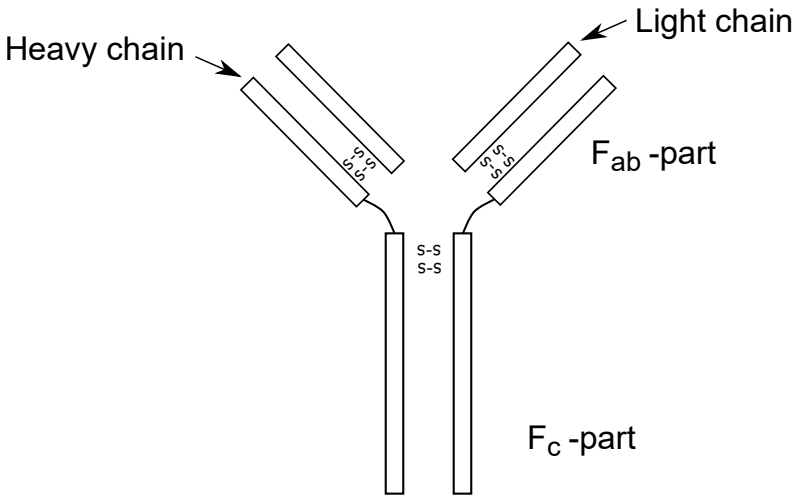

Figure 3.4.: Structure of IgG

It consists of two heavy and two light chains, which are connected by disulphide bounds. The variable F_{ab} part of the IgG binds to the antigen and the constant F_c is able to bind to protein A [Choe2016] at a pH near to the isoelectric point of IgG. By decreasing the pH to a value lower than 3, the bound is released. In more than 60 % of cases protein A resin chromatography is used as capture step in the downstream process. [Gott2009; Shuk2007; Mari2012]

Virus-like particles and viral vectors

Virus-like particles (VLPs) have the same structural characteristics and show similar antigens as the parental virus. As they do not incorporate genetic material, they are non-infectious. Due to their high amount of epitopes at the surface, VLPs provoke a strong immune response (= production of antibodies) and are therefore promising vaccine candidates. Typically, the size of VLPs is in the range of 22 to 150 nm. [Grga2006]

Viral vectors are gene modified viruses, that can deliver therapeutic genes into cells. The viruses of choice are retro, adeno, adeno assoiciated, herpes and pox

viral vectors in the range of 20 to 400 nm. [Walt2000; Mert2011]

For VLPs and viral vectors, chromatography is used for the purification and the polishing steps. The stationary phase are usually ion exchange or affinity resin packed beds or membranes. Further information can be found in Merten and Al-Rubeai [Mert2011]. Due to the large diameters of VLPs and viral vectors, the diffusive mass transfer inside the porous particles is slow and the dynamic binding capacity is low. Therefore, alternative chromatographic materials were developed, which are discussed in Section 3.1.5.

3.1.5. Chromatographic material

Basic definitions

Conventional chromatographic beds consist of porous particles. The total column volume (V_c) of a packed bed is divided into the interstitial volume (V_{int}) and the particle volume ($V_{particle}$), Figure 3.5. The latter is composed of the solid volume (V_{solid}) and the pore volume (V_{pore}).

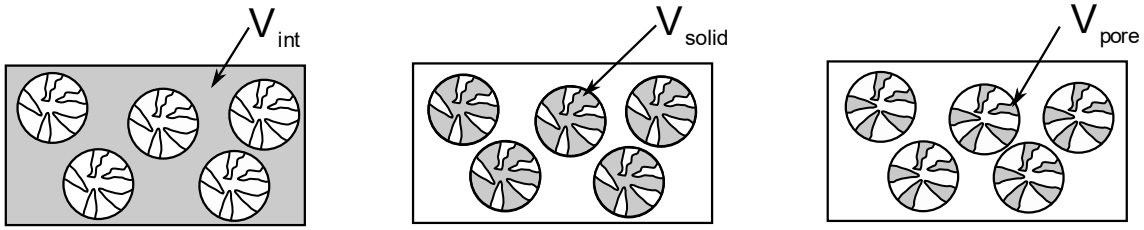

Figure 3.5.: Definition of volumes in a packed bed adapted from Schmidt-Traub [Schm2006]

Using these different volumes, corresponding porosities can be calculated.
The void fraction

$$\varepsilon_c = \frac{V_{int}}{V_c}, \tag{3.4}$$

the porosity of the solid phase:

$$\varepsilon_p = \frac{V_{pore}}{V_{particle}} = \frac{V_{pore}}{V_{solid} + V_{pore}} \tag{3.5}$$

and the total porosity

$$\varepsilon_t = \frac{V_{int} + V_{pore}}{V_c} = \frac{t_R \cdot \dot{V}}{V_c}. \tag{3.6}$$

The void fraction of packed beds lies in the range of $0.26 < \varepsilon_c < 0.48$. As a mean value $\varepsilon_c = 0.37$ can be applied [Brau1971].

Stationary phase material

Stationary phases for conventional chromatography can be divided into inorganic materials, such as zeolites, active carbon and silica, organic polymers as for example agarose gel or cellulose, and synthetic polymers such as acrylate [Schm2006]. In bio-chromatography organic polymers are mostly used. Next to mechanical stability, which is obtained by cross linking, these gels have to be biocompatible and stable regarding alkalines due to cleaning steps and sanitization.
Historically, many chromatographic media are made of agarose. Agarose is a polysaccarid from the red seaweed *Garcilaria* genus and forms a gel material. It shows a hysteresis in melting and gelation temperatures. When cooling down, gelation takes place at about $25\,°C$. At about $80\,°C$ liquefaction occurs, when heating up. Agarose chains consists of an altering copolymer of 1,3-linked β-D-galactopyranose and 1,4-linked 3,6 anhydro-α-L-galactopyranose, cf. Figure A.2 in the appendix. [Maci2008]
In literature a three-step gelation process is proposed, cf. Figure 3.6 [Ande1969]: The agarose chains form coils in the solution. During the gelation process, the coil-helix transition and the helix aggregation take place. Two copolymer chains are related by an axial translation of half the single chain pitch ($= 1.9\,\mathrm{nm}$) and form a parallel double helix. They aggregate to bundles of $6 - 11$ helices on average. [Arno1974; Djab1989]
The agarose filament diameter (d_{fil}) was determined in literature and a summary is given in Table 3.1. It was found that the filament diameter is independent from the agarose concentration. Moreover the concentration of organic material in the fiber was determined to be $0.65 - 0.82\,\mathrm{g/mL}$ and the density of the agarose $1.6\,\mathrm{g/mL}$ [Laur1967].

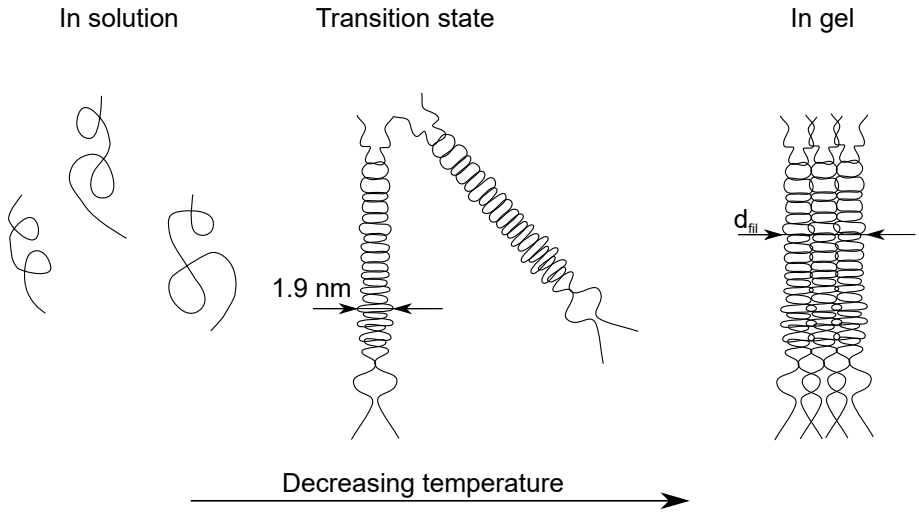

Figure 3.6.: Gelation process of agarose and formation of agarose filaments with decreasing temperature, according to [Ande1958]

Table 3.1.: Agarose filament diameter

d_{fil} [nm]	Measuring method	Concentration range	Author
$d_{fil} = 5.0$	Inverse size exclusion	$2 - 8\,wt\%$	[Laur1967]
$d_{fil,1} = 8.2$ $d_{fil,2} = 2.9$	Small angle X-ray scattering	$0.1 - 5\,wt\%$	[Djab1989]
$d_{fil} = 10.0$	Electron microscopy	-	[Guen1992]
$d_{fil} = 11.8$ $d_{jun} = 28.7$	Small angle X-ray scattering	MabSelect Sure Agarose + protein A	[Plew2018]

The filament diameter increases, when the ligand is attached. When the target molecule adsorbes, the diameter further increases. In case of protein A and IgG the resulting protein layer thickness is about 5.5 nm [Plew2018].

Comparison of beads and alternative stationary phases

In conventional bead based chromatography, the mass transfer in the interstitial space occurs by convective flow. Inside the beads, the mass transport to the binding sides takes place by diffusion.
Conventional beads, used in protein separation, have avarage diameters of 100 μm. Due to their porous structure, they have a large inner surface available for binding, leading to high binding capacities. On the downside, their long diffusive pathways require high residence times and therefore low flow rates. An increasing flow rate leads to a loss of dynamic binding capacity, as the target molecules passe through the column before all binding sites in the particles are occupied.

The binding capacity is also reduced for bigger target molecules, due to limiting bead pore sizes and slower diffusion. The data from literature plotted in Figure 3.7 shows the decrease of dynamic binding capacity at 10 % breakthrough with increasing hydrodynamic diameter of the diffusing particle.
One option for a better ligand utilization and shorter diffusion time is the reduction of the diffusive pathway. When reducing the bead diameter the diffusive pathways decrease, but the pressure drop over the column increases. This relation is described by the Carman-Kozeny equation for fixed beds with granular particles

$$\frac{\Delta p}{L_\mathrm{c}} = 150 \cdot \frac{\eta \cdot (1-\varepsilon_\mathrm{c})^2 \cdot u}{d_\mathrm{p}^2 \cdot \varepsilon_\mathrm{c}^3}, \tag{3.7}$$

where η is the mobile phase dynamic viscosity, u the superficial velocity and d_p the average particle diameter [Schm2006; Guio1994]. The derivation of Equation 3.7 is presented in Appendix A.1.4.
For incompressible beads, the pressure drop is inversely proportional to the square of the average particle diameter of the packing. For compressible beads, the bed becomes compressed and the permeability declines even further. The column pressure increases in a non linear manner up to a certain critical velocity at which

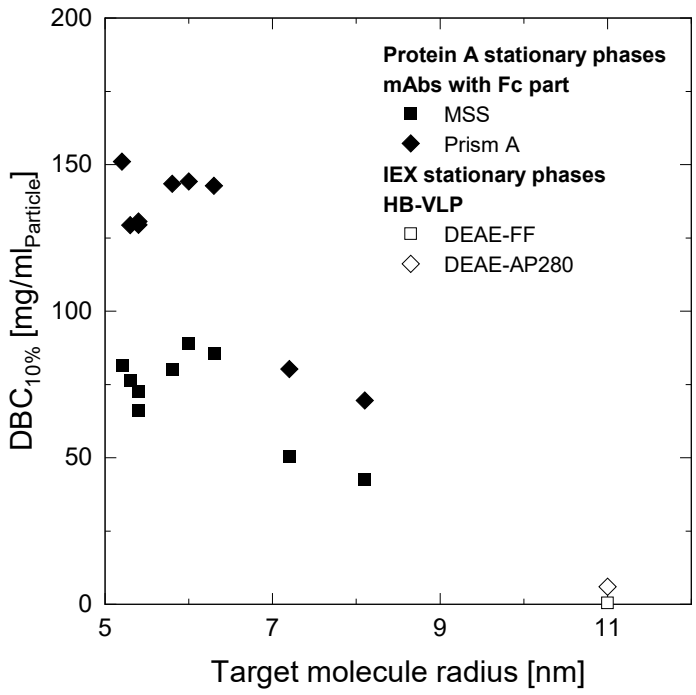

Figure 3.7.: $DBC_{10\%}$ at 4 min residence time for the protein A stationary phases as a function of diffusing particle's hydrodynamic diameter, data taken from [Pabs2018] (filled symbols) and ion exchange stationary phases, data taken from [Yu2014] (non-filled symbols).

the bed collapses.

To overcome the previously discussed limits of resin chromatography, several materials have been developed. Their dynamic binding capacities at 10 % breakthrough as a function of the residence time are compared in Figure 3.8. The data shows, that the same $DBC_{10\,\%}$ at lower residence times can be obtained. Further information on these materials is given in the next sections.

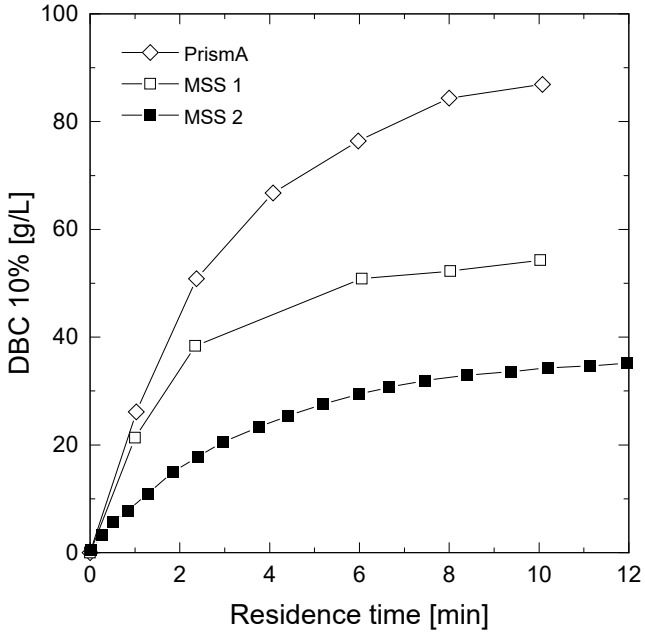

(a) Conventional stationary phases

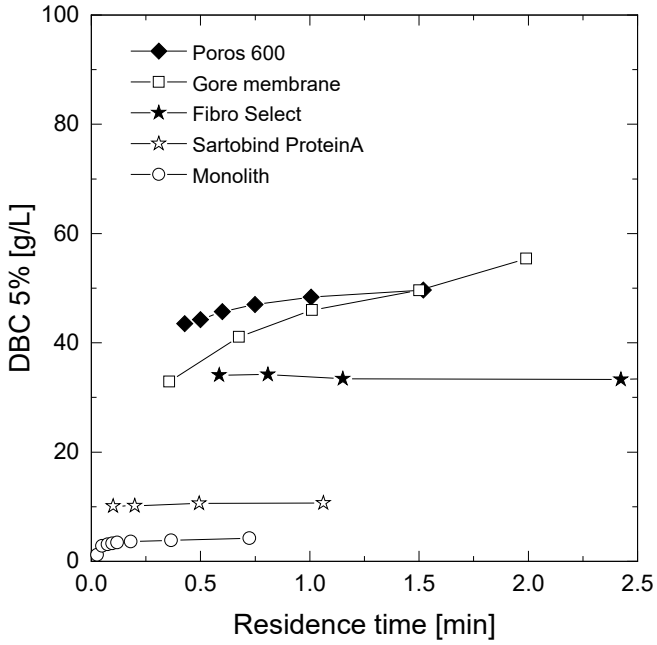

(b) Alternative stationary phases

Figure 3.8.: Comparison of conventional and alternative stationary phases: Dynamic binding capacity measured at 10 % and 5 % breakthrough and referred to the volume of chromatographic bed. Conventional stationary phases: PrismA and MSS 1 data from [GE H2017], MSS 2 data taken from [Hahn2005]. Alternative stationary phases: Poros 600 data is taken from [Appl2009], Gore membrane data from [WL G2017], Fibro select data from [GE H2017], Sartobind data from [Boi2008] and monolith data from [Jung2008] (a 30 mm column was assumed).

Perfusion chromatography beads

Perfusion chromatography beads have two different kinds of pores: through-pores with a diameter of $600 - 800\,\mathrm{nm}$, that enable convective flow through the particles, and diffusive pores with a diameter of $50 - 150\,\mathrm{nm}$ that generate a high surface area for adsorption [Gust1998]. The diffusive pathways can be reduced to $< 1\,\mu\mathrm{m}$ and high flow rates of $5000\,\mathrm{cm/h}$ become possible without loss of dynamic binding capacity [Afey1990; Gust1996]. The commercial available ®POROS material, is used for the purification of several virus-like particles [Jian2011; Phel2007; Cook1999].

Monoliths

The continuous stationary phase is cast in a single block and inserted into a chromatography housing [Iber1999]. In this material, all channels are highly interconnected and diffusive pathways are small $(1 - 15\,\mu\mathrm{m})$ [Tall2002; Hahn2000; Jung2008]. Velocity shows only little influence on breakthrough curves and the maximum dynamic binding capacity is already reached at $0.2\,\mathrm{min}$ residence time [Jung2008]. Furthermore, monoliths show significantly lower pressure drop than conventional packed beds [Pfau2013] and they are suitable for the separation of large biomolecules. The scale-up of this technology is one of the major challenges. It is difficult to generate a homogeneous pore structure in larger scales, because monoliths are produced in an exothermal polymerization process [Jung2008]. Moreover, the sealing of the monolith with the wall has to be guaranteed.

Hybrid materials

Avramescu et al. showed, that it is possible to build membrane adsorbers out of entrapped particles in polymeric material [Avra2003]. This method combines high binding capacity, low pressure drop and high throughput. A patent for a polymer membrane with incorporated particles was published by Demmer et al. [Demm2007]. A hybrid material was developed by Mc Manaway [Mc M2017] and commercialized by Gore, known as Gore Protein A capture, containing a porous polyethersulfone membrane and porous silica particles of a diameter of approximately $20\,\mu\mathrm{m}$. Using this structure, a high surface for binding with short diffusive pathways is generated. The void volume between the particles can be

increased due to the membrane and the flow resistance is decreased. The low alkali stability of silica presents a problem for the utilization in production processes.

Membrane adsorbers

A membrane adsorber consists of an adsorptive membrane and a housing, that has the purpose to distribute and collect the mobile phase. Typical material for membranes used in chromatography are cellulose, regenerated cellulose, polysulfone, polyamide and composite membranes [Char2012]. Conventional membrane adsorbers have a solid volume (membrane material) and a pore volume, which is called convective volume ($V_{\text{convective}}$), cf. Figure 3.9.

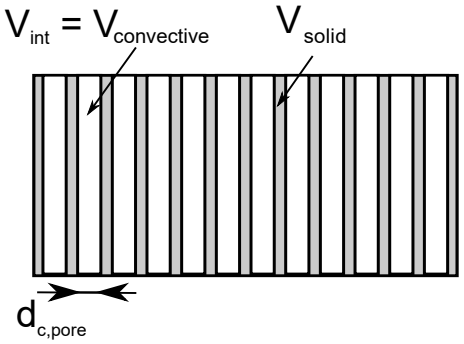

Figure 3.9.: Definition of volumes in a membrane adsorber [Char2012]

The convective membrane porosity is determined by

$$\varepsilon_{\text{c}} = \frac{V_{\text{convective}}}{V_{\text{m}}}. \tag{3.8}$$

The binding sites are located at the convective pore walls. The surface area is therefore entirely accessible by convective flow and the dynamic binding capacity is nearly independent from the flow rate. Therefore, membranes are suitable for the separation of large biomolecules at high flow rates. However, convective membranes underlie low binding capacities, due to a low surface area [Brie1992; Bran1988]. The surface of the membrane depends on the pore diameter and the porosity of the membrane. With decreasing pore diameter, binding capacity can be increased (at constant porosity) but the pressure drop over the membrane increases following the law of Hagen-Poiseuille (derivation in Appendix A.1.4)

$$\frac{\Delta p}{L} = \frac{32 \cdot \eta \cdot u_{\text{int}} \cdot \tau}{d_{\text{c,pore}}^2}. \tag{3.9}$$

The law of Hagen-Poiseuille assumes, that the membrane consists of parallel flow tubes with equal diameter. To consider non-idealities, the tortuosity τ is inserted into Equation 3.9. The tortousity is a parameter, which is adapted from experimental data, to describe the extension of the diffusive pathway due to twisted pores.
Darcy's law is used to calculate the permeability of the membrane

$$P = \frac{\dot{V} \cdot \eta \cdot L}{A \cdot \Delta p}. \tag{3.10}$$

In order to run at an elevated flow rate in order to achieve higher productivity, the membrane bed height can then be decreased. Convective membranes with a high binding capacity per membrane volume usually have small bed heights. The drawback of these membranes is, that the frontal area has to be increased to scale up the membrane volume. This leads to flow distribution problems. Tejeda et al. published a method of the optimal affinity membrane adsorber design [Teje1999]. However, these approaches are not sufficient to achieve the $\mathrm{DBC}_{10\,\%}$ values of conventional resins, while maintaining convective pores that ensure low-fouling tendency. Moreover, larger convective pores allow for bed heights that ensure scaleability into larger devices by reducing the frontal area. The scale-up of membrane adsorbers was investigated by Demmer and Nussbaumer [Demm1999]. In order to combine high possible flow rates and high binding capacities, a novel material has to be developed that combines both. One approach is the Sartobind Q membrane from Sartorius, Göttingen. This membrane adsorber consists of transport pores in the micrometer range which are coated with a swollen hydrogel network with pores in the nanometer scale. The porosity of the membrane is about 0.78, cf. Tatárová et al. [Tatá2009]. By decreasing the membrane porosity and the production of membrane adsorbers with porous membrane bridges, the binding capacity can be further increased.
Common membrane adsorber types are flat sheet, hollow fiber and radial flow membranes [Ghos2006]. Flat sheet and radial flow membranes usually have a smaller bed height to radius ratio than columns, cf. Figure 3.10 and therefore special attention has to be payed on the flow distribution at the module inlet and collection at the outlet. Barbe worked on the fluid dynamic in membrane adsorber systems [Barb2009]. In this work Section 3.2.2 deals with the flow distribution in the device.

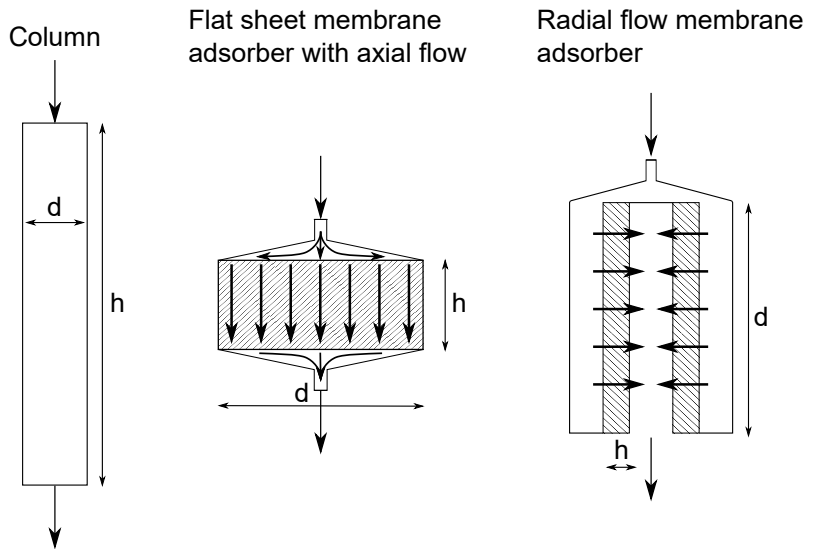

Figure 3.10.: Bed height to radius ratio of a conventional chromatography column and membrane adsorbers and flow direction in membrane adsorbers

Mechanical properties

Using the laws of mechanics, the compression of the chromatographic bed can be derived. Hook's law states, that the stress $\sigma = \frac{F}{A}$ is proportional to the strain ε in the linear elastic range. The proportionality factor between σ and ε is the modulus of elasticty E

$$\sigma = E \cdot \varepsilon. \tag{3.11}$$

The strain is defined as the change of height divided by the original height

$$\varepsilon = \frac{\Delta h}{h}. \tag{3.12}$$

The strain in case of transverse contraction is derived in the Appendix A.1.4.

3.2. Mass transfer

This section deals with mass transfer effects occurring in chromatographic processes, as they form the basis for understanding and design of chromatographic media. A well designed material ensures an optimum ligand utilization and high $DBC_{10\,\%}$ values. Figure 3.11 summarizes the occurring mass transfer effects in

a chromatography column. These effects are transferable to the membrane adsorbers, used in this thesis. In the interstitial phase convective and dispersive mass transfer occurs. The concentration in the stationary phase is c. Due to a concentration gradient ($\Delta c = c - c_p$) film diffusion occurs at the boundary between mobile and stationary phase. The target molecule diffuses into the pores stationary phase and then adsorbs onto the surface.

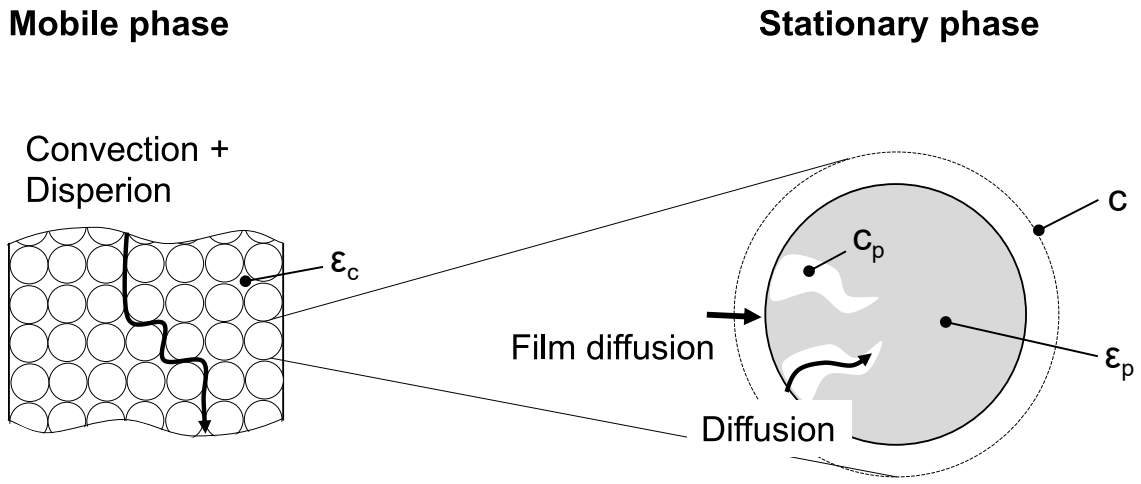

Figure 3.11.: Mass transfer effects occurring in chromatographic processes.

3.2.1. Residence time distribution

A chromatography process does not only consist of the chromatographic device but also of peripherals, such as tubes, valves and sensors, which have an influence on the shape of the breakthrough curve and on the dynamic binding capacity of the process as well. According to the model of Carman-Kozeny the interstitial space in packed beds and membranes can be approached by capillaries. Therefore, this section also deals with the mass transfer in the mobile phase.

A mass balance around a radial segment of a tube results in the following equation, describing the change of concentration over time and space:

$$\frac{\partial c(x,r)}{\partial t} = D_{ax}\left(\frac{\partial^2 c}{\partial x^2} + \frac{\partial^2 c}{\partial r^2} + \frac{1}{r}\frac{\partial c}{\partial r}\right) - u(x,r)\frac{\partial c}{\partial x}. \tag{3.13}$$

The first term on the right site describes the dispersion in the tube, which is described in Section 3.2.5, and the second term describes convection. Solutions for

the concentration distribution are summed up and expanded by Ananthakrishnan, Gill and Barduhn [Anan1965] for different regimes which are characterized by the Bodenstein number (Bo). Three different regimes can be distinguished, which are each described by a model: Pure convection, axial dispersion and pure diffusion regime. The mathematical description can be found in the Appendix A.1.5. It is assumed, that the flow behavior in these three regimes can be described by two characteristics: The parabolic velocity profile in the tube and the molecular diffusion (D_0) in radial tube direction [Leve2011]. The flow behavior is well studied in literature [Bara2019]. The residence time distribution (RTD) in extra-column volumes for different molecule sizes and velocities was investigated. The peak shape approaches the profile of a pure convection tracer peak shape, with increasing molecular weight due to a lower diffusivity of the molecule. With increasing flow rate the peak shape tends to the shape of the dispersion model. The peak shapes for the transport regimes presented previously are presented in Figure 3.12.

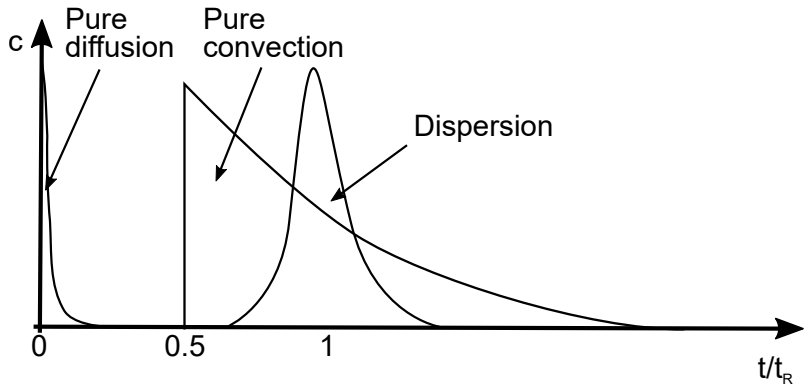

Figure 3.12.: Tracer curves for different regimes adapted from Levenspiel [Leve2011]

If the molecular diffusion is high, the parabolic velocity profile is distorted and the dispersion model is applied. For low molecular diffusion, the parabolic profile remains and is described by the pure convection model.

When the residence time distribution of a device is obtained experimentally, this is only realizable with the surrounding system of tubings and valves, leading to band broadening. Therefore, the measured residence time distribution data shows a deviation from the actual RTD of the device.
The impact of system an device on RTD is schematically shown in Figure 3.13.
The residence time distribution of the device can be determined by e.g. Fourier transformation, the one-dimensional dispersed plug flow model or the tank in series model by Martin and Synge [Mart1941]. Further information are given in Appendix

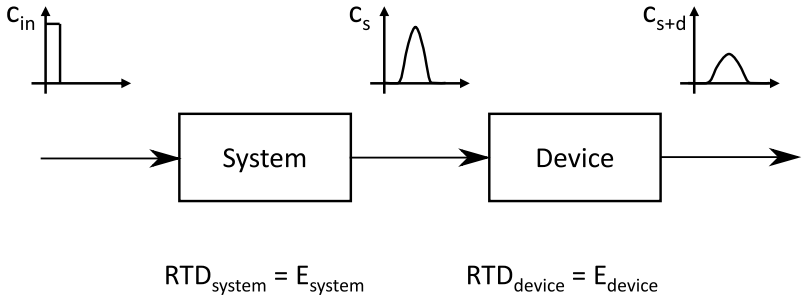

Figure 3.13.: Schematic of the experimental set-up consisting of the system (Äkta tubings and valves) and the device

A.1.5. As Fourier transformations often leads to a drastic increase of noise and the other two models do not fit skewed tracer peaks, Ham and Platzer developed an empirical model in order to allow a certain skewness of the distribution [Ham2004].

$$E(t) = \frac{MNt_k^N}{t^{N-1}} \cdot \left(1 - \frac{t}{t_{max}}\right)^{N-1} \cdot \left(1 - \frac{t_k^N}{t^N}\left(1 - \frac{t}{t_{max}}\right)^N\right)^{M-1} \tag{3.14}$$

where

$$t_k = \frac{t_{max} \cdot t_{min}}{t_{max} - t_{min}}. \tag{3.15}$$

The parameters t_{min}, t_{max}, N and M are pure fitting parameters.

3.2.2. Flow distribution in membrane adsorbers

Due to a high bed height to diameter ratio, also called aspect ratio, (h/d) in conventional column chromatography the impact of flow distribution on band broadening is low. In membrane chromatography on the contrary, h/d is low. Variations in the residence time distribution, resulting from feed distribution and collection contribute highly to broad tracer peaks and flat breakthrough curves. The efficiency of membrane adsorbers highly depends on the module design. In axial devices, the radial dimension usually is larger than the axial. In radial devices, the frontal area is usually larger than the bed height, cf. Figure 3.10 [Ghos2006]. With increasing bed height breakthrough curves sharpen and the influence of axial diffusion decreases: Due to higher pressure drop over the membrane the fluid is better distribution at the column inlet. [Suen1992; Liu1994]

3.2.3. Diffusion

Diffusion is the mass transport by random molecular motion meaning, that the molecules do not have a preferred direction of motion at constant concentration. Mathematically, diffusion in steady state is described by Fick's first law:

$$\frac{\dot{n}}{A} = -D \cdot \nabla c \tag{3.16}$$

The negative sign in Equation 3.16 results from the fact that diffusion occurs in the direction of decreasing concentration.
In case of time dependent diffusion, Fick's second law is applied:

$$\frac{\partial c}{\partial t} = D \cdot \nabla^2 c \tag{3.17}$$

For the notation of Equation 3.17 for cartesian, cylindrical or spherical coordinates see Appendix A.1.5. Crank [Cran1979] gives analytical solutions for Equation 3.17 for common boundary conditions and geometries, cf. Appendix A.1.5 and A.2. The free diffusion coefficient of molecules in a Newtonian fluid can be described by the Stokes-Einstein equation:

$$D_0 = \frac{k_B T}{6\pi\eta R}, \tag{3.18}$$

where k_B is the Boltzmann constant, T the temperature, η the dynamic viscosity and R the radius of the diffusing molecule.

Young et al. [Youn1980] developed a correlation for the prediction of the free diffusion of proteins, which is based on their molecular weight

$$D_0 = 8.34 \cdot 10^{-8} \cdot \left(\frac{T}{\eta \cdot M_W^{1/3}} \right), \tag{3.19}$$

where D_0 is in cm^2/s, the molecular weight M_W in $\mathrm{g/mol}$, the temperature in K and the dynamic viscosity in cP.

Pore diffusion

In porous structures or gels, the diffusive mass transfer is reduced due to interactions of the diffusing particle with the pore walls. This effect is called hindered diffusion. The mass transfer reducing effects are often lumped in the effective diffusion coefficient:

$$D_{\text{eff}} = \varepsilon_{\text{p}} \frac{D_0}{\tau} \tag{3.20}$$

in which ε the porosity of the porous media available for diffusion and τ the tortuosity.

In literature many models that describe the restricted diffusion into pores are presented. The molecule is approached by a rigid sphere. The case of diffusion in large liquid-filled pores a rigid sphere is modeled in a fluid continuum that fills the pores. The sphere is retarded due to the viscous drag of the fluid, affected by the proximity of the pore walls. A correlation proposed by Cussler [Cuss2009] is

$$\frac{D_{\text{eff}}}{D_0} = 1 + \frac{9}{8} \cdot \frac{R}{r_{\text{pore}}} \cdot \ln\left(\frac{R}{r_{\text{pore}}}\right) - \frac{3.082}{2} \cdot \frac{R}{r_{\text{pore}}}. \tag{3.21}$$

with the rigid sphere radius R and the pore radius r_{pore}.

Another model for the restricted diffusion of spherical molecules within cylindrical pores was developed by Renkin [Renk1954] and can be calculated with the following equation

$$\frac{D_{\text{eff}}}{D_0} = 1 - 2.104 \cdot \frac{R}{r_{\text{pore}}} + 2.09 \cdot \left(\frac{R}{r_{\text{pore}}}\right)^3 - 0.95 \cdot \left(\frac{R}{r_{\text{pore}}}\right)^5. \tag{3.22}$$

Gel diffusion

Ogston, Preston and Wells [Ogst1973] developed an empirical equation to describe the restricted diffusion in an array of fibres

$$\frac{D_{\text{eff}}}{D_0} = A \cdot \exp\left[-B \cdot \sqrt{\varphi}\right]. \tag{3.23}$$

Diffusion measurements showed that A is a constant close to one. The factor $B = \frac{(r_{\text{s}} + r_{\text{f}})}{r_{\text{f}}}$ is the sum of the Stoke's radius of the protein and the radius of the

polymer fiber divided by the fiber radius. φ is the polymer volume fraction. Another modification of the Ogston model, e.g. from Pluen et al. [Plue1999] or Johnson et al. [John1996] is

$$\frac{D_{\mathrm{eff}}}{D_0} = \exp\left(-\sqrt{\phi}\cdot\frac{r_{\mathrm{s}}}{r_{\mathrm{f}}}\right), \tag{3.24}$$

where ϕ is the fiber volume fraction.
A correlation for the restricted diffusion of a protein in agarose beads taking into account sterical hindrance is given by Boyer and Hsu [Boye1992]. This correlation is based on the molecular weight which is often more accessible than the hydrodynamic radius.

$$\frac{D_{\mathrm{eff}}}{D_0} = \exp\left(-A\cdot\left(M_{\mathrm{W}}^{1/3}+B\right)\cdot\sqrt{\phi}\right), \tag{3.25}$$

where the molecular weight is in $\mathrm{g/mol}$, $A = 0.1307$ and $B = 12.45$.

3.2.4. Film mass transfer

In conventional chromatography there is a film mass transfer resistance at the interface between the stream of mobile phase and the mobile phase which is inside the particle pores. Each particle is surrounded by a boundary layer where mass transfer only occurs by diffusion. The thickness of this layer depends on the fluid velocity [Guio1994]. Further information on the film theory is given in Appendix A.1.5. The resulting mass flow over the boundary layer is described by

$$\dot{m} = k_{\mathrm{f}}\cdot(c - c_{\mathrm{p}}(r = R)), \tag{3.26}$$

where c is is the bulk concentration and c_{p} the concentration at the particle's surface. The film diffusion coefficient k_{f} is defined by

$$k_{\mathrm{f}} = \frac{\rho\cdot D}{\delta}. \tag{3.27}$$

The correlation of Carberry [Carb1960] is valid for $\mathrm{Re} < 1000$

$$k_{\mathrm{f}} = 1.15\cdot u_{\mathrm{int}}\cdot \mathrm{Re}^{-1/2}\cdot \mathrm{Sc}^{-2/3}. \tag{3.28}$$

The penetration theory proposed by Bird et al. [Bird2015] describes the film mass transfer coefficient as

$$k_\mathrm{f} = \sqrt{\frac{4 \cdot D \cdot u_\mathrm{int}}{\pi \cdot d_\mathrm{p}}}. \tag{3.29}$$

Another approach is to calculate the film diffusion coefficient from the definition of the Sherwood number:

$$\mathrm{Sh} = k_\mathrm{f} d_\mathrm{p} / D_0. \tag{3.30}$$

Wilson and Geankoplis [Wils1966] developed equations to calculate Sh at very low Reynolds numbers in packed beds:

$$\mathrm{Sh} = \frac{1.09}{\varepsilon_\mathrm{c}} \cdot \mathrm{Re}^{1/3} \cdot \mathrm{Sc}^{1/3} \qquad \text{for} \quad 0.0015 < \mathrm{Re} < 55 \tag{3.31}$$

$$\mathrm{Sh} = \frac{0.25}{\varepsilon_\mathrm{c}} \cdot \mathrm{Re}^{0.69} \cdot \mathrm{Sc}^{1/3} \qquad \text{for} \quad 55 < \mathrm{Re} < 1050. \tag{3.32}$$

Here, the Reynolds number is calculated by $\mathrm{Re} = \rho u_\mathrm{int} d_\mathrm{p} / \eta$ and the Schmidt number by $\mathrm{Sc} = \nu / (\rho D_0)$. According to Guiochon, Golshan-Shirazi and Am Katti [Guio1994], the Reynolds number in liquid chromatography usually is lower than 0.1.

For $\mathrm{Re} < 100$ Kataoka and Yoshida [Kata1972] gives the following equation

$$\mathrm{Sh} = 1.85 \cdot \left(\frac{1 - \varepsilon_\mathrm{c}}{\varepsilon_\mathrm{c}} \right)^{1/3} \cdot \mathrm{Re}^{1/3} \cdot \mathrm{Sc}^{1/3}. \tag{3.33}$$

3.2.5. Dispersion

Dispersion is a phenomenon that summarizes all non-idialities leading to peak broadening. Dispersion in chromatography columns is caused by several effects [Goed2006b]:

- Wall effects cause a velocity gradient between molecules in proximity of the wall and molecules in the center of the column.

- The transition between cross-sections with different diameters leads to unequal distribution.
- Eddy diffusion describes the broadening of the signal due to different lengths of the stream lines the molecules take to flow through the column.
- The concentration gradient caused by the effects previously discussed, causes axial and radial diffusion.
- Figure 3.14 schematically shows the effect of dispersion: An initially sharp tracer pulse is quickly distorted by the parabolic velocity profile of the laminar flow.

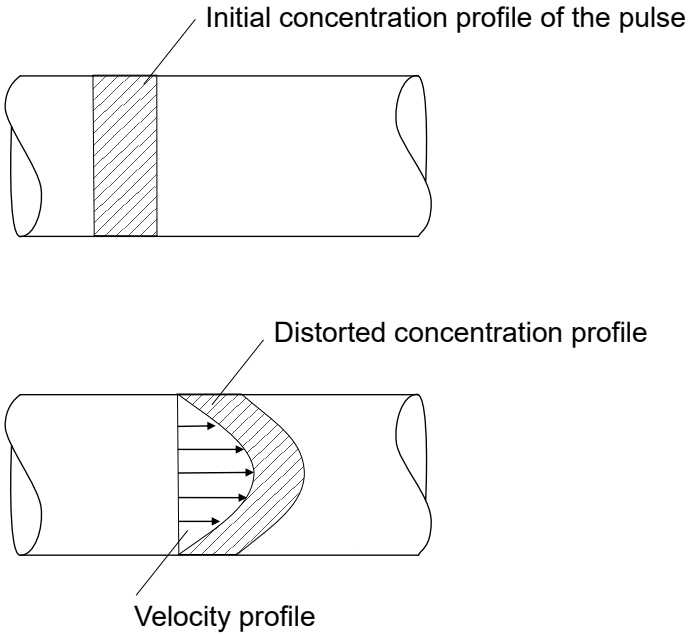

Figure 3.14.: Distortion of the concentration profile of a tracer pulse

Assuming the absence of diffusion the distortion continues and the pulse is widely dispersed when arriving at the measurement point. In case of rapid diffusion, the molecules in the center of the tube tend to diffuse outward into a region of slower moving solvent. Molecules form near the tube wall diffuse towards the tube center. Dispersion is described with mathematics similar to diffusion. In Equation 3.16 the diffusion coefficient has to be replaced by the dispersion coefficient. [Cuss2009; Bara2019]

The axial dispersion coefficient can be calculated with the following correlation [Schm2006]

$$D_{\mathrm{ax}} = \underbrace{\frac{\sigma_{\mathrm{t}}^2}{\mu_{\mathrm{t}}^2} \cdot L_{\mathrm{c}}}_{\mathrm{HETP}} \cdot \frac{u_{\mathrm{int}}}{2}. \tag{3.34}$$

Here, μ_{t} and σ_{t} are the first and second absolute moments, respectively. L_{c} is the length of the column and u_{int} the interstitial velocity.

3.3. Models for chromatography

Mathematical models are divided into physical models which rely on physical laws and empirical models that have no physical reference. Models can be used for the optimization of stationary phases, the scale-up and the validation of chromatographic processes. The main challenge is the determination and the proper interpretation of the model parameters [Jung1996]. Altenhöner et al. give an instruction on the determination of model parameters [Alte1997].

Chromatographic material is usually analyzed by either batch uptake experiments or breakthrough curve analysis. In batch uptake experiments, chromatographic material is stirred in a bulk volume. The concentration of the target molecule is measured over time. In breakthrough curve experiments, the chromatographic material is packed into a device and a solution flows through the bed. The concentration of the target molecule is measured at the column outlet. In literature batch uptake behavior or breakthrough curves using the models presented below were modeled:

- Simulations of batch uptake behavior give information on the mass transfer inside the porous particles and the static binding capacity [Hunt2000; Yu2014].
- The calculation of breakthrough curve profiles is used to determine effective diffusion coefficients and $\mathrm{DBC}_{10\,\%}$-values [Pabs2018]. Breakthrough curve predictions that are helpful for the evaluation of the process performance in scaled-up processes were performed for many combinations of target molecules, stationary phases and binding mechanism e.g. [Hunt2000; McCu2003; Vaňk2010].

- Lieres, Wang and Ulbricht developed an analysis tool (CADET) which is able to solve the most common chromatography models with different isotherms [Lier2010b]. Several authors investigated protein A or ion exchange membrane adsorbers using mathematical models: [Boi2008; Brie1992; Sarf1997; Suen1992; Yang1999].
- Membrane chromatography processes were e.g. modeled by Dimartino, Boi and Sarti [Dima2011], Gebauer, Thömmes and Kula [Geba1997] and Frerick et al. [Frer2008].

In this section a selection of physical chromatography models of different modeling depth is presented. A more detailed model overview is given by Guiochon, Golshan-Shirazi and Am Katti [Guio1994] and Schmidt-Traub [Schm2006]

3.3.1. Ideal model of chromatography

The ideal model of chromatography describes convection and adsorption equilibrium. Axial dispersion and mass transfer kinetics in the column are neglected:

$$\frac{\partial c_i}{\partial t} + \frac{1-\varepsilon_c}{\varepsilon_c}\frac{\partial q_i}{\partial t} + u\frac{\partial c_i}{\partial z} = 0 \tag{3.35}$$

The stationary phase concentration q is given by an isotherm equation. This model gives good results when large samples with highly efficient ($N >> 100$) columns are used, so that mass transfer kinetics and axial dispersion have a low contribution.

3.3.2. Equilibrium dispersive model

In dispersive models the contribution of mass transfer and all other non-idealities is described by one parameter D_{app}.

$$\frac{\partial c_i}{\partial t} + \frac{1-\varepsilon_c}{\varepsilon_c}\frac{\partial q_i}{\partial t} + u\frac{\partial c_i}{\partial z} = D_{app}\frac{\partial^2 c}{\partial z^2} \tag{3.36}$$

The lumped parameter D_{app} describes peak broadening effects due to the fluid dynamic in the system and all other mass transfer effects. Experiment and simulation are in good agreement, for highly efficient columns ($N >> 100$).

3.3.3. Lumped kinetic model

In order to consider adsorption kinetics, lumped rate models can be used. The equation for Langmuir kinetic is the following:

$$\frac{\partial c_{s,i}}{\partial t} = k_a \cdot (q_{s,i} - c_{s,i}) \cdot c_i - k_d \cdot c_i \tag{3.37}$$

In contrast to the other models, presented in this section, the lumped kinetic model only describes the adsorbent.
Adsorption on affinity chromatography material can be described by the Langmuir isotherm

$$q = q_{max} \cdot \frac{K \cdot c_p}{1 + K \cdot c_p}. \tag{3.38}$$

In this equation, q is the binding capacity, q_{max} the maximum binding capacity that is related to the static binding capacity (SBC), and $K = k_{ad}/k_{des}$ is the Langmuir coefficient.

3.3.4. General rate model

The general rate model is the most detailed continuous model [Guio1994]. The main assumptions made for the general rate model is, that the cross section of the column is homogeneous regarding interstitial volume, fluid flow and distribution of components. The radial transport is therefore neglected in the interstitial volume and only one spatial coordinate is needed in axial direction. As the bead radii are much smaller than the column radius and length, the beads are assumed to be continuously distributed inside the column.
The mass balance of the liquid phase (interstitial volume) includes accumulation, convection, axial dispersion and mass transfer through the liquid film outside the spherical particles.

$$\frac{\partial c}{\partial t} = -u_{int}\frac{\partial c}{\partial z} + D_{ax}\frac{\partial^2 c}{\partial z^2} - \frac{1-\varepsilon_c}{\varepsilon_c}\frac{3}{r_p}k_f\,(c - c_p) \tag{3.39}$$

The liquid phase in the porous beads is described e.g. by Li, Gu and Gu [Li1998] and includes adsorption kinetics, pore diffusion and surface diffusion:

$$\frac{\partial c_p}{\partial t}+\frac{1-\varepsilon_p}{F_{acc}\varepsilon_p}\frac{\partial}{\partial t}\sum_n q_n = D_p\left[\frac{\partial^2}{\partial r^2}+\frac{2}{r}\frac{\partial}{\partial r}\right]c_p+\frac{1-\varepsilon_p}{F_{acc}\varepsilon_p}D_s\left[\frac{\partial^2}{\partial r^2}+\frac{2}{r}\frac{\partial}{\partial r}\right]\sum_n q_n \quad (3.40)$$

The general rate model should only be used, when the mass transfer kinetics are slow, as many parameters are often not accessible. However, it gives good results, when large molecular compounds with slow mass transfer kinetics as e.g. IgG are described.

3.3.5. Modeling of extra-column volumes

Several authors worked on the mathematical modeling of the contribution of flow distribution on breakthrough curves. Extra membrane volumes, containing the external volume and the membrane void volume, are usually simulated using a continuously stirred tank reaktor (CSTR) and a dispersed plug flow reactor (DPFR) [Rope1995; Yang1999; Boi2007]. A more complex model, the so called zonal rate model, for the description of flow distribution in membrane adsorbers was developed by Lieres, Wang and Ulbricht [Lier2010b; Fran2011; Fran2012; Ghos2014].

3

4. Working methods

In this work, experimental and modeling parts are closely intermeshed. This chapter gives an overview on the working methods. The *Material and Methods* and the *Modeling* chapter are divided into three parts: The experimental investigation and modeling of the agarose structure, the optimization of the membrane structure and the modeling of chromatographic processes.

4.1. Agarose structure

The structure and characteristic parameters of agarose are shown in Figure 4.1.

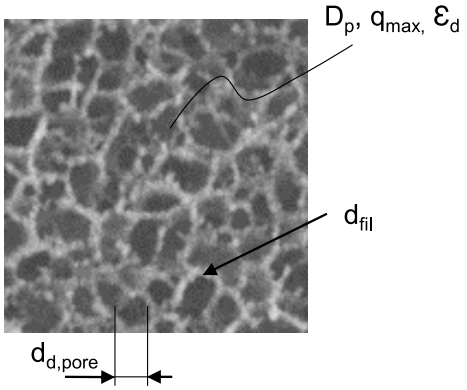

Figure 4.1.: Diffusive pore structure of agarose according to [Sart2020].

The parameters needed to describe the diffusive pore structure are determined by experimental methods and modeling, cf. Table 4.1. Experiments were performed with agarose beads. It is assumed that the agarose structure in beads and in the membrane bridges is equal.

Table 4.1.: Procedures for the determination of agarose parameters.

Parameter	Procedure	Section
ε_d	Inverse size exclusion experiments	Section 5.4
q_{max}	Breakthrough curve experiments	Section 5.7
D_p	Breakthrough curve experiments & modeling	Section 5.7.3

A model for the mathematical description of the agarose structure was developed, in order to describe the relation between the agarose filament diameter d_{fil}, the diffusive pore diameter $d_{d,pore}$ and the diffusive porosity ε_d. The so called *cubic grid model* for agarose is presented in Section 6.1.

4.2. Membrane structure

The limits of the membrane structure are confined by the maximum pressure drop over the membrane bed as well as by the diffusive accessibility of the membrane bridges and with that the degree of utilization of the binding sites. The parameters needed for the design of a membrane adsorber are shown in Figure 4.2.

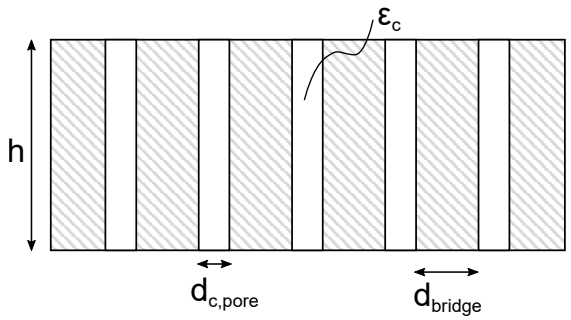

Figure 4.2.: Structure of the biporous membrane adsorber.

An overview on the optimization procedure of the membrane bed height h and the bridge diameter d_{bridge} is given in Table 4.2.

Table 4.2.: Procedures for the optimization of membrane parameters.

Parameters	Procedure	Section
h	RTD experiments & simulations	Section 5.7.1
d_{bridge}	Mass transfer approach and GRM	Sections 6.3.2 and 6.4

The correlation between d_{bridge}, $d_{\text{c,pore}}$ and ε_{c} is described with the cubic grid model for membrane adsorbers, cf. Sections 6.2 and 6.3.1. The optimization of d_{bridge} and ε_{c} for different agarose types is performed by modeling the membrane bed with the general rate model, cf. Section 6.4.

4.3. Model for chromatographic processes

The model of a chromatographic process consists of a model of the system which is composed of tubings and valves, a model of the housing and a model for the chromatographic bed. The combination of housing and chromatographic bed is called device. System and housing are each modeled with a continuously stirred tank reactor (CSTR) and a dispersed plug flow reactor (DPFR). For the description

of the chromatographic bed, the general rate model (GRM) is used. The model set-up and the necessary model parameters are presented in Figure 4.3.

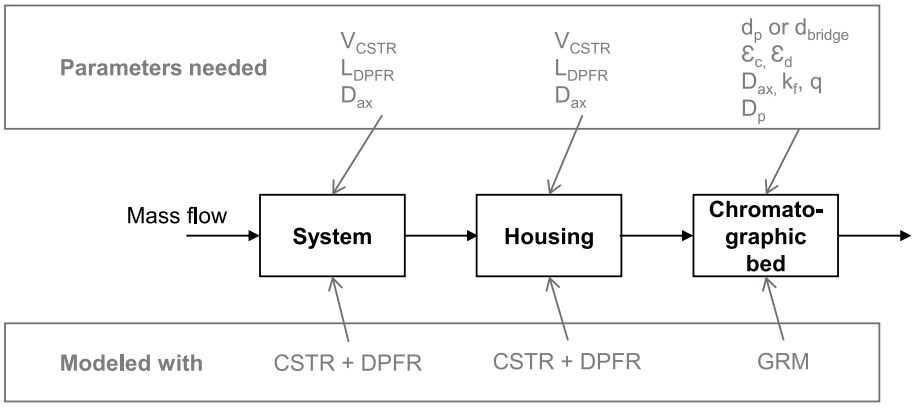

Figure 4.3.: Model for the simulation of membrane adsorbers or chromatography columns, including the needed model parameters.

In Table 4.3, the procedures for the determination of the model parameters are assigned to the respective sections.

Table 4.3.: Procedures for the determination of model parameters.

Sub-model	Parameters	Procedure	Section
System	V_{CSTR} L_{DPFR} D_{ax}	Tracer experiments	Section 5.7.1
Housing	V_{CSTR} L_{DPFR} D_{ax}	CFD simulations	Section 6.4.2
Chromatographic bed	d_p or d_{bridge}	Microscopy	Section 5.2
	D_{ax}	Tracer experiments	Section 5.7.2
	k_f	Equation 3.28	
	q	Equation 3.38	
	D_p	Parameter fitting	Section 5.7.3
	ε_p	iSEC	Section 5.4
	ε_c	Pressure-flow experiments or from production recipe	Section 5.5

The membrane devices were further investigated: Different device designs are compared, cf. Section 5.8. Models for the investigation of the influence of bed height, porosity and permeability on flow distribution are shown in Section 6.4.2.

5. Materials and methods

In this chapter the materials and the experimental methods used in this work are presented. At first, the buffer, tracers and target molecule which are needed in several experiments are presented. Then, the different stationary phases used in this work are described. Information on the chromatographic devices are given and the methods needed for the stationary phase investigation are shown.

5.1. Buffer, tracers and target molecule

In this section all chemicals needed in this work are summarized.

Phosphate-buffered saline (PBS), for composition, cf. Sambrook et al. [Samb1989], was used as the mobile phase buffer. The conductivity was $14.5\,\mathrm{mS/cm}$ and the pH of the buffer is 7.2 at $21°\mathrm{C}$.

Dextran standards of $5\,\mathrm{kDa}$, $25\,\mathrm{kDa}$, $80\,\mathrm{kDa}$, $270\,\mathrm{kDa}$ and $410\,\mathrm{kDa}$ were produced from Sigma Aldrich (catalogue numbers: 31417, 31419, 31421, 31423, 31424). The flourescein isothiocyanate-dextran (FITC-dextran) of $2000\,\mathrm{kDa}$ was obtained from TdB Consultancy.

Immunoglobulin G 1 (IgG 1) from an in-house Chinese Hamster Ovary (CHO) fermentation with a molar mass of $145{,}400\,\mathrm{Da}$ and an isoelectric point of 8.36 was used as an adsorbing antibody. IgG has a hydrodynamic diameter of $11.24\,\mathrm{nm}$ and its diffusion coefficient in free solution at $20\,°\mathrm{C}$ is $D_0 = 3.8 \cdot 10^{-11}\,\mathrm{m^2/s}$ [Boye1992]. The viscosity of IgG solutions is measured with a Haake Mars 60 device from Thermo Scientific (PP35-geometry with $0.8\,\mathrm{mm}$ gap height). To this end different IgG concentrations (1, 2.5, 5 and $20\,\mathrm{g/L}$) in PBS buffer were measured.

Before use, all buffers and samples were filtered using a $0.22\,\mu\mathrm{m}$ polyethersulfone bottle-top filter supplied by Sartorius.

5.2. Stationary phase investigation

5.2.1. Bead material

The beads used in this study were plain agarose beads from Agarose Bead Technologies, Spain: ABT $2\,\mathrm{wt\%}$ B Agarose Bead Standard ($50 - 150\,\mu\mathrm{m}$), ABT $4\,\mathrm{wt\%}$ B Agarose Bead Standard ($50 - 150\,\mu\mathrm{m}$) and ABT $6\,\mathrm{wt\%}$ B Agarose Bead Standard ($50 - 150\,\mu\mathrm{m}$), (catalog numbers: A-1020S, A-1040S and A-1060S).

5.2.2. Particle size

Bead diameters were determined manually from light microscope images. An MX51 microscope from Olympus was used, and images were analyzed using the software ImageJ2 version 2.35. For each particle size distribution, the mean particle diameter was determined from 80 beads each on three different images.

5.2.3. Membrane material

The characteristics of the membranes that were used in this study are summarized in Table 5.1.

Table 5.1.: Membrane characteristics of the membranes used in this study (*value taken from Sartorius data sheet)

Membrane	Material	Reinforcement material	ε_c	Used for
AM 1	Agarose	A	0.38	breakthrough curves + mechanic stability
AM 2	Agarose	B	0.38	mechanic stability
CM	Stabilized reinforced cellulose		0.8*	RTD in devices

5.2.4. Membrane bridge diameter

The membrane bridge is defined as the *diffusive stationary phase* of the membrane. The membrane bridge diameter distribution and the convective pore diameter distribution were determined according to the procedure presented in Ley et al. [Ley2018] using confocal microscopy.

5.3. Assembly of chromatography devices

5.3.1. Bead preparation and column packing

The beads were cross-linked by a standard procedure reported Demmer et al., Example 2 [Demm2016] in order to improve the mechanical stability. The protein A ligand was then coupled to the surface according to an established method performed by Johansson, Example 2 [Joha2002].

As chromatographic columns Tricorn 5/50 glass columns with a volume of $1\,\mathrm{mL}$ and a bed height of $35-59\,\mathrm{mm}$ from GE Healthcare were used and packed according to the Tricorn packing instructions. For each agarose concentration, a corresponding packing flow rate was determined. The procedure is specified in Bemberis, Noyes and Venkatesh [Bemb2003]. The column was considered well packed when the reduced HETP was $h = \mathrm{HETP}/d_\mathrm{p} < 3$ and the asymmetry factor $0.8 < \alpha < 1.6$, which are recommended values of the manufacturers [GE H2008].

5.3.2. Membrane devices

Throughout this work, different membrane devices were used and compared regarding their performance. A schematic representation of the LP15, which is an axial flow device, and the radial flow $3\,\mathrm{mL}$ Nano is given in Figures 5.1 and 5.2, respectively.

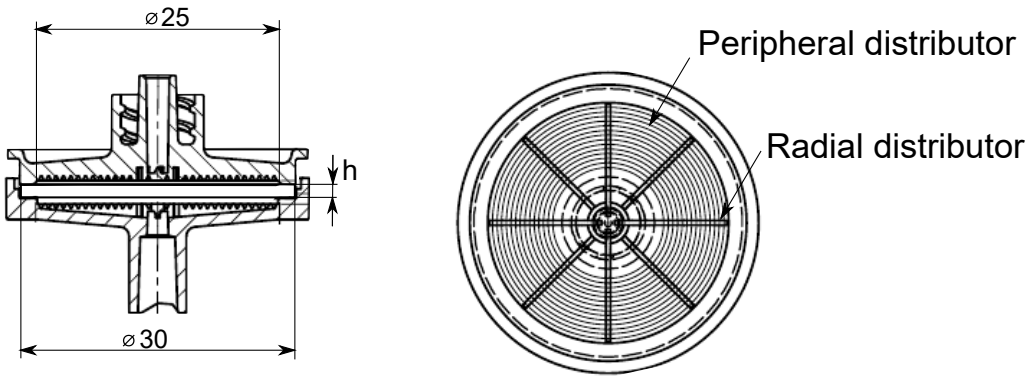

Figure 5.1.: Construction of the LP15 laboratory device (axial flow device). Units in mm. The usual bed height is $1\,\mathrm{mm}$ and membrane diameter is $26.4\,\mathrm{mm}$.

In a $1\,\mathrm{mL}$ Nano device, the bed height is reduced from $8\,\mathrm{mm}$ to $4\,\mathrm{mm}$. The occurring gap is filled up with fleece. Melting residues may occur during device assembly.

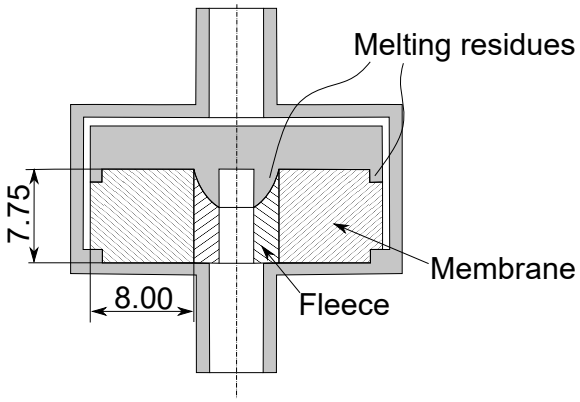

Figure 5.2.: Construction of the 3 mL Nano device (radial flow device). Units in mm. The usual bed height is 8 mm and bed length is 7.75 mm.

The ones shown here are a conservative case. In a 0.8 L device (800 mL), the bed height is kept at 8 mm but the width is increased from 7.75 mm to 450 mm.

5.4. Diffusive porosity and pore diameter

Diffusive porosities and accessibilities were determined by inverse size exclusion (iSEC) experiments using an HPLC (Ultimate 3000, Thermo Scientific). Therefore, the column was connected between the sampler and the UV detector using PEEK tubing, each with an inner diameter of $0.13\,\mathrm{mm}$ and a length of $250\,\mathrm{mm}$. Acetone and dextran were used as tracers. In order to eliminate effects of electrostatic interactions, inverse size exclusion measurements were performed with different salt concentrations. Due to interactions with the stationary phase, even under non-binding conditions, IgG peaks have not been performed. When interpreting the pore size diameters, the following has to be taken into account: According to Hagel et al. iSEC yields in a more narrow apparent pore size distribution and a lower average pore size than the pore sizes obtained with absolute methods [Hage1996]. However, this method is used, as it is well established and feasible.

The samples of $80\,\mu\mathrm{L}$ were dissolved in the mobile phase buffer (PBS) at a concentration of $2\,\mathrm{vol\%}$ (acetone) and $1\,\mathrm{mg/mL}$ (dextran). The flow rate was set to $0.2\,\mathrm{mL/min}$, resulting in a residence time of $\approx 5\,\mathrm{min}$. The tracer peak was monitored with an RI detector (Refracto Max 520, ERC). The retention volume of the system (tubing and valves) $V_{\mathrm{R,system}}$ and the retention in the system and the column $V_{\mathrm{R,system+column}}$ were determined with the first statistical moment. The retention volumes of the column were computed by subtraction: $V_{\mathrm{R}} = V_{\mathrm{R,system+column}} - V_{\mathrm{R,system}}$ [Schm2006]. The distribution coefficient is given by:

$$K_{\mathrm{D},i} = \frac{V_i - V_{\mathrm{int}}}{V_{\mathrm{c}} - V_{\mathrm{int}}}. \tag{5.1}$$

In this equation, V_i is the retention volume of the tracer molecule, V_{int} the interstitial volume, and V_{c} the column volume. The distribution coefficient presents the accessible particle porosity

$$\varepsilon_{\mathrm{p},i} = K_{\mathrm{D},i}. \tag{5.2}$$

Further information on distribution coefficients and pore diameters are given in Appendix A.3.

The pore size was determined with a model which describes the partitioning of the standard compounds into the pores. A model for mono-dispersed pores of different shapes is represented by the following equation [Yau1980], [Gorb1988]

$$K_{\mathrm{D}} = \varepsilon_{\mathrm{dex}} \left(1 - \frac{d_{\mathrm{h}}}{d_{\mathrm{pore}}}\right)^2. \tag{5.3}$$

The hydrodynamic radius in nm of the tracer molecule is estimated with the Mark-Houwink-Sakurada equation:

$$d_{\mathrm{h}} = 2k \cdot M^a, \tag{5.4}$$

where M represents the molar mass in Da. As dextranes are used as tracer molecules, the parameters are set to $k = 0.0271$ and $a = 0.498$ [Dubi1988].

5.5. Convective porosity

5.5.1. Column porosity

The column porosity was determined, using the experimental setup shown in Figure 5.3. Compressed air pressure was controlled by a pressure reducer, equipped with a Wika pressure gauge (No. 1135358, 0 - 2.5 bar). A 3 L stainless steel pressure vessel with pressure-reducing valve (Sartorius DJG SM 16663), initially filled with 1 L of buffer, was attached to the pressure reducer. The buffer was displaced by compressed air, exiting the pressure vessel through the pressure-reducing valve at its outlet. A Landefeld pressure gauge (DMGB 1 ES) was attached directly upstream of the column inlet to monitor the pressure at the column inlet with regard to atmospheric pressure. The pressure gauge and the column were then connected to the stainless steel vessel, whereas the column outlet was left open to atmospheric pressure. This enables the pressure drop in the column to be adjusted and kept constant in a range of ± 0.001 bar. The resulting flow rate was determined using a chronometer and a Sartorius balance (GC 1201-G, measurement error of $\leq \pm 0.005$ g).
The column porosity ε_{c} was then calculated with the Carman-Kozeny equation, Equation 3.7, as proposed in literature [Guio1994; Schm2006; Pabs2018].

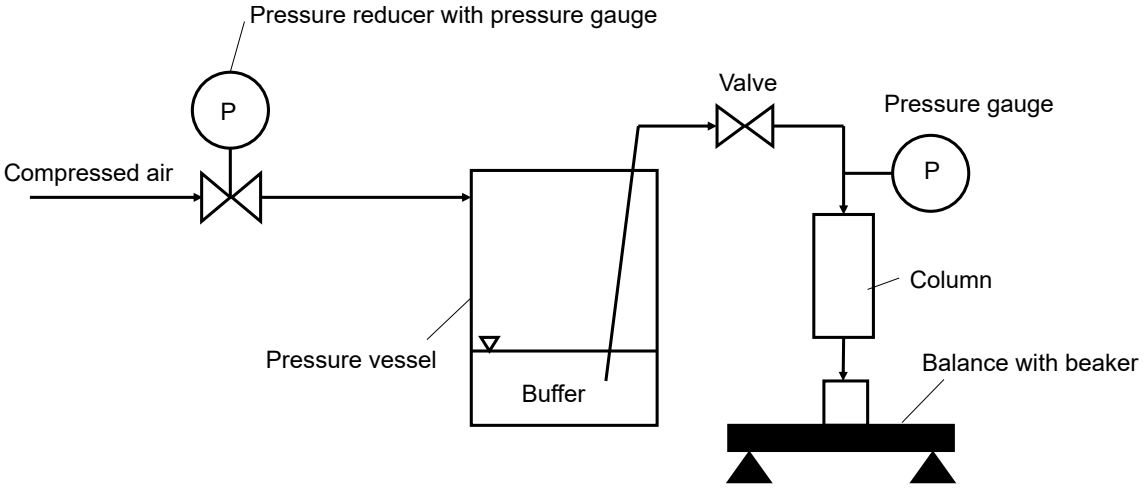

Figure 5.3.: Set-up for pressure-flow experiments

5.5.2. Convective porosity of membranes

The convective porosity of the membrane is determined from the production recipe. It is assumed, that the ratio of membrane bridges is equal to the volumetric ration of the agarose solution. The convective porosity of both agarose membrane types (AM1 and AM2) is 0.38.

5.6. Membrane stability

Stress-strain experiments are performed with the membranes AM1 and AM2 using an universal thickness gauge, product group S16502 from FRANK-PTI GmbH, Germany. The experimental set-up is given in Figure 5.4.

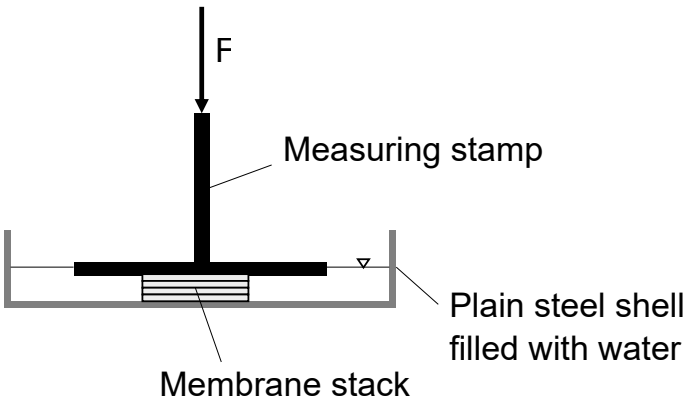

Figure 5.4.: Experimental set-up for stress-strain experiments. Area of the measuring stamp: 10 cm^2, weight of the measuring stamp: 25 g, membrane diameter: 8 mm.

The membrane was placed in the middle of the empty shell and the stamp without additional weight (25 g, assumed as zero-level) was brought into position. Water was added up to the height of the stamp. Additional weight was added (56 g, 130 g, 223 g, 376 g, 556 g, 1056 g and 1556 g). When the displayed value did not change for 60 s it was assumed to be constant.
The pressure, that leads to deformation is calculated from the applied force on the cross-sectional area of the membrane bridges and the reinforcement material:

$$\sigma = \frac{F}{A \cdot \varepsilon_{\text{min}}}, \tag{5.5}$$

where $F = m \cdot g$ is the force on the membranes, A the contact area between stamp and membrane and ε_{min} the minimum porosity which is calculated with Equation 6.8.

5.7. Breakthrough curves and mass transfer parameters

Breakthrough curves and mass tracer experiments for flow distribution and mass transfer determination were performed with an Äkta prime system (GE Healthcare Life Science, Sweden). The schematic set-up of the Äkta System is shown in Figure 5.5. Tubings, sensors and valves were washed up to the inlet valve. The tubings from the inlet valve to the column ($l = 270\,\text{mm}$, $i.d. = 0.75\,\text{mm}$) and from the column to the UV-detector ($l = 620\,\text{mm}$, $i.d. = 0.75\,\text{mm}$) influence dispersion. The concentration of the protein solution was $0.8\,\text{g/L}$. The concentration at the column outlet was measured on-line at 280 nm.

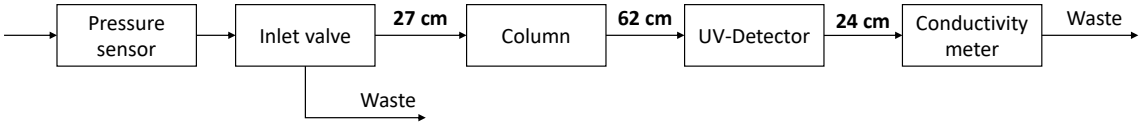

Figure 5.5.: Schematic representation of the Äkta system. The inner diameter of the tubings is 0.75 mm.

5.7.1. Hydrodynamics of the system

The hydrodynamics in the Äkta prime system were investigated using acetone and IgG tracers. Tracers are added, using a $100\,\mu$L injection loop. The volumetric flow rate is adapted to the one used with the devices, e.g. $0.2\,\mathrm{CV/min}$ for packed columns or $1\,\mathrm{MV/min}$ and $5\,\mathrm{MV/min}$ for membrane adsorbers.

5.7.2. Axial dispersion

The axial dispersion in the system was determined by the HETP of dextran with a molecular weight of $2000\,\mathrm{kDa}$. In this case, it is assumed that the dextran cannot enter the particle pores and therefore only experiences peak broadening in the interstitial column volume. Axial dispersion is calculated using Equation 3.34.

5.7.3. Pore diffusion and dynamic binding capacity

The pore diffusion coefficient is obtained by fitting the general rate model to experimental breakthrough curves. The CADET tool, developed by Lieres, Wang and Ulbricht was used [Lier2010b]. Breakthrough curves were recorded with an Äkta prime system at a flow rate of $\dot{V} = 0.2\,\mathrm{ml/min}$ for columns. This corresponds to a residence time of $\sim 6\,\mathrm{min}$.

Dynamic binding capacities at $10\,\%$ and $100\,\%$ are determined from breakthrough curves. For parameter fittings the initial value for the dynamic binding capacity at total breakthrough ($\mathrm{DBC}_{100\,\%}$) is calculated from the area above the breakthrough curve and is adjusted to describe the breakthrough curve as accurately as possible. The adsorption is described with the Langmuir isotherm, cf. Equation 3.38. The Langmiur coefficient K is adopted from Pabst, Thai and Hunter [Pabs2018] for protein A resins.

5.8. Residence time distribution of membrane devices

The hydrodynamics in the membrane device is evaluated by the residence time distribution of an acetone tracer signal. The RTD of different devices was analyzed, cf. Table 5.2. Due to the size variation, different chromatographic systems

equipped with an injection loop were used. The tracer solution has an acetone content of 2 vol% in PBS buffer.

Table 5.2.: System device combinations for the determination of the hydrodynamics in the device

Device	System	Signal
LP15 laboratory device	Äkta Prime (GE Healthcare)	Impuls of 100 μL
1 mL Nano	Äkta Prime (GE Healthcare)	Impuls of 100 μL
3 mL Nano	Äkta Prime (GE Healthcare)	Impuls of 100 μL
0.8 L Capsule	Hipersep Bio M ILD Pack II (Novasep)	Step signal

For the comparison of the residence time distribution in different devices, CM membranes were used, cf. Table 5.1. In contrast to the agarose membranes, which were still under developement, CM membranes were available in different device sizes.

In order to consider the influence of the system and the device separately, one tracer peak was performed over the system, another was applied on the system and the membrane device, cf. Section 3.2.1. The resulting residence time distribution for the device describes the hydrodynamics of the device. The RTD of the device is calculated by the deconvolution of the input and the output concentration of the device c_s and c_{s+d}, respectively. In order to avoid the drastic increase of noise by using Fast Fourier Transformation, the correlation of Ham et al., Equation 3.14 for the E-curve, and the experimental procedure of Boskovic et al. are used to separate the influence of the system from the device [Ham2004; Bošk2008]. The parameters in Equation 3.14 are obtained by fitting the result of the convolution of $c_s * E_{device}$ to experimental data c_{s+d}, using the method of non-linear least-squares.

6. Modeling

In this chapter the models used in this work are presented. It can be distinguished between simple geometric models for the description of the agarose and the membrane structure, time and space dependent mass balances for the description of the chromatographic bed and CFD models for fluid distribution in membrane devices.

The used membranes consist of a biporous agarose structure. The convective pores allow a fast convective mass transfer through the membrane and diffusive pores inside the so called membrane bridges generate a high specific surface, cf. Figure 6.1. To increase the mechanical stability, the biporous agarose structure is applied on reinforcement material which occupies $\approx 15\,\%$ of the bed volume.

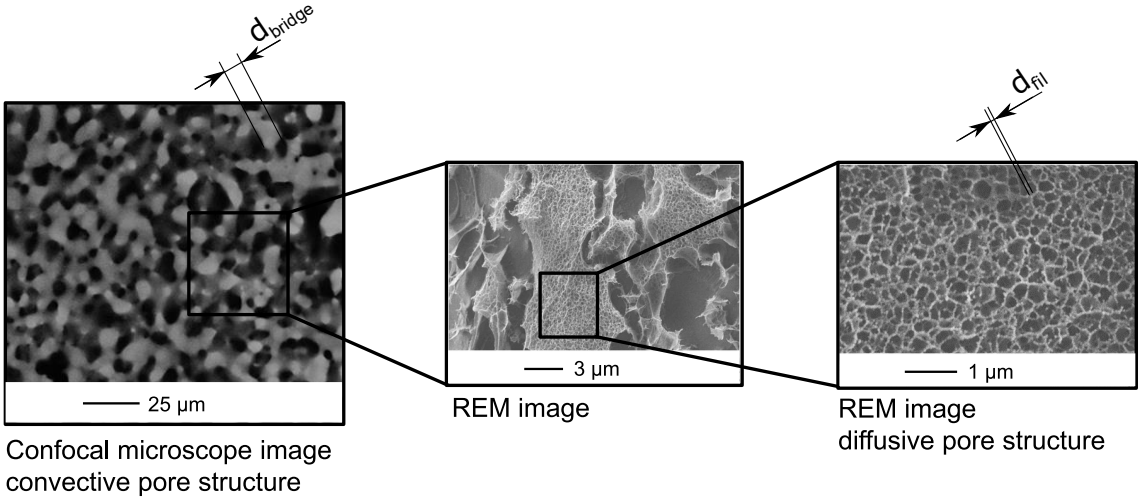

Figure 6.1.: Internal membrane structure with convective and diffusive pores [Sart2020].

For the process simulation and the optimization of the membrane material, different agarose types have been used. Their characteristics are summarized in Table 6.1.

Table 6.1.: Potential agarose membranes with different agarose structures, used for the process optimization. Material A membrane is a potential membrane with PrismA characteristics. *Values taken from results in Chapter 7, **values based on the binding capacity of PrismA material, cf. Appendix A.2.2.

Agarose type	D_{eff} $[\text{m}^2/\text{s}]$	ε_{p} $[\text{mol}/\text{m}^3]$	q
Material A membrane	$1.2 \cdot 10^{-12}$	0.50	1.87
AM1 model membrane	$0.9 \cdot 10^{-12}$	0.69	0.63
2 wt% agarose	$6.50 \cdot 10^{-12}$*	0.63*	0.68**
4 wt% agarose	$5.72 \cdot 10^{-12}$*	0.58*	1.49**
6 wt% agarose	$3.96 \cdot 10^{-12}$*	0.47*	1.98**

6.1. Cubic grid model for the diffusive pore structure

The agarose gel is described using a cubic grid structure, which is schematically shown in Figure 6.2. The cubic grid structure was proven to be a suitable model.

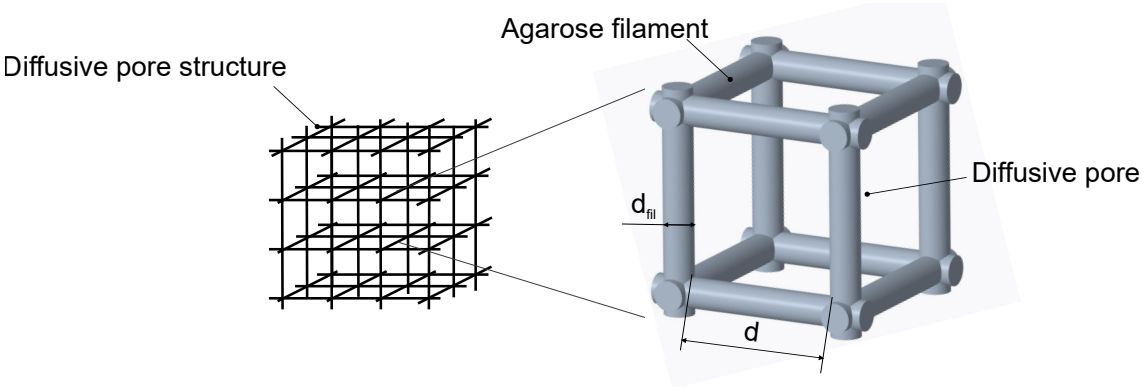

Figure 6.2.: Schematic representation of the agarose gel filament structure, according to [Hage2020]

This grid consists of equal cylinders with the diameter d_{fil}. The distance between two parallel cylinders d can also be interpreted as the diameter of diffusive pores. If one of these two diameters and the agarose concentration is known, these parameters can be used to deduce the other diameter

$$V_{\text{fil}} = N_{\text{cylinders}} \cdot \left(\frac{\pi}{4} \cdot d_{\text{fil}}^2 \cdot d + \underbrace{\frac{1}{3} \cdot d_{\text{fil}}^3}_{\text{Volume nods}} \right). \tag{6.1}$$

The filament volume V_{fil} is described by the following equation

$$V_{\text{fil}} = \underbrace{(1 - \varepsilon_{\text{p}})}_{\phi} \cdot V_{\text{agarose}}. \tag{6.2}$$

Based on the equation proposed in the study published by Pluen et al. [Plue1999], the volume fraction of agarose filaments, ϕ, is obtained

$$\phi = \frac{c_{\text{agarose}}}{\varphi_{\text{agarose}} \cdot \omega_{\text{agarose}}}, \tag{6.3}$$

where c_{agarose} is the concentration of agarose in the gel (w/v), $\varphi_{\text{agarose}} = 1.64\,\text{g/ml}$ the dry agarose density according to Laurent and $\omega_{\text{agarose}} = 0.625$ the mass fraction of agarose in a filament according to Johnson et al. [Laur1967] [John1995].

The number of cylinders is defined by

$$N_{\text{cylinders}} = \underbrace{3}_{\substack{\text{Cuboid has 12 edges} \\ \text{shares them with 4 other}}} \cdot \underbrace{\left(\frac{V_{\text{agarose}}^{\frac{1}{3}}}{d + d_{\text{fil}}} \right)^3}_{\substack{\text{Amount of cuboids} \\ \text{in agarose volume}}}. \tag{6.4}$$

Model input parameters are e.g. c_{agarose} and d_{fil}. The output parameter is then the pore diameter d. Agarose filament diameters have been examined by several authors in literature, as described in Table 3.1. The resulting specific surface of the agarose network-structure is then expressed by

$$S_{\text{V}} = \frac{N_{\text{cylinders}} \cdot \pi \cdot d_{\text{fil}} \cdot d}{V_{\text{Agarose}}}. \tag{6.5}$$

The specific surface is transformed into the load q by multiplying with the specific adsorptive surface density of antibody-immobilized film ρ_{s} (mass that is bound per surface):

$$q = S_{\text{V}} \cdot \rho_{\text{s}}. \tag{6.6}$$

The specific adsorptive surface density of antibody-immobilized film highly depends on the used protein A ligand. For protein A, the surface density is indicated with

$\rho_s = 16.82\,\mathrm{mg/m^2}$ [Dubr1995]. In this work, $\rho_s = 22\,\mathrm{mg/m^2}$, corresponding to PrismA material, is used [Pabs2018]. This state of the art surface density is primarily used in this work for the simulation of membrane adsorbers to describe their potential.

6.2. Models for the membrane structure

The law of Hagen-Poiseuille is used to describe the flow through a membrane, cf. Equation 3.9. Assumptions are, that the membrane consists of parallel capillaries, the flow is laminar and the fluid is Newtonian. The law of Hagen-Poiseuille is used in this work along with Darcy's law, cf. Equation 3.10, for estimations of the pressure loss over the membrane.

According to Figure 6.1, the convective pore structure can also be described by a cubic grid structure, similar to the one presented in Section 6.1. In this case the cylinders at the cube edges refer to the membrane bridges and the diameter d to the convective pore diameter $d_{c,pore}$. The resulting porosity is referred to as the maximum porosity of the membrane ε_{max}. The maximum porosity of the membrane is defined as

$$\varepsilon_{max} = 1 - \frac{3 \cdot \pi \cdot d_{bridge}^2 \cdot d_{c,pore} + 4 \cdot d_{bridge}^3}{4 \cdot (d_{c,pore} + d_{bridge})^3}. \tag{6.7}$$

The porosity in the definition of the permeability, cf. Equation 3.9, is the porosity of a volume with cylindrical pores, referred to as the minimum porosity of the membrane ε_{min}:

$$\varepsilon_{min} = \frac{\frac{\pi}{4} d_{c,pore}^2 \cdot h \cdot N}{V_{membrane}}. \tag{6.8}$$

6.3. Models for the membrane design

6.3.1. Pressure drop approach

The pressure drop of the total membrane bed is calculated with Equation 3.10. Combining Equation 3.9 with Equation 3.10 a correlation between permeability and convective pore diameter results:

$$P = \frac{d_{c,pore}^2 \cdot \varepsilon_{min}}{32}. \tag{6.9}$$

The porosity in this equation is the minimum porosity of the membrane, as the law of Hagen-Poiseuille considers tube flow, cf. Section 6.2. The cubic grid model for membranes, presented in Section 6.2, is used to transform volume porosity of the membrane into its surface porosity and vice versa.

The bridge diameter depends on the convective porosity of the membrane adsorber. The proportion of stationary phase in the membrane is defined by the maximum allowed pressure drop in the device. Given Equation 3.10, the minimum permeability of the membrane stack is calculated for a bed height of $8\,\mathrm{mm}$ and maximum pressure drop of $2\,\mathrm{bar}$. The correlation between bridge diameter and convective porosity is calculated using Equation 6.9 and the correlation between pore and bridge diameter, which is based on the cubic grid model, cf. Equation 6.7.
The optimum convective porosity and the corresponding membrane bridge diameter are calculated for the configurations presented in Table 6.1 and for different volumetric flow rates. The impact of the membrane stability on the convective pore diameter is considered by

$$d_{c,pore} = \sqrt{\frac{d_{c,0}^2 \cdot \left(1 - \frac{1-\varepsilon}{\varepsilon_c}\right)}{\varepsilon}}. \tag{6.10}$$

The derivation is presented in Appendix A.3.2.

6.3.2. Mass transfer approach for the membrane bridge design

The bridge diameters, which defines half of the diffusive pathway, for 2 wt%, 4 wt% and 6 wt% agarose membranes are designed.
The bridge diameter can be quickly estimated by the diffusive mass transfer inside the bridges. This approach neglects all convective mass transport in the convective pores. The mass balance around the bridges is given by

$$\frac{\partial c_\mathrm{p}}{\partial t} + \frac{(1-\varepsilon_\mathrm{p})}{\varepsilon_\mathrm{p}} \cdot \frac{\partial q}{\partial t} = D_\mathrm{eff} \cdot \nabla^2 c. \tag{6.11}$$

The load q is characterized with the Langmuir isotherm, Equation 3.38. The diffusion coefficient in the material and the porosity for IgG are taken from the investigation of the agarose beads in Section 7.2. The binding capacity is calculated from the specific adsorptive surface density and the specific surface that is available for binding. The values are summarized in Table 6.1.
In order to consider borderline cases the geometry of the bridges is approached by slabs on the one hand and spheres on the other. The nabla operator has to be adapted according to the geometry, cf. Appendix A.1.5. Dirichlet boundary conditions with a constant concentration of 1 g/L at the boundary are taken. Equation 6.11 then becomes a non-linear ordinary differential equation. Using the implicit Euler method, a non-linear equation is solved with the Newton method and a Jacobi matrix.

When convective mass transfer in the membrane bed is considered for the estimation of the bridge diameter, the general rate model, cf. Equations 3.39 and 3.40, is solved for cartesian and spherical coordinates. Only the adsorptive bed is considered. The used parameter set for the simulation is summarized in Table A.6 in the appendix.

6.4. Modeling of breakthrough curves

The model which is used for the modeling of breakthrough curves is shown in Figure 4.3. The system and the housing are modeled each with a combination of a CSTR and a DPFR. In the system, the CSTR describes back mixing and dead volumes e.g. due to valves, whereas tubes are represented by the DPFR

[Sarf1997]. Parameters for CSTR and DPFR are fitted with the CADET software version 4.0.1 (mex) using Matlab R2019a to experimentally obtained acetone and IgG curves. The housing is only considered in membrane chromatography, cf. Section 6.4.2. The chromatographic bed is described with the general rate model. The time, available for the diffusion is the effective residence time in the membrane, which is assumed by

$$\tau_{\text{eff}} = \frac{V \cdot \varepsilon_{\text{c}}}{\dot{V}}. \tag{6.12}$$

6.4.1. Resin chromatography

In the model that describes the resin bed, the fluid distribution is neglected. This assumption can be made, as the considered columns have a large length to diameter ratio. To describe breakthrough curves, the model of the system is extended with the general rate model (Equations 3.39 and 3.40). Danckwerts boundary conditions are assumed at the column inlet and outlet. The mass transport through the stagnant film around a bead is equal to the diffusive transport into the beads and a symmetry condition was applied at its center [Lier2010a]. The resulting system of non-linear partial differential-algebraic equations (PDAE) was solved with the CADET software. Initial and boundary conditions are listed in Appendix A.2.3.

Langmuir adsorption kinetic is chosen to describe the affinity binding between protein A and IgG. This rather simple approach is not able to describe the behavior occurring close to complete saturation which are considered to be influenced by steric hindrance effects [Jung1996; Jin1994]. In order to minimize the influence of this effect, model parameters are fitted up to 80% of the total breakthrough, which is a procedure commonly applied [Dima2011]. This is the reason why the binding capacity at total breakthrough of the experimental and simulated data vary from one another. For an affinity binding mechanism it is assumed that the target molecules bind permanently at their binding site. The surface diffusion coefficient is therefore set to zero.

6.4.2. Membrane chromatography

In contrast to conventional chromatography columns, the hydrodynamics in membrane adsorber devices are much more important, because the frontal area of a membrane device is larger than the flow-through length. When modeling a membrane adsorber, the flow distribution has to be considered.

Hydrodynamics in the LP15 device

As simulative approach, CFD simulations of the LP15 laboratory device with COMSOL Multiphysics, version 5.5 (COMSOL AB, Burlington, MA) were performed. The needed modules for the simulations are the *CAD Import Module*, the *CFD Module* and the *Chemical Reaction Engineering Module*. The influence of bed height, porosity and permeabilty at a flow rate of $5\,\mathrm{MV/min}$ on the residence time distribution were investigated and the parameter sets are presented in Table 6.2. The area at the inlet of the device is $4.91\,\mathrm{mm}^2$ and the volume of the tracer peak is $0.1\,\mathrm{mL}$.

Table 6.2.: Parameter variations for CFD simulations. Constant membrane area at $5\,\mathrm{cm}^2$

Bed height [mm]	Flow rate [mL/min]	Inlet velocity [m/s]	Pulse length [s]	Porosity	Permeability [mD]
				0.30	100
1	5	0.009	2.260		50
				0.38	100
					500
				0.50	100
4	20	0.036	0.565	0.38	100
8	40	0.072	0.283	0.38	100
12	60	0.108	0.188	0.38	100

The simulations of the membrane adsorber devices were performed in a 3D space dimension. The inverse geometry, which refers to the volume which is filled with fluid and membrane, cf. Figure 6.3, is imported into COMSOL. Due to symmetry, only one eighth of the geometry is used, to save computing time without influencing the results.

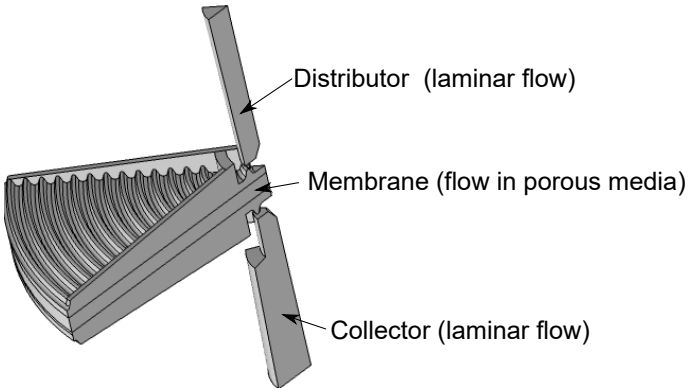

Figure 6.3.: Inverse geometry of the LP15 laboratory device which corresponds to the cavities in the device used in CFD simulations.

In order to model the behavior of a tracer substance inside the device, a stationary study is performed. Based on the calculated stationary state, a time-dependent study for the transport of the tracer molecules through the device is implemented. The flow in the housing, which consists of the distributor and the collector, is described with laminar flow, as the Reynolds number ($\mathrm{Re} = u\rho\eta^{-1} \cdot \sqrt{P \cdot \varepsilon^{-1}}$) is < 2300. The membrane is simulated using the physics *porous media*, the Brinkman equation, cf. Appendix A.3.3 and no-slip conditions ($u_{\mathrm{wall}} = 0$). Tracer peaks are implemented with the physics *transport of diluted species*. Water is used as medium and $2\,\mathrm{v}\%$ acetone with a diffusion coefficient of $D_{\mathrm{acetone}} = 1.303 \cdot 10^{-9}\,\mathrm{m}^2/\mathrm{s}$ is used as tracer molecule [Ande1958]. Although the size of the tracer molecule has an influence on the shape of the residence time distribution in tubes, cf. Baran et al. [Bara2019], the simulated RTD of the device are not significantly influenced by the tracer molecule size, cf. Figure A.9 in the appendix. Therefore, RTD simulations with acetone can be used to describe the distribution of IgG.

A physics defined mesh consisting of a *free tethraethal* mesh, corner refinement and boundary layers was used. The mesh is calibrated for fluid dynamics and its element size parameters are shown in Table 6.3.
Those parameters are found to be sufficiently accurate with regard to computing expenses.

In order to investigate the impact of hydrodynamics in the membrane housing and separate it from the impact of the membrane, CFD simulations are performed with a complete device and with the membrane. For the simulation of the membrane residence time distribution, the tracer is given directly on the membrane surface.

Table 6.3.: Mesh parameters for a LP15 device.

	LP15 device
Maximum element size	0.405 mm
Minimum element size	0.0437 mm
Maximum element growth rate	1.1
Curvature factor	0.4
Resolution of narrow regions	0.9

The COMSOL model is structured in the same way as the model for the whole device. The RTD of the housing is calculated according to Section 3.2.1, using the model of Ham and Platzer [Ham2004]. In order to describe the influence of the hydrodynamics on breakthrough curves the RTD of the housing is modeled using a DPFR and a CSTR. The equivalent circuit is fitted to the RTD of the housing with the CADET software, version 4.0.1 with Matlab 2019a.

Hydrodynamics in the Nano device

The simulations were performed similar to procedure described in Section 6.4.2 for a 3 mL Nano device, cf. Figure 6.4. The fleece that is integrated in the device is simulated using *porous media* with a porosity of 0.8 and a permeability of 3000 mD. The final mesh parameters after a mesh study are summarized in Table 6.4.

Table 6.4.: Mesh parameters for a 3 mL Nano device.

	3 mL Nano
Maximum element size	0.288 mm
Minimum element size	0.0188 mm
Maximum element growth rate	1.08
Curvature factor	0.3
Resolution of narrow regions	0.95

Modeling of the membrane bed

In order to describe the stationary phase in membrane beds, plates instead of particles are assumed, cf. Appendix A.2.1, resulting in:

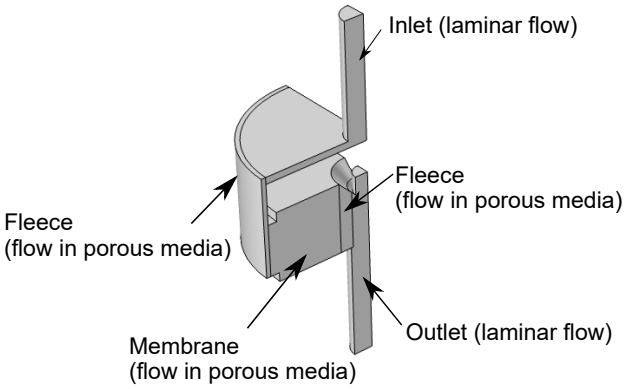

Figure 6.4.: Inverse geometry of the 3 mL Nano device which corresponds to the cavities in the device used in CFD simulations.

$$\frac{\partial c}{\partial t} = -u_{\text{int}}\frac{\partial c}{\partial z} + D_{\text{ax}}\frac{\partial^2 c}{\partial z^2} - \frac{1-\varepsilon_{\text{c}}}{\varepsilon_{\text{c}}} \cdot \frac{1}{L} \cdot k_{\text{f}}\left(c - c_{\text{p}}\right) \tag{6.13}$$

$$\frac{\partial c_{\text{p}}}{\partial t} + \frac{1-\varepsilon_{\text{p}}}{F_{\text{acc}}\varepsilon_{\text{p}}}\frac{\partial}{\partial t}\sum_{n} q_{\text{n}} = D_{\text{p}}\frac{\partial^2}{\partial x^2} + \frac{1-\varepsilon_{\text{p}}}{F_{\text{acc}}\varepsilon_{\text{p}}} \cdot D_{\text{s}}\frac{\partial^2}{\partial x^2} \tag{6.14}$$

The interstitial velocity in packed beds and axial membrane devices is constant over the device length. In radial flow devices, the interstitial velocity changes with the flow-through length. For the simulation of radial devices, the mean interstitial velocity is calculated using

$$u_{\text{int}} = \frac{\dot{V}}{A} \tag{6.15}$$

$$\bar{u}_{\text{int}} = \frac{1}{r_1 - r_2} \cdot \int_{r_2}^{r_1} \frac{\dot{V}}{2\pi r L}\mathrm{d}r \tag{6.16}$$

$$= \frac{1}{r_1 - r_2} \cdot \frac{\dot{V}}{2\pi L} \cdot \ln\frac{r_1}{r_2}. \tag{6.17}$$

6.5. Membrane adsorber process

Breakthrough curves of the membrane bed are calculated with the optimal bridge diameter for each convective porosity for a maximum pressure drop of 2 bar using

the general rate model. Effects of the system and the device hydrodynamic are not taken into account at this point.
In this work a simplified model process is presumed. The following assumptions were made:

- A cycle consists of the following steps: Equilibration, load, wash, elution and wash, cf. Section 3.1.1. The first washing step includes buffer changes. In the second washing step a CIP step, pH shifts and buffer changes are included. The required volumes for a membrane and a resin process are shown in Table 6.5. The reason for the difference between membrane and resin process volumes is the different fluid dynamic in device and column.
- The flow rate is constant throughout the process and adapted to the flow rate of the loading step
- The recovery of the process is $100\,\%$
- Only process times are considered. Changes over time are not taken into account
- The membrane adsorber has a volume of $1\,\mathrm{L}$ and the feed concentration ranges from $1 - 10\,\mathrm{g/L}$
- The load step is terminated, when $1\,\%$ breakthrough are reached

The productivity of the process is calculated with Equation 3.1.

Table 6.5.: Process volumes for membrane and resin processes. *Resin process volumes are based on GE data sheets.

Step	Membrane [MV]	Resin* [CV]
Equilibration	5	3
Wash	5	6
Elution	5	3
Wash	10	6

7. Optimization of the agarose structure

Parts of this chapter have been published as:

Franziska Hagemann, Patrick Adametz, Matthias Wessling, Volkmar Thom
Modeling hindered diffusion of antibodies in agarose beads considering pore size reduction due to adsorption
Journal of Chromatography A, 2020
doi.org/10.1016/j.chroma.2020.461319

In this chapter, the agarose structure is investigated using resin material. The cubic grid model is used to calculate equilibrium binding capacities. Diffusive porosities and pore diffusion coefficients are determined for different agarose concentrations. At the end of this chapter, the $DBC_{10\,\%}$ for different target molecule sizes are compared for three different agarose concentrations and the optimized agarose concentration for the target molecules is discussed.

7.1. Prediction of the equilibrium binding capacity

In this section, the influence of modification and adsorption on the agarose filament diameter and the filament volume fraction is investigated. With the cubic grid model, cf. Section 6.1, diffusive pore diameters, filament volume fractions and static binding capacities are calculated.
By fitting the model to experimental data using the method of linear least squares, the filament diameter is deduced. This filament diameter consists of the agarose filament which is cross-linked and coupled with protein A. In Figure 7.1, the model for different filament diameters is compared with experimental data from Pabst et al. [Pabs2018]. A filament diameter of $16\,\mathrm{nm}$ in Equation 6.5 fits best with the experimental data.
As the agarose concentration decreases, the pore size increases. This results in a decreasing surface and, therefore, the binding capacity drops. Deviations of the model from the experimental data have two main reasons: On the one hand, the model used is a simple geometric approach in which all pores have the same pore size. Therefore, in the model, either the molecule fits into the pore and all binding sites are available or the molecule is excluded and no binding sites are reachable at all. On the other hand, the model cannot describe the complex influence of surface modifications, such as ligand coupling.
Due to the specific interaction between protein A and IgG and the high binding constant, it is assumed that IgG adsorbs immediately and permanently to a free binding site. The adsorption process of IgG in the porous particles can be described with the shrinking core model based on pore diffusion and an irreversible isotherm. The adsorption occurs on the outer part of the particle first, then the adsorptive region moves into the particle. For protein A resins, this means that the IgG entering the pore first, adsorb directly at the pore inlet. All following IgG diffuse into a pore with a reduced pore diameter and adsorb at the first available binding

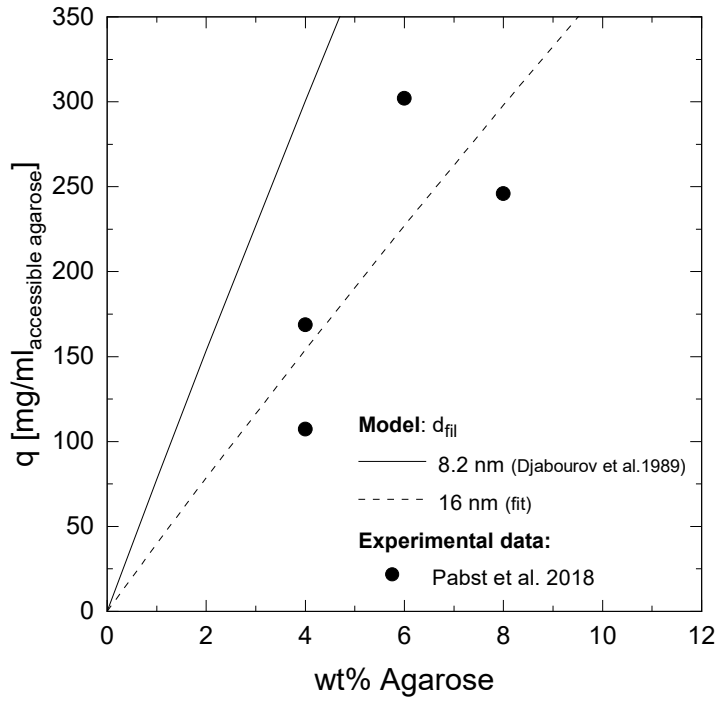

Figure 7.1.: Load of accessible agarose volume calculated with the agarose gel model: Comparison of experimental data [Pabs2018] with cubic grid model, cf. Section 6.1. The specific adsorptive surface density was assumed to be $\rho_s = 16.82\,\mathrm{mg/m^2}$.

sites. The adsorption of IgG leads to further increase in the filament diameter, which is called apparent filament diameter, $d_{\text{fil,apparent}}$.
Figure 7.2 shows pore diameters for the apparent filament diameters, calculated using the cubic grid model. Moreover, the experimental results from iSEC are added, which are smaller than the ones obtained with the model. This effect is consistent with the statement above that lower pore sizes and lower particle porosities are obtained with iSEC [Hage1996]. The adsorption of IgG leads to $d_{\text{fil,apparent}} = (d_{\text{fil}} + 2d_{\text{IgG}}) = 38.48\,\text{nm}$.

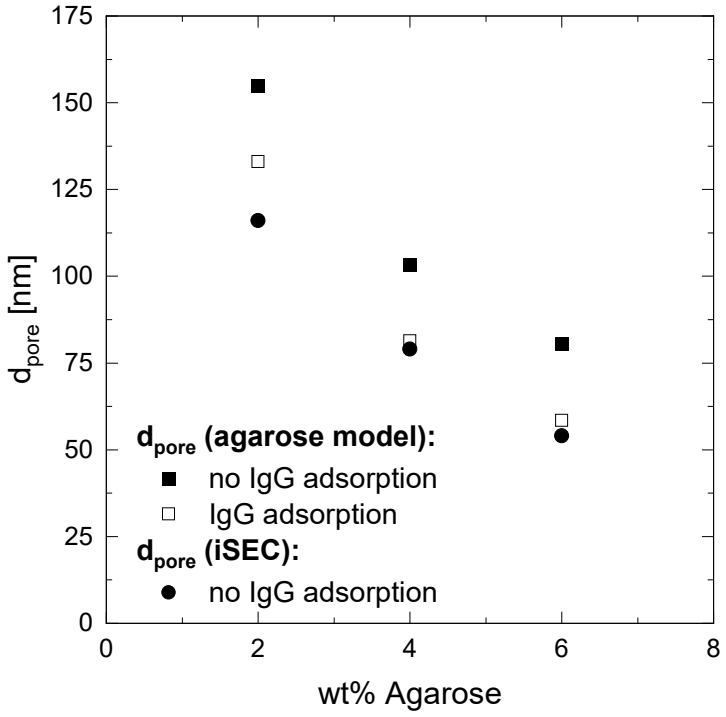

Figure 7.2.: Effect of agarose adsorption on the pore diameter. Data points calculated with the cubic grid model, cf. Section 6.1. Without IgG adsorption $d_{\text{fil}} = 16\,\text{nm}$ is assumed, with IgG adsorption $d_{\text{fil,apparent}} = 38\,\text{nm}$.

7.2. Diffusive mass transport in agarose gel particles

Diffusive porosities and other parameters needed for the simulation of breakthrough curves with the general rate model are presented in this section. Pore

diffusion coefficients are determined by fitting simulated breakthrough curves to experimental ones.

7.2.1. Influence of the gel concentration on diffusive porosities

From the iSEC results, presented in Figure 7.3, it can be concluded, that the residence time of dextranes in the protein A coupled agarose beads is not affected by electrostatic interactions, because no influence of the salt concentration is observed. This means, that dextran is a suitable tracer to determine residence times in agarose stationary phases.

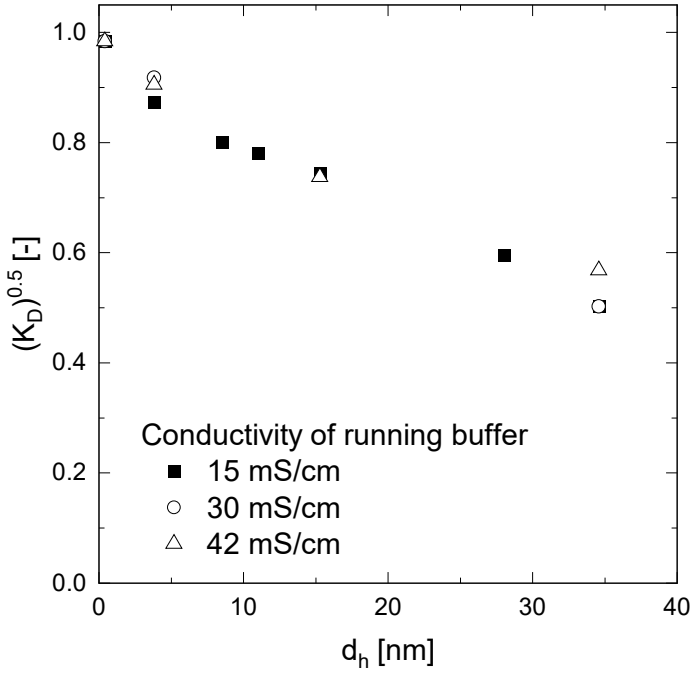

Figure 7.3.: Square root of the distribution coefficient over the hydrodynamic diameter of dextrans. Influence of salt concentration of the running buffer on retention volumes in an ABT154 column. Experimental data obtained by iSEC measurements, cf. Section 5.4.

The total porosity, ε_{dex}, for dextran and the maximum pore diameter, d_p, are determined by fitting Equation 5.3 to the experimental data which are shown in Figures 7.4 and 7.5. The porosity for IgG, ε_{IgG}, is then calculated with Equation 5.3. The results are presented in Table 7.1.

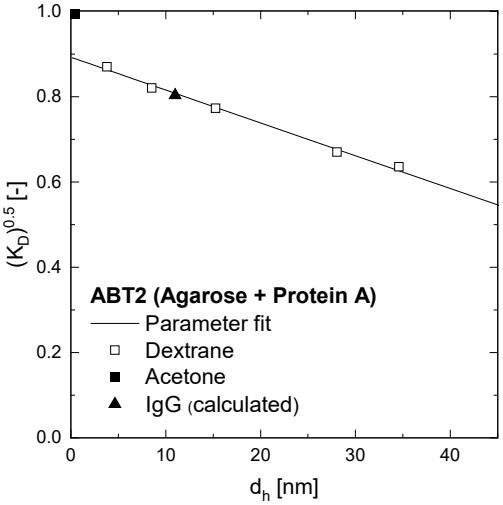

(a) Column packed with 2 wt% agarose beads $d_{\text{pore}} = 116\,\text{nm}$

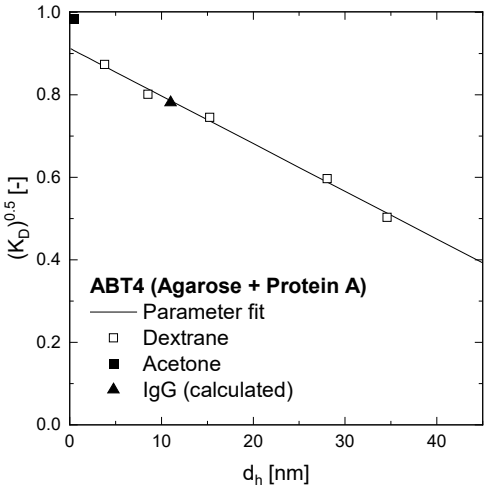

(b) Column packed with 4 wt% agarose beads $d_{\text{pore}} = 79\,\text{nm}$

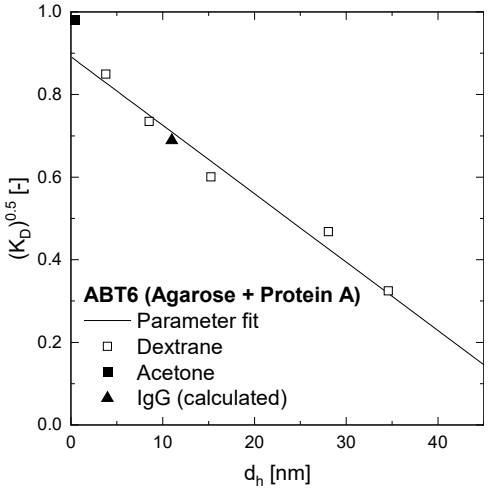

(c) Column packed with 6 wt% agarose beads $d_{\text{pore}} = 54\,\text{nm}$

Figure 7.4.: Inverse size exclusion experiments, cf. Section 5.4, with agarose concentrations of 2 wt%, 4 wt%, and 6 wt% at a residence time $\tau \approx 6\,\text{min}$. Square root of the distribution coefficient over the hydrodynamic diameter of dextrans. Parameter fits are calculated with Equation 5.3.

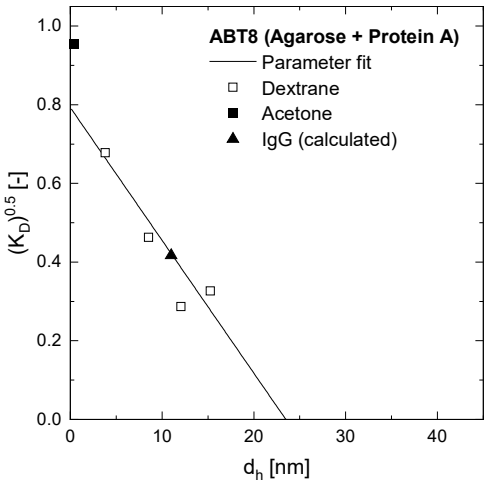

(a) Column packed with 8 wt% agarose beads $d_{\text{pore}} = 23\,\text{nm}$

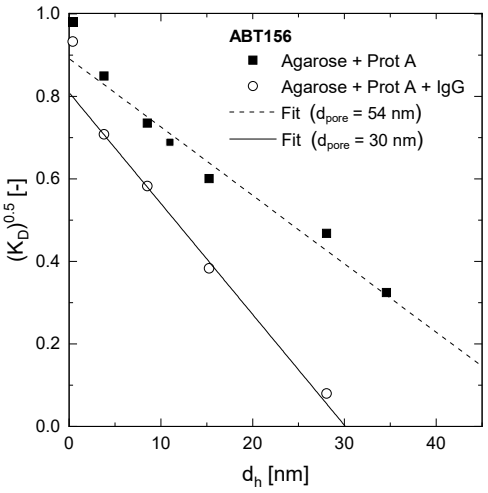

(b) Comparison of empty and loaded column using 6 wt% agarose beads

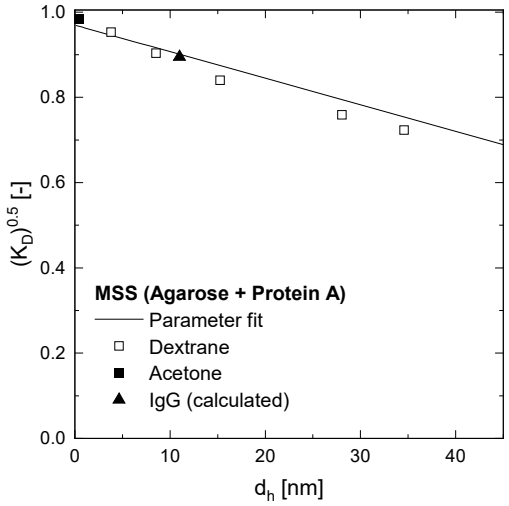

(c) Column packed with MSS beads $d_{\text{pore}} = 155\,\text{nm}$

Figure 7.5.: Inverse size exclusion experiments, cf. Section 5.4, with an agarose concentration of 8 wt%, a comparison of empty and loaded 6 wt% agarose beads and MSS beads at a residence time $\tau \approx 6\,\text{min}$. Square root of the distribution coefficient over the hydrodynamic diameter of dextrans. Parameter fits are calculated with Equation 5.3.

Table 7.1.: Porosities, particle and pore diameters of investigated bead materials and stationary phase volumes. Values calculated from results shown in Figures 7.4 and 7.5 with Equation 5.3.

Material	ε_t	ε_{IgG}	$\varepsilon_{acetone}$	ε_{dex}	d_{pore} [nm]
MSS	0.99	0.75	0.97	0.94	155
ABT2	0.99	0.63	0.99	0.80	116
ABT4	0.97	0.58	0.97	0.83	79
ABT6	0.96	0.47	0.96	0.79	54
ABT8	0.91	0.17	0.91	0.62	23

The data clearly shows a decreasing accessibility for acetone, IgG and dextranes with increasing agarose concentration and pore size reduction. As the filament diameter is independent of the agarose concentration [Djab1989], more filaments per volume are present when the agarose concentration is increased. This leads to smaller pore sizes, reduced accessibility and increased hindrance of diffusive mass transfer in the pores. However, the specific surface, available for binding enhances. Hence, there is a trade-off between binding capacity, accessibility and mass transfer velocity. For $8\,\mathrm{wt}\%$ agarose beads, the accessibility and the pore size are very low. For this specific material it is therefore assumed, that IgG does not enter into the pores any more.
ISEC experiments with a loaded column showed, that the accessibility decreases due to the adsorbed IgG, cf. Figure 7.5b. The pore diameter, deduced by fitting the data points, is reduced by $24\,\mathrm{nm}$ which is approximately two times the hydrodynamic diameter of the IgG, which is $\approx 11\,\mathrm{nm}$, cf. Section 5.1.

7.2.2. Parameter determination for the general rate model

In Table 7.2 chromatographic bed parameters are summarized. The bead diameter was determined according to Section 5.2.2 and the convective porosity according to Section 5.5.
Table 7.3 shows the calculated parameters D_{ax} and k_f, as well as the Langmuir coefficient K, which was adapted based on the study of Pabst et al. [Pabs2018]. The axial dispersion coefficient is calculated with Equation 3.34 and the film diffusion coefficient with Equation 3.28.

Table 7.2.: Model parameters for the general rate model. The particle diameter is obtained from microscopy measurements, cf. Section 5.2.2 and the convective porosity is determined according to Section 5.5. V is the volume of the chromatographic bed.

Material	V	d_p	ε_c
MSS	1.21	65.9 ± 16	0.37
ABT2	1.34	93.6 ± 16	0.25
ABT4	1.22	84.3 ± 12	0.31
ABT6	1.19	101.1 ± 17	0.32
ABT8	1.19	91.7 ± 17	0.21

Table 7.3.: Model parameters for the general rate model. The axial dispersion is calculated with Equation 3.34 and the film diffusion coefficient with Equation 3.28. The adsorption coefficient K is taken from [Pabs2018].

Material	D_{ax} $[m^2/s]$	k_f $[m/s]$	K $[m^3/mol]$
MSS	$6.07 \cdot 10^{-6}$	$2.45 \cdot 10^{-6}$	26640
ABT2	$5.99 \cdot 10^{-6}$	$1.96 \cdot 10^{-6}$	25574
ABT4	$3.41 \cdot 10^{-5}$	$2.06 \cdot 10^{-6}$	25574
ABT6	$1.74 \cdot 10^{-5}$	$1.88 \cdot 10^{-6}$	25574

The axial dispersion coefficient D_{ax} decreases with increasing bead diameter due to increasing interstitial space between the particles and decreasing bed volume. The film diffusion coefficient k_f is more influenced by the particle diameter than by the column porosity. As the particle diameter increases, the film diffusion coefficient decreases.

7.2.3. Hydrodynamics in the system

The acetone and IgG peaks, performed on the Äkta Prime system, are presented in Figure 7.6. The parameters of the CSTR-DPFR model are obtained by fitting the model to the experimental data. The results are listed in Table 7.4.

Table 7.4.: Results of the parameter fitting for the Äkta Prime and the Äkta Avant 25 system

	Parameter		Acetone (Prime)	IgG (Prime)	IgG (Avant)
CSTR	V	[m^3]	$0.95 \cdot 10^{-7}$	$2.60 \cdot 10^{-7}$	$3.45 \cdot 10^{-7}$
DPFR	D_{ax}	[m^2/s]	$3.50 \cdot 10^{-4}$	$4.11 \cdot 10^{-6}$	$2.7 \cdot 10^{-4}$
	L_{tube}	[m]	1.80	1.01	2.4

Different parameter values are obtained in order to describe the acetone and the IgG peak. One reason for the different peak shapes is the diffusivity of the target molecule. Small molecules with a high diffusivity, like acetone, show a Gaussian concentration profile due to high influence of molar diffusion. As the hydrodynamic diameter increases, like IgG, the diffusivity of the molecule decreases and the peak shape changes in the direction of a pure convection RTD, cf. Figure 3.12.

The shoulder in the experimental data of Figure 7.6b can be explained by the concentration profile which occurs due to the flow profile. The slow diffusivity of IgG is not able to compensate the concentration gradient in radial direction in the short tube. With increasing tube length, the shoulder disappears as diffusion has more time to smooth the radial concentration distribution but dispersion effects gain significance and the peak broadens [Bara2019]. This effect is shown in Figure 7.6c.

A simple model consisting of a DPFR and a CSTR, not taking into account radial effects, cannot describe the shoulder as precisely as the model of Baran et al. [Bara2019]. However, the simple model is able to describe the peak. An

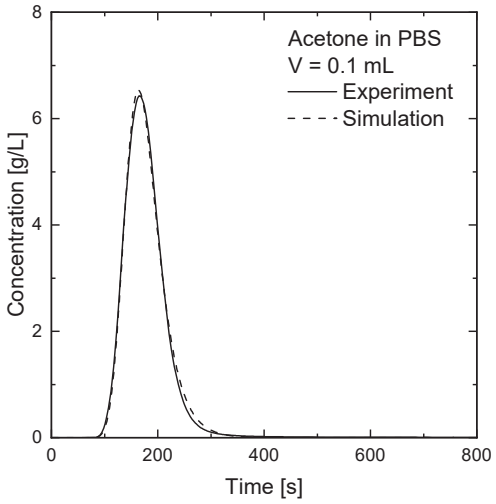

(a) Peak of $2\,\mathrm{v}\%$ acetone in PBS buffer, measured on an Äkta prime system.

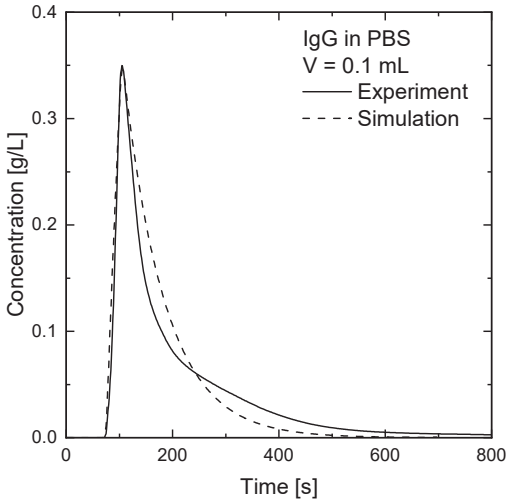

(b) Peak of $1\mathrm{g/L}$ IgG in PBS, measured on an Äkta prime system.

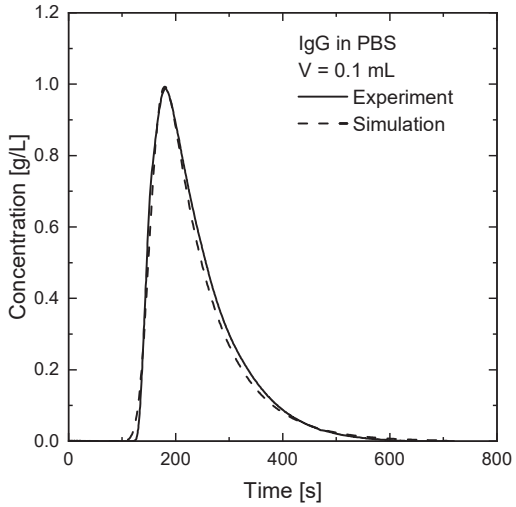

(c) Peak of $2\mathrm{g/L}$ IgG in PBS, measured on an Äkta Avant 25 system.

Figure 7.6.: Fitted tracer peaks of acetone (a), IgG (b) for the Äkta Prime system and IgG for the Äkta Avant 25 System (c) at $\dot{V} = 0.2\,\mathrm{ml/min}$. No device connected. For the simulation with CADET, a CSTR and a DPFR used, cf. Section 6.4.

improvement of the fit is possible by the introduction of a further parameter, which is unfavorable regarding the cost-benefit ratio. As $\mathrm{Re} \approx 10 < 2300$ the flow regime in the system tubes is assumed to be laminar.

7.2.4. Results from breakthrough curves

Figure 7.7 shows breakthrough curves of chromatographic beds consisting of 2 wt% to 8 wt% agarose beads. The different agarose concentrations are compared to the commercial MSS bead from GE.

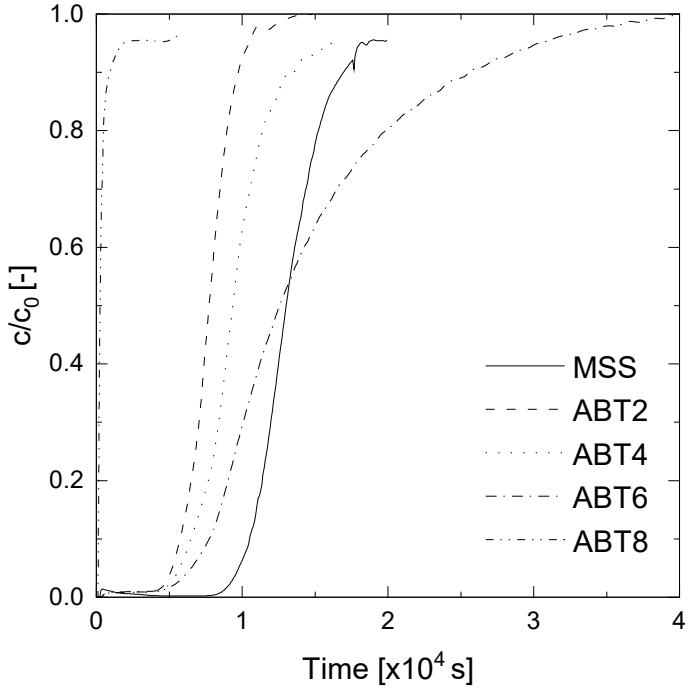

Figure 7.7.: Comparison of breakthrough curves for different agarose concentrations. Flow rate $\dot{V} = 0.2\,\mathrm{mL/min}$ and bed volume $V \approx 1\,\mathrm{mL}$.

The static binding capacity increases from 2 wt% to 6 wt% agarose, as the diffusive pore diameter decreases and the specific surface increases. The static binding capacity for 8 wt% is drastically reduced, due to the decreased pore accessibility. As the accessibility is too low and adsorption is assumed to only take place at the bead surface, 8 wt% agarose beads are not further considered in this work. The slope of the breakthrough curves decreases from 2 wt% to 6 wt% agarose, as the diffusive mass transfer is slowed down with decreasing diffusive pore diameter.

The pore diffusion coefficient for IgG is determined for 2 wt% to 6 wt% agarose by fitting the simulated breakthrough curve to the experimental data, cf. Section 5.7.3. The particle porosity for IgG used in the GRM is the porosity obtained for an agarose bead coupled with protein A, although bound IgG might block some binding sites, leading to a more conservative model. Experimental and simulated breakthrough curves are presented in Figure 7.8.

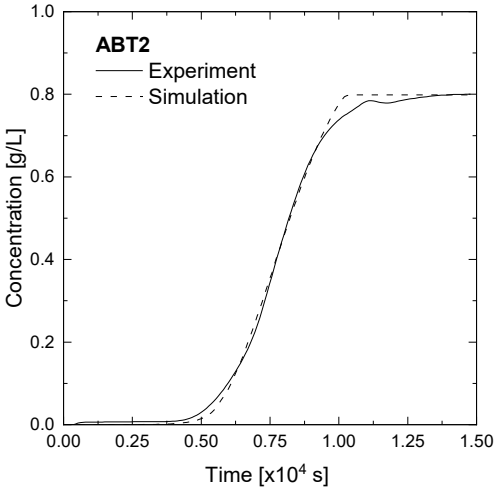

(a) Column packed with 2 wt% agarose beads $d_{\text{pore}} = 116\,\text{nm}$

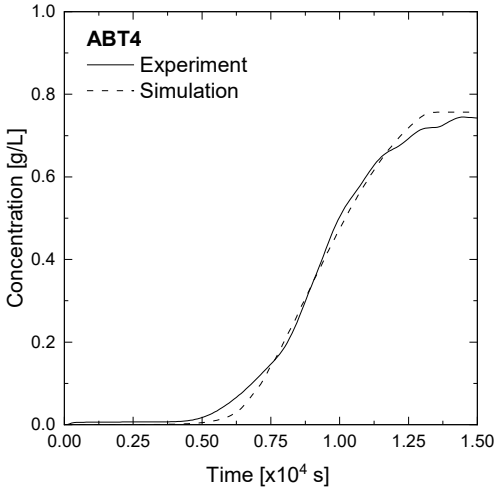

(b) Column packed with 4 wt% agarose beads $d_{\text{pore}} = 79\,\text{nm}$

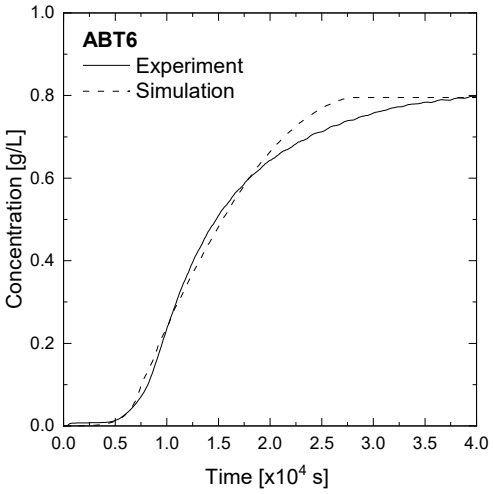

(c) Column packed with 6 wt% agarose beads $d_{\text{pore}} = 54\,\text{nm}$

Figure 7.8.: Experimental and simulated breakthrough curves of IgG on protein A beads at $\tau \approx 6\,\text{min}$ using an Äkta Prime. The breakthrough curve is simulated with the model presented in Figure 4.3, without the housing, using CADET.

In the ideal Langmuir model, the target molecules adsorb unhindered onto the surface. During the adsorption on real adsorber surfaces, hindrance effects occur, especially close to complete saturation. This is the reason why simulated breakthrough curve reach the final asymptotic concentration faster than the experimental curve.
The determined pore diffusion coefficients and the $\mathrm{DBC}_{100\,\%}$ values related to the ligand density are summarized in Table 7.5. Moreover, the process related $\mathrm{DBC}_{1\,\%}$ values related to the ligand density are shown. Binding capacities are related to the ligand density, because during the surface modification different amounts of binding sites are coupled to the beads.

Table 7.5.: Determined D_p and adjusted $\mathrm{DBC}_{100\,\%}$ by fitting the general rate model (Equations 3.39 and 3.40) to experimental data and $\mathrm{DBC}_{100\,\%}$ values

Material	D_p $[\mathrm{m}^2/\mathrm{s}]$	$\mathrm{DBC}_{100\,\%}/\rho_\mathrm{ligand}$ $[\mathrm{mg_{IgG}}/\mathrm{mg_{ProtA}}]$	$\mathrm{DBC}_{1\%}/\rho_\mathrm{ligand}$ $[\mathrm{mg_{IgG}}/\mathrm{mg_{ProtA}}]$
ABT2	$6.50 \cdot 10^{-12}$	2.61	1.91
ABT4	$5.72 \cdot 10^{-12}$	4.39	2.68
ABT6	$3.96 \cdot 10^{-12}$	3.47	1.12

With increasing agarose concentration, the diffusion coefficient decreases, which means that the mass transfer into the pores is more and more hindered. This agrees with the determined pore diameter in Table 7.2. The binding capacities related to the ligand density both have their maximum at $4\,\mathrm{wt}\%$ agarose.
It can be concluded from the results, that the pore structure of a $4\,\mathrm{wt}\%$ agarose suits best for the separation of IgG with protein A. Next to the trade off optimum, diffusion is still fast enough to result in high dynamic binding capacities. For lower agarose concentrations, the diffusive velocity increases but the binding capacity is not sufficient. At higher agarose concentrations, the specific surface increases, but the diffusive pore diameter decreases and with it the accessibility. Moreover, diffusion becomes more and more hindered.

7.2.5. Correlation between pore diffusion coefficients

The diffusion coefficients obtained from the parameter fit in Section 7.2.4 as well as diffusion coefficients provided in literature [Pabs2018] are shown in Figure 7.9b. The error bars represent the maximum inaccuracy of the target value, which is

calculated with the uncertainties of the input parameters. All input parameters were chosen so that they have maximum influence on the target value. In order to fit the experimentally obtained diffusion coefficients, the Ogston model, cf. Equation 3.23, and the Boyer model [Boye1992], cf. Equation 3.25, are modified. The empirical parameter C was added to the Ogston model:

$$\frac{D_\mathrm{p}}{D_0} = \exp\left[-C \cdot \frac{(r_\mathrm{s} + r_\mathrm{f})}{r_\mathrm{f}} \cdot \sqrt{\varphi}\right] \tag{7.1}$$

and found to be $C = 3.7379$ using the method of least squares. The filament volume fraction φ has to be determined with the cubic grid model for the diffusive pore structure. The variables A and B of the Boyer model [Boye1992] are changed to 0.0747 and 9.9733, respectively. Both models are valid for apparent filament diameters smaller than 0.51. This corresponds to an agarose concentration of $8\,\mathrm{wt}\%$ which is cross-linked, modified with protein A and IgG is bound.
Both models give the same result. The Boyer model is suitable for molecules for which it is difficult to determine a diameter.

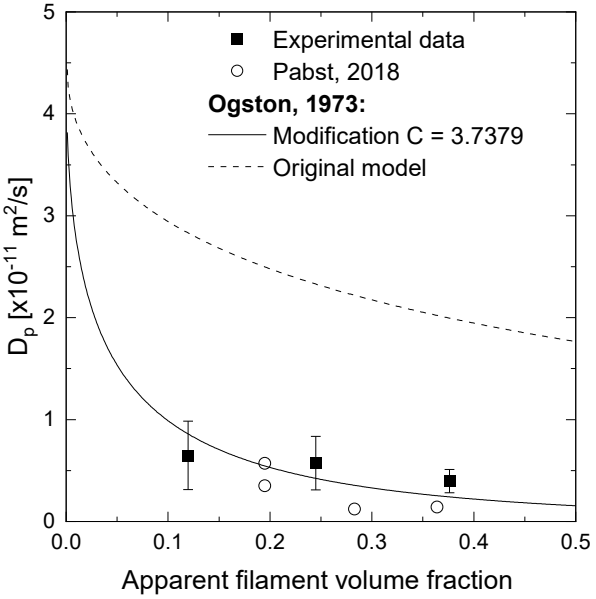

(a) Experimental data fitted with the Ogston model, Equations 3.23 and 7.1.

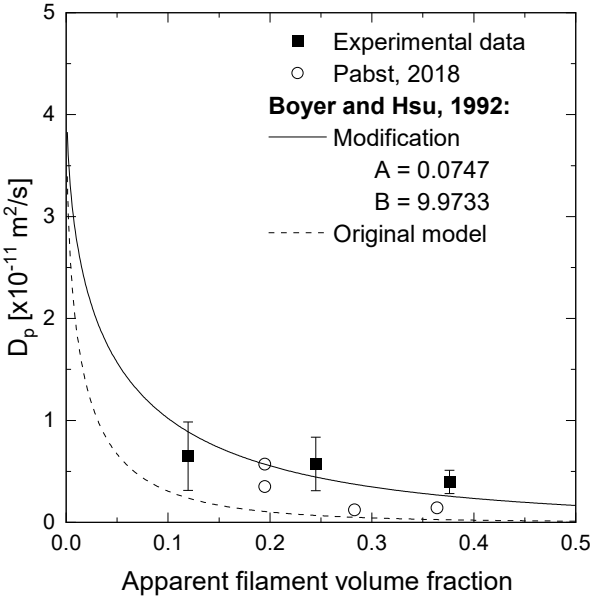

(b) Experimental data fitted with the Boyer model, Equation 3.25.

Figure 7.9.: Dependence of the diffusion coefficient on the apparent polymer volume fraction

7.3. Influence of particle size on material performance

As with increasing particle diameter, the diffusion inside pores becomes more and more hindered, accessibility, diffusion coefficients, binding capacities and resulting $DBC_{10\,\%}$ values are discussed in this section. For all target molecule sizes, affinity binding which leads to a reduction of the diffusive pore diameter, is assumed.

The accessibility (particle porosity) for different target molecule sizes was determined with the results from iSEC experiments, presented in Figures 7.4 and 7.5 and Equation 5.3. The accessible volume fractions for the different target molecules are shown in Figure 7.10. The pore size increases with decreasing agarose concentration. This results in a higher accessibility for low agarose concentrations for all target molecule sizes. Particle porosities for $1\,\mathrm{wt\%}$ agarose were calculated with Equation 5.2 using extrapolated values for ε_{dex} and d_{pore}.

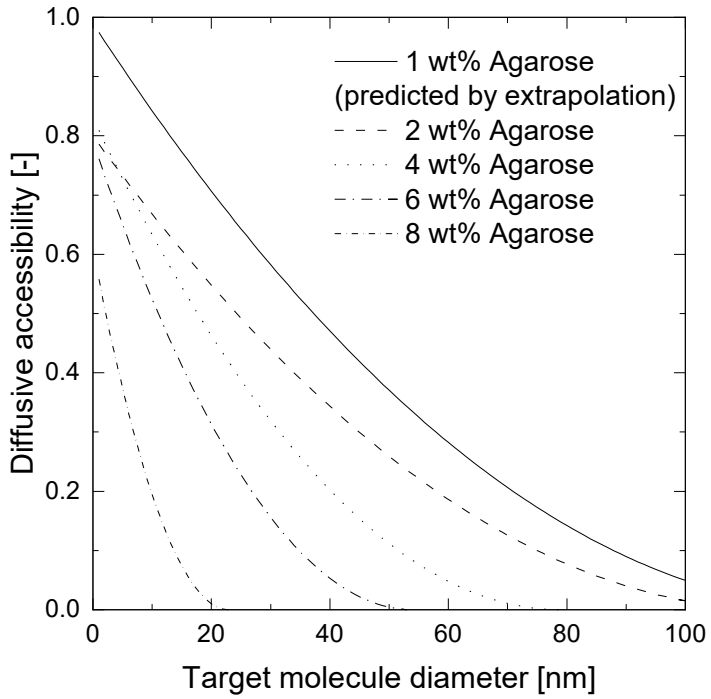

Figure 7.10.: Accessible volume fractions for different target molecule diameters, calculated with Equation 5.3 and the results from iSEC experiments. The accessibility for $1\,\mathrm{wt\%}$ agarose was calculated from linear extrapolated values for the dextran porosity and the diffusive pore diameter.

The diffusion coefficients for different agarose concentrations and target molecule diameters are estimated with the Ogston model, cf. Equation 7.1, and the agarose model from Section 6.2. The results are presented in Figure 7.11. As the diffusive pore diameter becomes smaller, the hindrance of diffusion increases and the diffusion coefficient diminishes. With increasing particle diameter the effective diffusion coefficient decreases due to increased hindrance. In order to ensure a diffusive mass transfer which is fast enough, the agarose concentration should be at maximum $2\,\mathrm{wt\%}$ for the separation of target molecules larger than $d_\mathrm{h} = 20\,\mathrm{nm}$. For target molecules smaller than $d_\mathrm{h} = 20\,\mathrm{nm}$ agarose concentrations up to $6\,\mathrm{wt\%}$ are possible.

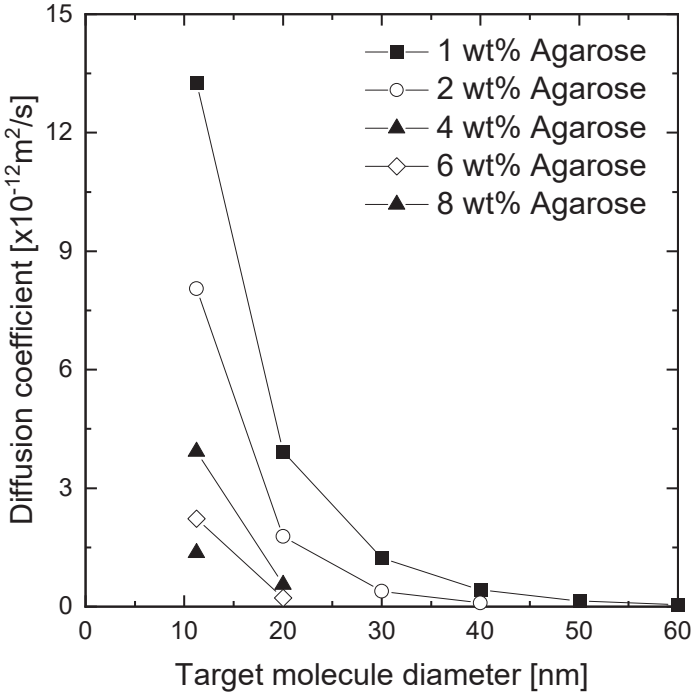

Figure 7.11.: Diffusion coefficients of different target molecule sizes in agarose networks, calculated with the modified Ogston model, cf. Equation 7.1, and the cubic grid model, cf. Section 6.1.

The static binding capacities of the different agarose and target molecule combinations were estimated from the accessible specific surface, cf. Equation 6.6. The specific adsorptive surface densities that are used for the calculations of the static binding capacity, are shown in Figure 7.12.

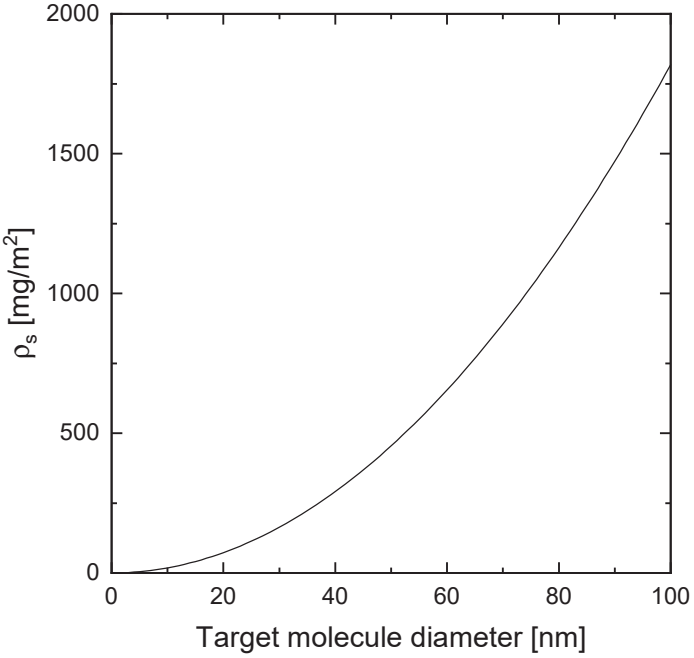

Figure 7.12.: Surface densities for different target molecule sizes estimated from the surface density of PrismA.

They are estimated from the specific adsorptive density value of PrismA material, cf. Section 6.1. As already stated, the pore diameter increases with decreasing agarose concentration, leading to a better diffusive mass transfer. On the other hand the specific surface decreases, resulting in lower binding capacities. The estimated static binding capacities for different target molecule sizes are presented in Figure 7.13. For each target molecule an optimum agarose concentration leads to the highest static binding capacities.

Accessibilities, diffusion coefficients and static binding capacities have been calculated for different target molecule sizes. In the following, $\mathrm{DBC}_{10\,\%}$ values are determined from simulated breakthrough curves. Due to the trade-off between diffusive mass transfer and binding capacity, the $\mathrm{DBC}_{10\,\%}$ was simulated for particles of $45\,\mu\mathrm{m}$ radius and a volumetric flow rate of $0.25\,\mathrm{MV/min}$. Moreover, the influence of the resin radius and the flow rate on the dynamic binding capacity were investigated. The optimum agarose concentration for different target molecule sizes at a given diffusive length is given in Figure 7.14. The optimum agarose concentrations for different particle sizes are presented in Figure 7.15. Calculations were performed at discreet values. The course between the calculated points is

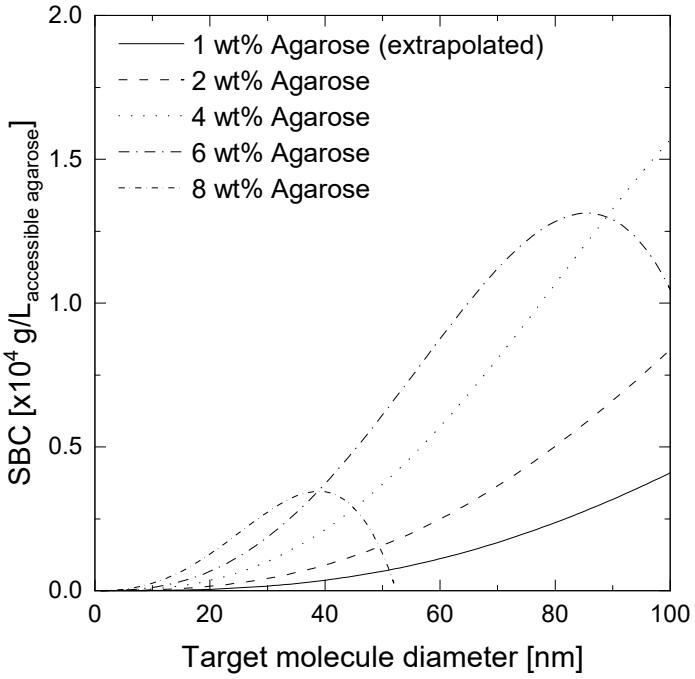

Figure 7.13.: Static binding capacities, calculated from the specific surface of the agarose and the surface density ρ_s.

indicated by lines. For 30 nm particles the accessibility at 4 wt% agarose is zero. The dashed line shows how the $DBC_{10\,\%}$ runs.

Due to the trade-off between diffusive pore diameter and specific surface, each target molecule size has an optimum agarose concentration for maximum dynamic binding capacity. This optimum shifts to smaller agarose concentrations with increasing target molecule diameter. With decreasing resin diameter, a slower diffusion is possible. Therefore, smaller pores and higher agarose concentrations are possible. An increase of the flow rate leads to lower maximum dynamic binding capacities due to mass transport limitations. This shifts the optimum to lower agarose concentrations. For conventional beads ($d_p = 45\,\mu$m, $\dot{V} = 0.25\,$MV/min) and the target molecule IgG the optimum agarose concentration is 4 wt%. With decreasing diffusive pathway smaller diffusive pores are possible and the optimum agarose concentration increases to 6 wt%. A further increase of the agarose concentration leads to such small pores, that IgG has no accessibility anymore. For a target molecule diameter of 20 nm the optimum agarose concentration is 2 wt% in conventional bead processes. A decrease of the diffusive pathway at

constant flow rate increases the $DBC_{10\,\%}$ drastically and shifts its optimum to 6 wt%. An increase of the flow rate reduces the $DBC_{10\,\%}$ and the optimum agarose concentration is at 4 wt%.

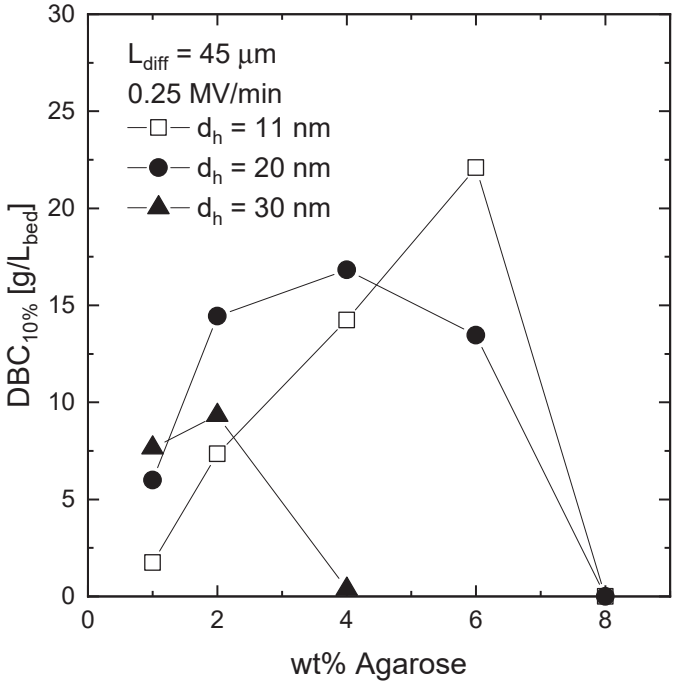

Figure 7.14.: $DBC_{10\,\%}$ values for different molecule sizes depending on the agarose concentration.

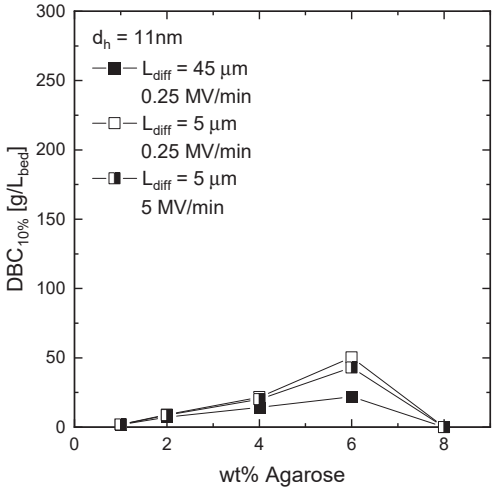

(a) Impact of the particle radius and the flow rate on $DBC_{10\,\%}$ for 11 nm

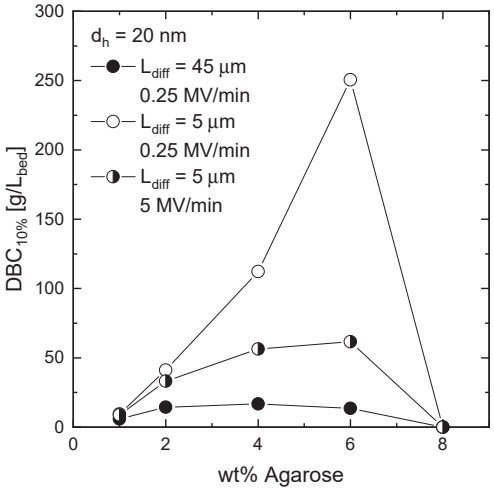

(b) Impact of the particle radius and the flow rate on $DBC_{10\,\%}$ for 20 nm

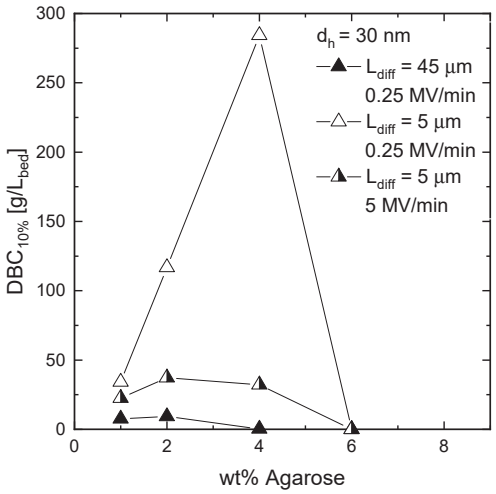

(c) Impact of the particle radius and the flow rate on $DBC_{10\,\%}$ for 30 nm

Figure 7.15.: $DBC_{10\,\%}$ values for different agarose concentrations, diffusive length L_{diff} and flow rates. Optimum agarose concentration for different stationary phase configurations (particle diameter and agarose concentration) and flow rates can be read. Discrete values are obtained from breakthrough curve simulations using the general rate model.

7.4. Conclusion

The optimum stationary phase for a target molecule should have a highly accessible specific surface for binding and fast diffusive mass transport in the pores. Due to the increasing surface and the decreasing accessibility and diffusive mass transport with decreasing pore diameters, there is a trade-off between these parameters. The following statements can be concluded from this chapter:

- As the agarose concentration increases in the investigated range from $2\,\mathrm{wt\%}$ to $6\,\mathrm{wt\%}$, the pore diameter decreases from $116\,\mathrm{nm}$ to $54\,\mathrm{nm}$, leading to an increased specific surface. As the pore diameters become smaller with increasing agarose concentration and IgG is adsorbed, the diffusive mass transfer of IgG, which lies in the range between $3.96 \cdot 10^{-12}\,\mathrm{m^2/s}$ and $6.5 \cdot 10^{-12}\,\mathrm{m^2/s}$, decreases.
- Due to IgG adsorption, the diameter of each pore reduces by twice the time of the IgG's hydrodynamic diameter, which leads to a lower diffusivity in agarose networks.
- Both, the Ogston model and the Boyer model [Boye1992] were modified and could be fitted to the determined diffusion coefficients of IgG in the different porous networks.
- The optimum agarose concentration is highly dependent on the target molecule size, the diffusive pathway and the applied flow rate.

8. Hydrodynamics in the device

Parts of this chapter have been published as:

Franziska Hagemann, Denis Wypysek, Kristina Baitalow, Patrick Adametz, Volkmar Thom, Matthias Wessling
Why device design is crucial for membrane adsorbers
Journal of chromatography open, 2021
DOI: 10.1016/j.jcoa.2021.100029

In this chapter, the hydrodynamics in selected Sartorius devices is investigated. First, the experimental residence time distribution (RTD) of several devices is compared to each other. In a second step, RTD are determined with CFD simulations in order to investigate the impact of bed height, convective porosity, permeability and the dead volume in the device. It was possible to separate the impact of the housing and the membrane on the RTD of the device, using CFD simulations.

8.1. RTD of different devices

In Figure 8.1, the RTD of different devices, consisting of housing and membrane, are compared. The RTD of the corresponding device is determined by deconvolution, according to the procedure presented in Section 5.8, in order to eliminate the impact of the system. The parameters needed are listed in Table A.7 in the appendix.

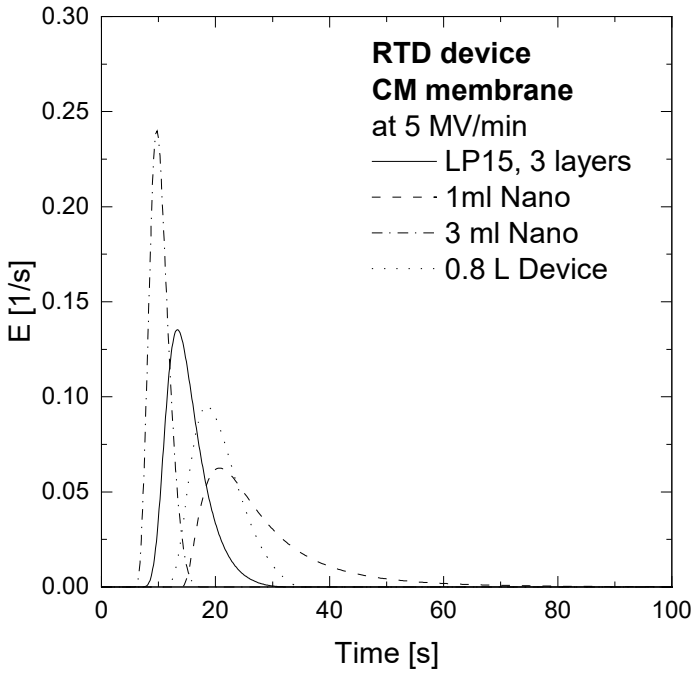

Figure 8.1.: Residence time distribution of various Sartorius devices at $5\,\mathrm{MV/min}$ using CM membrane, eliminating the impact of the surrounding system. The acetone tracer volume is $100\,\mu\mathrm{L}$ for all devices, except the $0.8\,\mathrm{L}$ device, where a step signal was used. The input peak length is $2.4\,\mathrm{s}$. For the calculation of these graphs the method presented in Sections 5.7.1 and 5.8 is used.

The 3 ml Nano device shows the sharpest peak and the lowest residence time. This results from a specific design to minimize the dead volume of the device. The mean residence time of the LP15 laboratory device is also shorter than the one of the 1 mL Nano and the 0.8 L device. This is due to the fact, that the LP15 laboratory device has less dead volume than the other ones. However, the peak width is ≈ 20 s, which suggests that the distribution can still be improved. The peak of the 1 mL device is symmetric, whereas the peak of the 0.8 L device shows strong tailing. In 1 mL Nano devices, the same housing as in 3 mL Nanos is used. The difference between both designs is the membrane bed height: In the 1 mL Nano the bed height is 4 mm and the remaining volume is filled with fleece. This leads to a higher dead volume and a higher residence time.

In this study, the LP15 laboratory device with 3 membrane layers is used as a reference. This device is used for the membrane adsorber development in laboratory scale.

8.2. Impacts on flow distribution of LP15 devices

In Figure 8.2 experimentally obtained RTD, using LP15 devices, are compared to CFD simulations at two bed heights.
The results show that the simulated RTD is sharper for both bed heights. Reasons for this are different bed heights, the squeezing of the membrane during device integration and the purely fluid mechanical CFD model. During device integration, the membrane is compressed at the edges, leading to a deviation from the cylindrical shape which is used in the simulations. In the simulation, membrane bridges consist of non porous material and convective flow appears in the porous network only. The real agarose membrane has porous bridges. They can be entered by acetone, leading to a higher mean residence time and broader distributions in the experiment compared to the simulations. In the model, the diffusion into the membrane bridges is not taken into account, which results in an optimistic prediction of the RTD. However, the CFD model is able to describe the RTD characteristics and is used in the following to point out the impact of bed height, dead volume, porosity and permeability on the RTD.

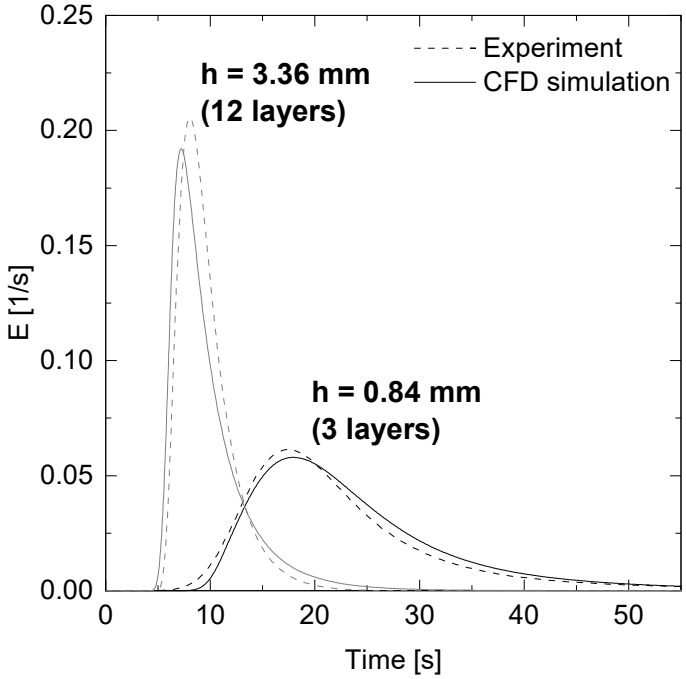

Figure 8.2.: Comparison of experimental and simulated RTD of the LP15 device for bed heights of 1 mm and 4 mm. Tracer experiments were performed according to Section 5.7.1 and CFD simulations according to Section 6.4.2.

8.2.1. Impact of bed height, porosity and permeability

The impact of the bed height is shown in Figure 8.3. With increasing bed height, the residence time distribution becomes sharper, as dispersion due to entrance and exit effects for flat sheet devices can be minimized by the stacking of membranes. Due to an increase in pressure loss over the membrane bed, the fluid distribution becomes more even. Increasing the bed height from 8 mm to 12 mm only brings little improvement, which is in agreement with literature [Liu1994].

Porosity and permeability have no noteworthy impact on simulated residence time distributions, cf. Figure A.11 in the appendix. One reason for that is, that the impact of the housing superimposes the one of the membrane.

For an adequate distribution, the bed height of the membrane should be 8 mm. Higher beds would lead to smaller RTD, but would also lead to an increase in pressure drop, cf. Section 10.1.2. For the optimum membrane adsorber the permeability among other has to be adapted to meet pressure drop limitations and an optimum binding capacity. Another important design criteria is the accessibility of the binding sites for the target molecule and a high dynamic binding capacity.

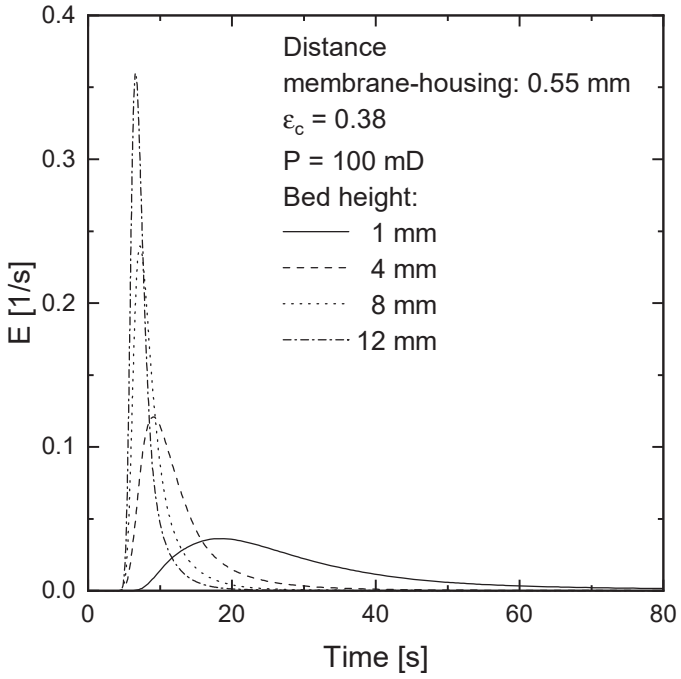

Figure 8.3.: Comparison of simulated RTD of the LP15 device for bed heights from 1 mm to 12 mm. CFD simulations were performed according to Section 6.4.2.

8.2.2. Impact of dead volume

The impact of the dead volume in the device on the residence time distribution of acetone tracer peaks is shown in Figure 8.4. The configurations with dead volume have a gap up to 0.55 mm above and below the membrane. A schematic representation of the configurations is given in Figure 8.5.

The RTD also becomes sharper, when the dead volume of the device decreases, as it enables backmixing which leads to a broadened RTD at the device's outlet. Obviously, the dead volume has to be kept as small as possible to ensure a sharp RTD.

The design of the LP15 device has to be adapted to the bed heights. This ensures a constant dead volume to membrane ratio and comparable results. A device without dead volume is preferable.

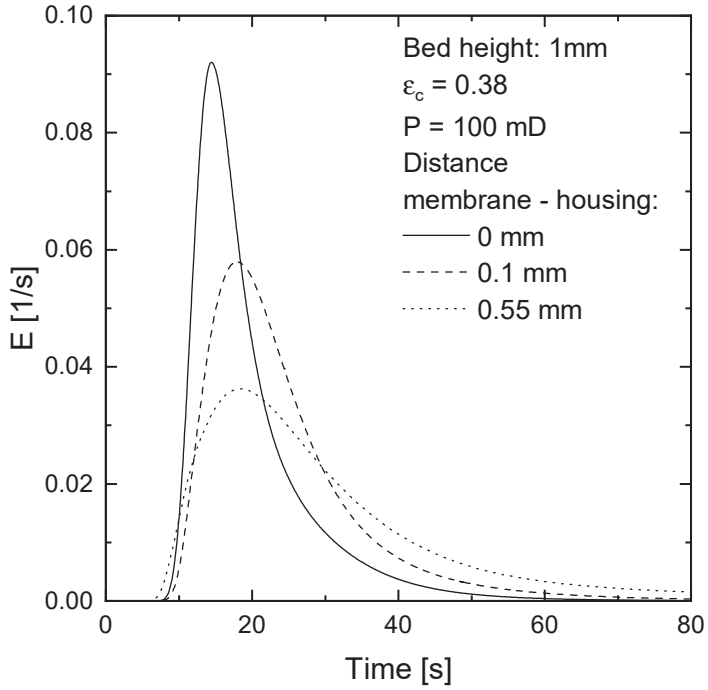

Figure 8.4.: Comparison of device integration with and without dead volume into an LP15 laboratory device at $5\,\mathrm{MV/min}$. Data taken from COMSOL simulations, cf. Section 6.4.2.

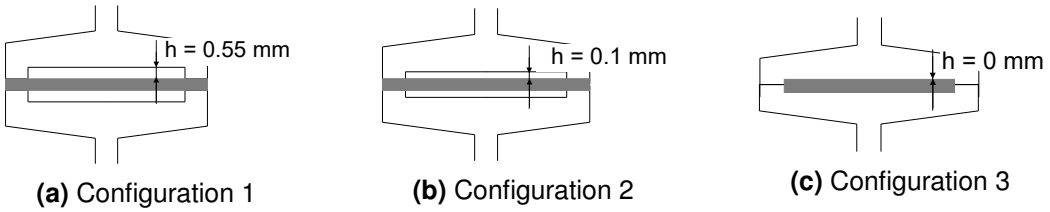

(a) Configuration 1 **(b)** Configuration 2 **(c)** Configuration 3

Figure 8.5.: Comparison of device integration with and without dead volume into an LP15 laboratory device at $5\,\mathrm{MV/min}$. Data taken from COMSOL simulations, cf. Section 6.4.2.

8.2.3. Impact of bed height on breakthrough curves

In order to demonstrate the influence of the device hydrodynamics on the process, breakthrough curves with $1\,\mathrm{g/L}$ IgG for different bed heights in the LP15 laboratory device were measured with membrane material AM1. In contrast to the results presented above, the impact of system is not excluded from the breakthrough curves. The results are shown in Figure 8.6.

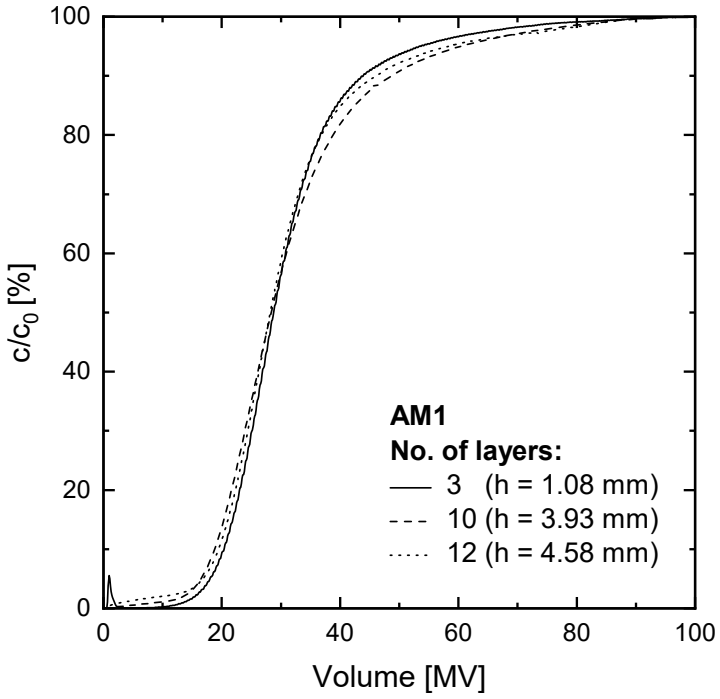

Figure 8.6.: Experimental breakthrough curves with $1\,\mathrm{g/L}$ IgG solution at $5\,\mathrm{MV/min}$ using different bed heights in an LP15 laboratory device

The expected increase of the slope due to a sharper RTD at higher membrane beds cannot be observed. It is assumed that band spreading due to fluid distribution is superimposed by a diffusive mass transfer limitation in the membrane bridges that results from the membrane structure. Further research has to be done in order to prevent those mass transfer limitations.

8.3. Separating the influence of housing and membrane

The device consists of the housing and the membrane. The housing is an essential component, as it fixes the membrane and distributes the fluid. To further analyze the RTD, the influence of housing and membrane on tracer signals is simulated with CFD using the method described in Sections 6.4.2. The simulated tracer responses of the total LP15 laboratory device and the of a $3\,\mathrm{mL}$ Nano are presented in Figure 8.7 and 8.8, respectively.

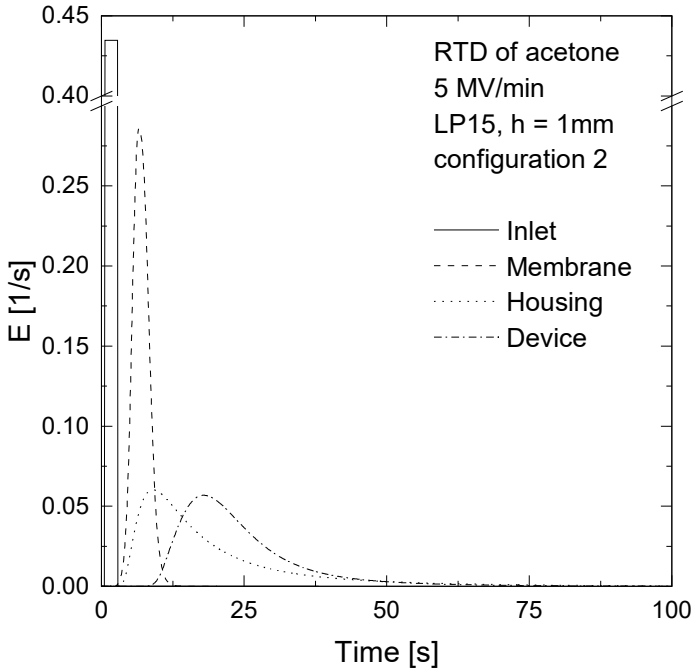

Figure 8.7.: Comparison of the RTD of the membrane, the housing and the total device for a LP15 laboratory device. Bed height: $1\,\mathrm{mm}$, flow rate: $5\,\mathrm{MV/min}$, configuration 2, cf. Figure 8.5. RTD of the housing for different flow rates with equivalent circuit and the development of its parameters over the flow rates. For the procedure, cf. Section 6.4.2.

The results show the impact of membrane and housing on the RTD, resulting from mathematical decoupling of device and membrane. In Figure 8.7 the results for the LP15 device are shown. The RTD of the membrane is sharp and symmetric, whereas the one of the housing is broad and shows tailing. It becomes clear, that the influence of the housing dominates the RTD of the total device. This explains the small influence of porosity and permeability on the RTD, demonstrated in

Figure A.11.

Figure 8.8 shows the result of the 3 mL Nano. Despite the lower flow rate, the RTD is sharper than the one of the LP15. This is due to the optimized dead volume in the 3 mL Nano device. The RTD of the housing has an extensive tailing but apart from this, its influence on the total device RTD is small. The membrane broadens the device signal and leads to unavoidable additional residence time, as the tracer has to flow through the membrane.

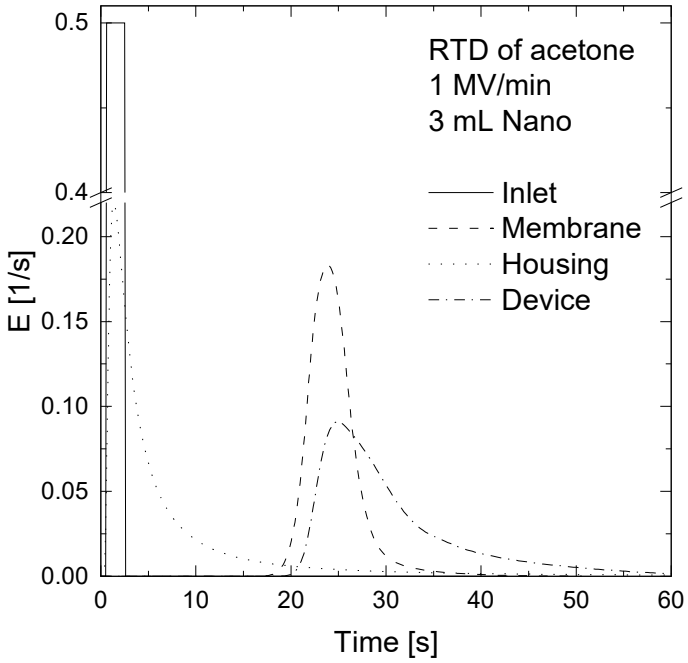

Figure 8.8.: Comparison of the RTD of the membrane, the housing and the total device for a 3 mL Nano device. Bed heigth: 8 mm, flow rate: 1 MV/min. RTD of the housing for different flow rates with equivalent circuit and the development of its parameters over the flow rates. For the procedure, cf. Section 6.4.2.

8

An equivalent circuit diagram was developed, cf. Section 6.4.2, and the impact of the flow rate on the size of the CSTR and the DPFR was investigated. Results for a 1 mm membrane bed height in configuration 2 are shown in Figure 8.9a and the parameter of the unit operations are summarized in Table A.2 in the appendix. In Table A.3 the results for a 3 mL Nano at a flow rate of 1 MV/min are shown.

Figure 8.9a shows exemplary fits of the equivalent circuit to the calculated RTD of the housing for volumetric flow rates of 1 MV/min and 5 MV/min. The fits for the

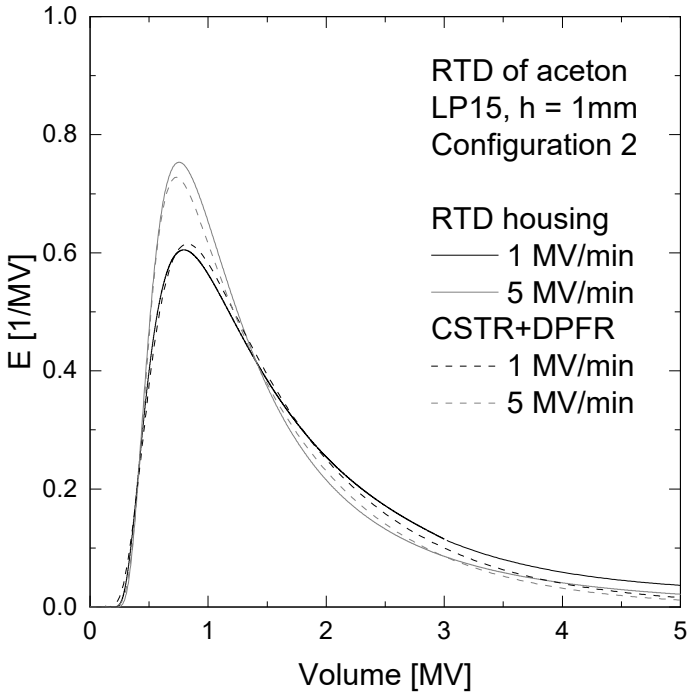

(a) Equivalent circuit of the housing's RTD using a CSTR and a DPFR.

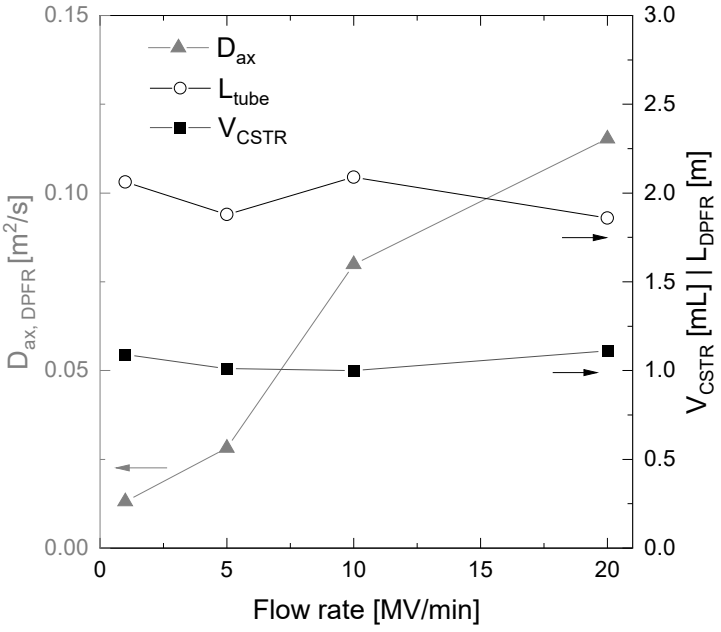

(b) Parameters for the equivalent circuit

Figure 8.9.: RTD of the housing for different flow rates with equivalent circuit and the development of its parameters over the flow rates. For the procedure, cf. Section 6.4.2.

other flow rates have a similar accuracy. Due to a higher pressure loss over the membrane, which results in a better flow distribution, the RTD becomes sharper, when the flow rate increases. The application of the parameters in Figure 8.9b shows nearly constant values for the volume of the CSTR and the length of the DPFR. The axial dispersion coefficient increases with the flow rate. This is in accordance with the correlation shown in Equation 3.34.

8.4. Conclusion

In this chapter the hydrodynamics in membrane adsorber devices were investigated. As the fluid distribution influences the quality of the breakthrough curve, it is important to gain understanding and to build models. The following conclusions can be drawn from this chapter:

- Experiments and CFD simulations showed, that the dead volume in the devices has to be as small as possible in order to obtain sharp RTD.
- It was shown by experiments and CFD simulations that an increasing membrane bed height up to $8\,\mathrm{mm}$ leads to a sharpening of the RTD. Bed heights larger than $8\,\mathrm{mm}$ no longer lead to a significant improvement of the RTD.
- Porosity and permeability do not have a significant influence on the simulated RTD in the considered range.
- Using CFD simulations, the impact of the housing and the membrane on the RTD of the device could be separated. In a LP15 device, the influence of the housing dominates the RTD of the total device. When the dead volume is optimized, as in a $3\,\mathrm{mL}$ Nano, the impact of the housing on the RTD of the total device is less distinct.

9. Simulation of membrane breakthrough curves considering system and housing

Breakthrough curves of membrane adsorbers are simulated and compared to experimental data, which was measured on the Äkta prime system. Two devices with two different flow rates were chosen:

- LP15 laboratory device, $h_{\text{bed}} \approx 0.9\,\text{mm}$, 3 layers, $1\,\text{MV}/\text{min}$
- LP15 laboratory device, $h_{\text{bed}} \approx 0.9\,\text{mm}$, 3 layers, $5\,\text{MV}/\text{min}$
- 3 mL Nano device, $h_{\text{bed}} \approx 8\,\text{mm}$, $1\,\text{MV}/\text{min}$

The model for the membrane adsorber process is build up as presented in Figure 4.3. This chapter also presents the determination of parameters that are needed for the simulation of membrane adsorbers.

9.1. Model parameters for system and housing

The parameters for the Äkta system are determined for each flow rate of the three devices, cf. Section 5.7.1. The results are plotted in Figure A.12 in the appendix and the parameters for the CSTR and the DPFR are summarized in Table A.4 in the appendix. With increasing flow rate, the tracer residence time reduces. It is important, that this effect is considered in the simulation of breakthrough curves, when the system is taken into account. The simulation of the tracer peaks over the system is in good agreement with the experimental data. The model parameters for the describtion of the housing are given in Tables A.2 and A.3.

9.2. Parameters for the general rate model

The diffusive porosity of the membrane bridges and the diffusive pore diameter are determined by iSEC measurements. The results are plotted in Figure 9.1. The diffusive porosity for IgG in the AM1 membrane adsorber material is 0.69 and the largest pore in the model has a diameter of $130\,\text{nm}$.
The bridge size distribution is shown in Figure 9.2. The mean bridge diameter is $3.07 \pm 1.36\,\mu\text{m}$. Parameters for the simulation of the membrane adsorber AM1 are summarized in Table A.5 in the appendix.

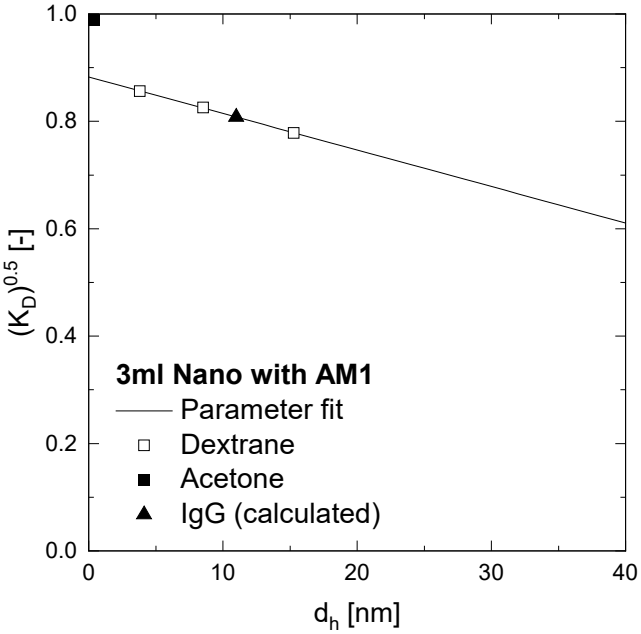

Figure 9.1.: Inverse size exclusion experiments, cf. Section 5.4, for the determination of the diffusive porosity of the membrane using a 3 mL Nano with AM1 membrane, $d_{\text{pore}} = 130\,\text{nm}$ at $\dot{V} = 0.2\,\text{mL/min}$. For the parameter fit Equation 5.3 is used.

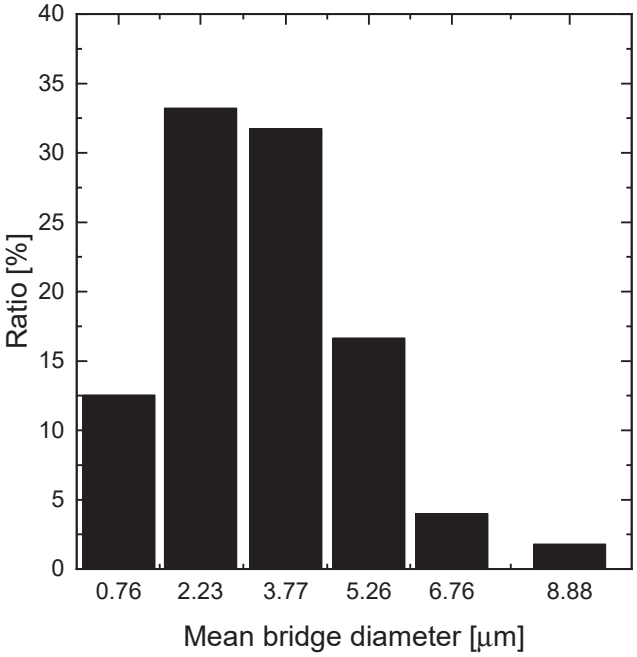

Figure 9.2.: Bridge size distribution for the membrane AM1, determined according to the procedure presented in Ley et al. [Ley2018].

9.3. Simulation of membrane adsorber breakthrough curves

Breakthrough curves are simulated by using the parameters determined in Sections 9.1 and 9.2. The experimental and simulated breakthrough curves of the three different configurations are shown in Figure 9.3. Experiments were performed with two devices in order to show the effects of membrane volume on the one hand and the device structure on the other. The used membranes (AM1) in all three devices were taken from the same lot.

The effective diffusion coefficient of $9 \cdot 10^{-13}\,\mathrm{m^2/s}$ was obtained by fitting the model up to $40\,\%$ of the total breakthrough, cf. Figure 4.3, to the experimental data which were obtained with the LP15 device at $1\,\mathrm{MV/min}$, cf. Figure 9.3a. The effective diffusion coefficient is low compared to literature values, cf. Pabst, Thai and Hunter [Pabs2018]. Further research has to be done to identify possible reasons, such as mass transfer limitation inside the agarose structure or flow through effects. The 1D model, which is used here, is not able to describe the impact of poorly flowed through membrane areas. This results in an effective diffusion coefficient, that also takes into account the flow distribution.
The fitted diffusion coefficient was taken to simulate the breakthrough curve of the LP15 device at a flow rate of $5\,\mathrm{MV/min}$. The experimental breakthrough curve is well described by the simulation. For the $3\,\mathrm{mL}$ prototype device, which is based on the $3\,\mathrm{mL}$ Nano, the simulated breakthrough curve deviates from the experimental one. The deviation might result from membrane inhomogeneity, device integration and the flow distribution. However, in the important region up to $10\,\%$ breakthrough the breakthrough curve is well described by the model for all three cases. Based on these results it is concluded that it is possible to describe a membrane process with the model presented in Figure 4.3.

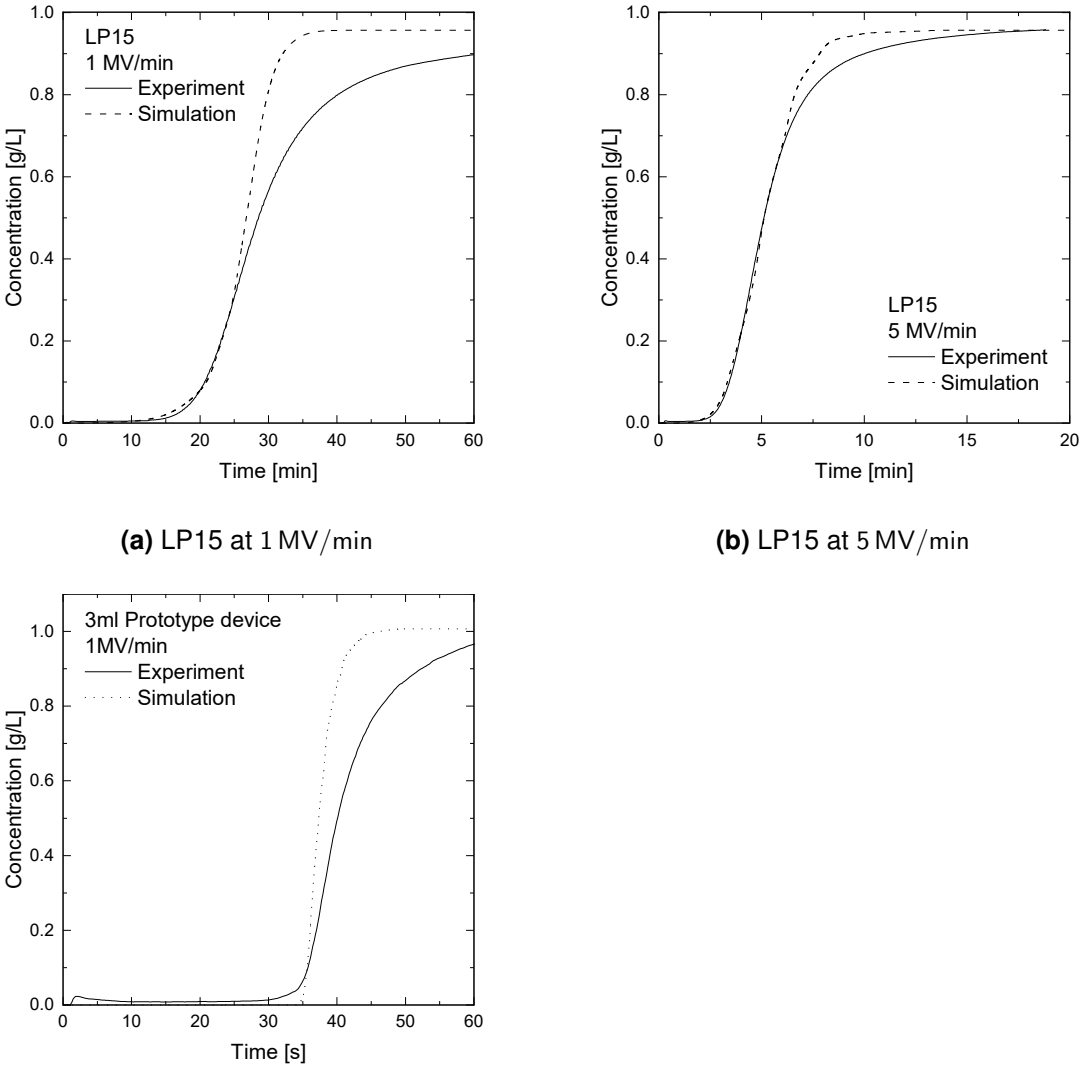

(a) LP15 at 1 MV/min

(b) LP15 at 5 MV/min

(c) 3 ml Nano at 5 MV/min

Figure 9.3.: Simulation of membrane adsorber breakthrough curves for three different cases with the general rate model. Used parameters are presented in Table A.5.

9.4. Conclusion

In this chapter membrane adsorber breakthrough curves were simulated with the model shown in Figure 4.3 and compared to experimental data. The parameters for the general rate model are determined experimentally or by calculations.

- The effective pore diffusion coefficient was determined to be $9 \cdot 10^{-13}\,\mathrm{m^2/s}$, which is relatively low compared to typical values from agarose resins. Reasons for the low diffusion coefficient might be due to the agarose structure or the fact, that the used 1D model is not capable to describe the influence of flow distribution on breakthrough curves. The impact of the distribution might therefore be lumped into the pore diffusion coefficient, which therefore has smaller values than expected.
- The breakthrough up to $10\,\%$ of the total breakthrough is well described by the simulated breakthrough curves.
- The model is further used to describe breakthrough curves of membrane adsorbers.

10. Membrane adsorber design

The convective mass transfer inside membrane adsorbers and the design of the stationary phase is considered in this chapter. For an optimal utilization of the membrane capacity, it is of great interest to find the maximum distance, that the target molecule can reach by diffusing into the material in a certain time. The size of the membrane bridge, in which the diffusive mass transfer takes place, is approached with models of different complexity. Pressure drop limits and the membrane stability are taken into account for the optimization of the convective porosity and the bridge size.

10.1. Geometry and structure of high capacitive membrane adsorbers

10.1.1. Design of the membrane bridge size

A first approach to estimate the size of the membrane bridge, is to calculate the accessible diffusive pathway (L_{diff}) with Equation 6.11. The relation between diffusive pathway, effective diffusion coefficient and effective residence time are presented in Figure 10.1 for slab and spherical geometry. Two geometries are considered, because the membrane shows a combination of various geometries, cf. Appendix A.2.1.

Both graphs show, that with increasing diffusion coefficient and with increasing residence time inside the convective pores a longer diffusive pathway is accessible. The accessible diffusive pathway is larger for spheres than for slabs due to the volume reduction in radial direction.

The maximum membrane bridge radii, that correspond to the diffusive pathway, are presented in Table 10.1 for an effective residence time of $3.6\,\text{s}$, which corresponds to a residence time of $12\,\text{s}$ for a membrane with a convective porosity of 0.3.

Table 10.1.: Diffusive length taken from the results in Figure 10.1. Diffusion coefficients are taken from Table 7.5.

wt% agarose in bridges	L_{diff}, slab [μm]	L_{diff}, sphere [μm]
2	1.89	1.13
4	1.69	1.05
6	1.48	0.88

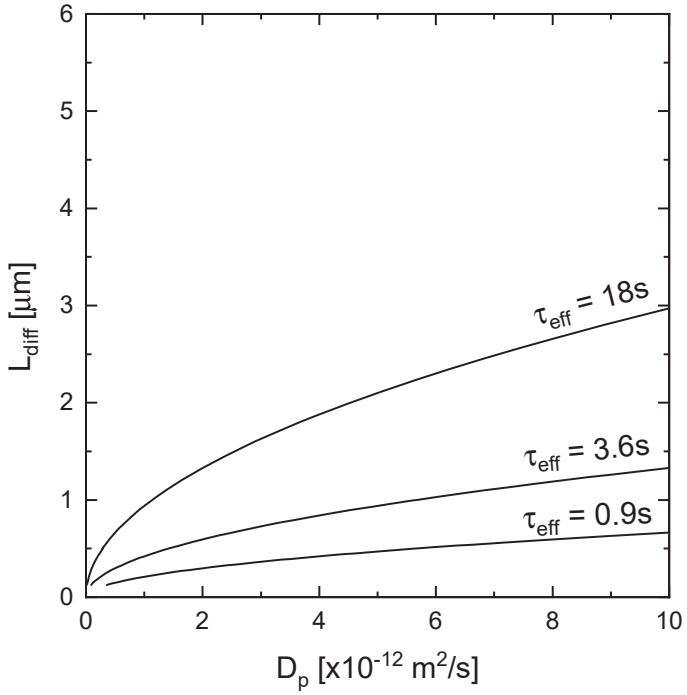

(a) Slab geometry

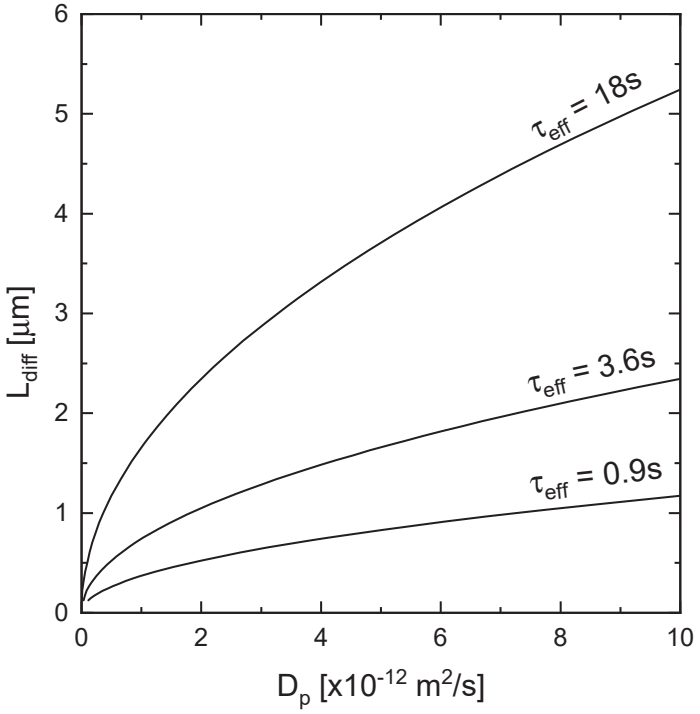

(b) Spherical geometry

Figure 10.1.: Diffusive pathway as function of the pore diffusion coefficient and the effective residence time. Calculated with Equation 6.11. Calculations were performed until 90 % of the binding sites are occupied.

In a more precise approach for the estimation of the membrane bridge size, the hydrodynamic in the membrane bed is taken into account. To this end, $DBC_{10\,\%}$ values are calculated, using the general rate mode at a residence time of $12\,s$. Geometry and porosity impacts are presented in Figure 10.2. The results for the influence of the agarose concentration and the flow rate are shown in Figure 10.3.

With an increasing diffusive pathway, the breakthrough curve flattens and breakthrough occurs earlier, because the diffusion is not fast enough to access the whole membrane bridge. Therefore, the $DBC_{10\,\%}$ decreases as the diffusive pathway becomes longer. Allowing $5\,\%$ loss of the $DBC_{10\,\%}$ in comparison to only device dispersion, diffusive pathways are in the range between $1\,\mu m$ (slab) and $4\,\mu m$ (sphere) for IgG in a $4\,wt\%$ agarose stationary phase, cf. Figure 10.2a.
Simulations showed, that the optimum diffusive pathway is dependent on the convective porosity. This effect is shown in Figure 10.2b. With decreasing convective porosity, the volume of accessible stationary phase increases which results in an increasing static and dynamic binding capacity.

In Figure 10.3a the dependence of the agarose concentration on the $DBC_{10\,\%}$ is presented. The changes in the accessibility and the diffusion coefficient for different agarose concentration are taken into account. For small membrane bridges up to a radius of $4\,\mu m$, $6\,wt\%$ agarose gives the highest $DBC_{10\,\%}$ value, because of the large surface which is available for binding. For larger bridges, the highest $DBC_{10\,\%}$ values are reached with $2\,wt\%$ agarose. Because of the large diffusive pathways, low agarose concentrations are needed to ensure the highest possible accessibility.
The impact of the flow rate on the $DBC_{10\,\%}$ is shown in Figure 10.3b. With increasing flow rate, the slope of the curve increases, leading to smaller diffusive pathways when the $DBC_{10\,\%}$ is kept constant. This is due to high residence time dependency of the diffusive mass transfer.
The first approach, that only takes into account the diffusive mass transfer inside the membrane bridges, is conservative and leads to smaller diffusive pathways as the second approach, which also takes into account the membrane bed hydrodynamics. The highest $DBC_{10\,\%}$ is reached with a concentration of $6\,wt\%$ agarose for diffusive pathways smaller than $4\,\mu m$.

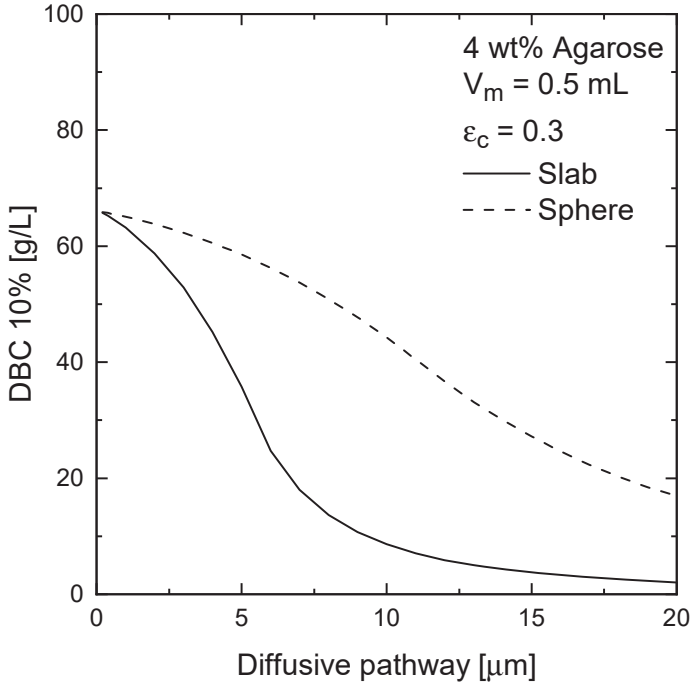

(a) Influence of the geometry at 5 MV/min

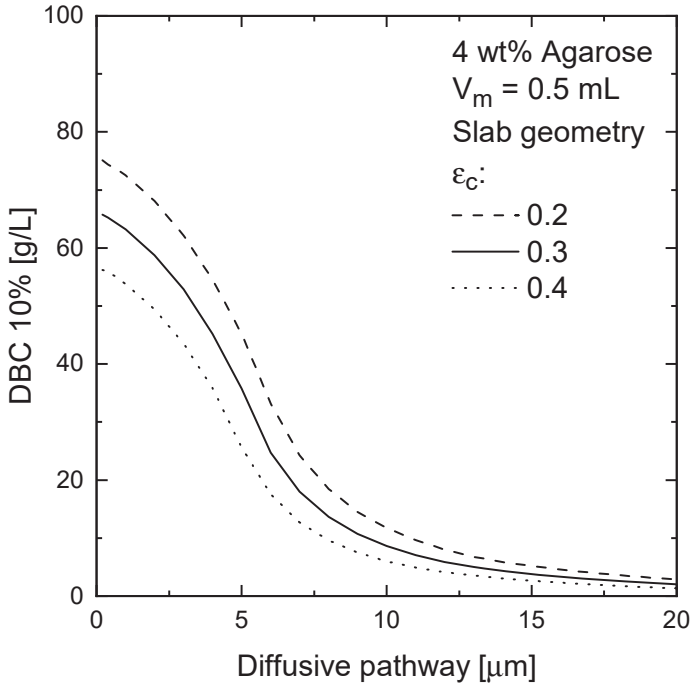

(b) Influence of ε_c at 5 MV/min

Figure 10.2.: $DBC_{10\,\%}$ of the membrane bed as a function of the diffusive pathway for the diffusion and adsorption of IgG in agarose stationary phases. The influence of the stationary phase geometry and the convective porosity is shown. Parameters of the general rate model are listed in Table A.6 in the appendix.

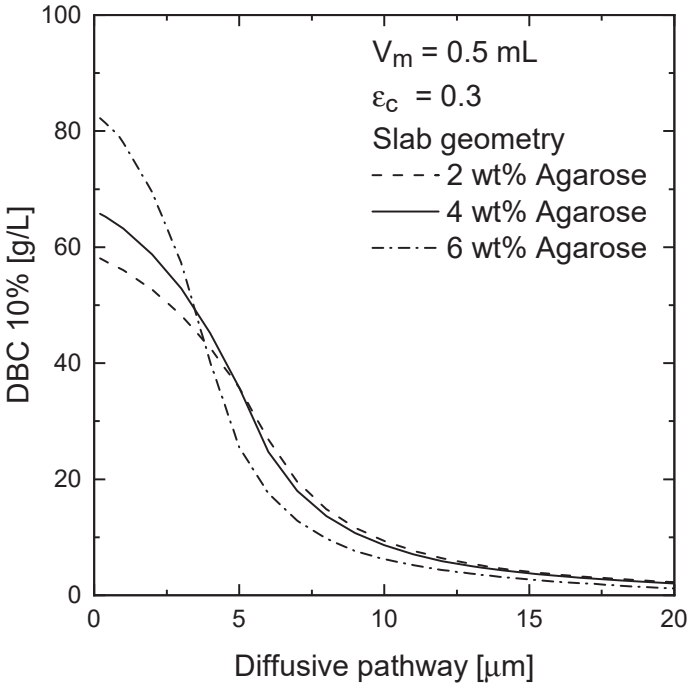

(a) Influence of the agarose concentration at $5\,\mathrm{MV/min}$

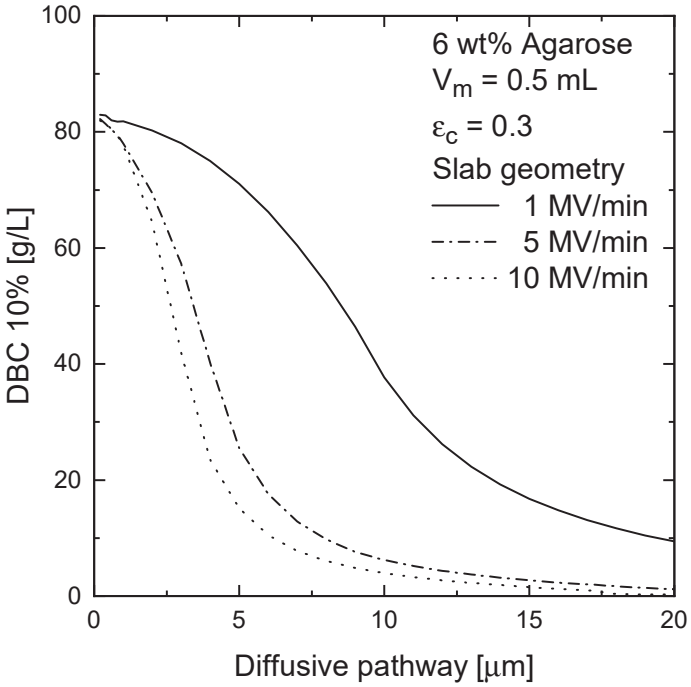

(b) Influence of the flow rate on $6\,\mathrm{wt\%}$ agarose

Figure 10.3.: $\mathrm{DBC}_{10\,\%}$ of the membrane bed as a function of the diffusive pathway for the diffusion and adsorption of IgG in agarose stationary phases. The impact of the agarose concentration and the flow rate is shown. Parameters of the general rate model are listed in Table A.6 in the appendix.

10.1.2. Pressure drop over the membrane

The relation between permeability and pressure drop is presented in Figure 10.4. With increasing permeability the pressure drop decreases due to a decreasing flow resistance.
With increasing bed height and viscosity the pressure drop over the membrane stack increases. The viscosity of IgG solutions of different concentrations in PBS buffer is shown in Figure A.13 in the appendix. In a concentration domain up to $5\,\mathrm{g/L}$, which is usually used in the loading step of the chromatographic step, the viscosity of the solution can be approached by water. Increasing the concentration to $20\,\mathrm{g/L}$, which is possible in elution steps, the viscosity and the pressure drop over the membrane bed increase.

A maximum pressure drop as a typical industry standard for chromatography steps, $2\,\mathrm{bar}$ are assumed. This leads to a minimum required permeability between $100 - 150\,\mathrm{mD}$. By an increase of the permeability to the upper limit, a more robust pressure drop range is reached, because the curve flattens in the domain of larger permeabilities. The pressure drop over the housing is not considered in these calculations but is added in the process.
In order to obtain the highest volume available for binding, the convective porosity should be as small as possible in the range of the allowed pressure drop of $2\,\mathrm{bar}$.

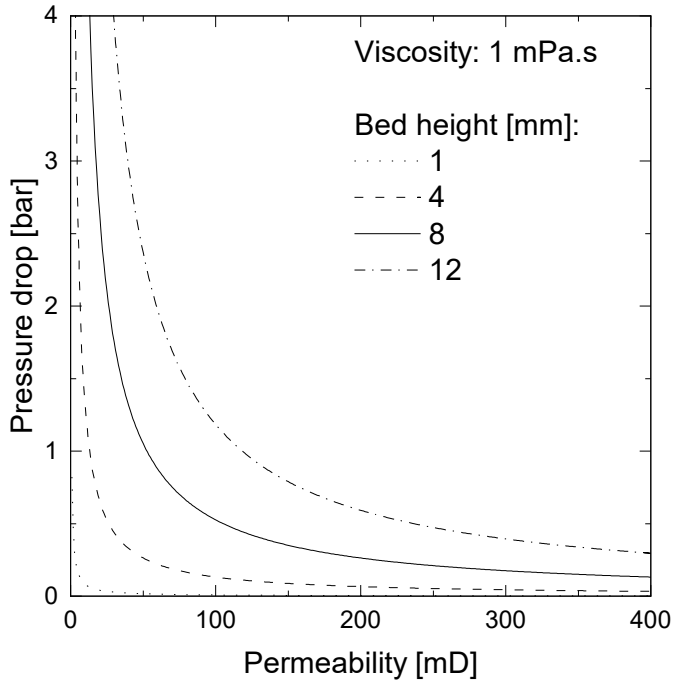

(a) Influence of the bed height

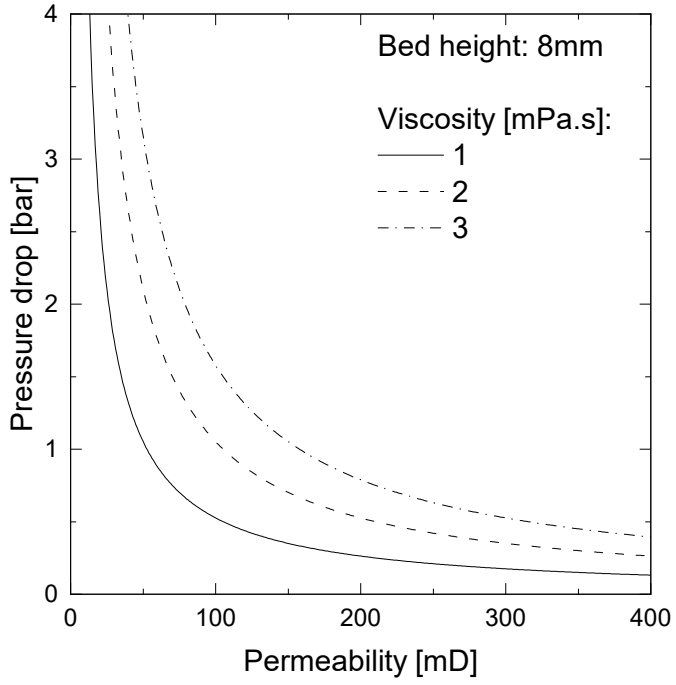

(b) Influence of the viscosity

Figure 10.4.: Permeability - pressure drop plots calculated with Equation 3.10. The flow rate is set to $5\,\mathrm{MV/min}$.

10.1.3. Membrane stability

The membrane could be exposed to compressive forces due to multilayer device integration and pressure gradients during operation. This can lead to a reduction of the permeability and the convective pore diameter.
With compression experiments, performed as described in Section 5.6, the stress induced height change of the membrane stack can be calculated. The height reductions of the bed for two different agarose membranes, AM1 and AM2, are shown in Figure 10.5. The main difference between the two membranes is the used support material. The experimental data was fitted with the Farazdaghi Harris approach, cf. Appendix A.4.7. Although two different reinforcement materials are used, the compression behavior of the two membranes is very similar. The impact

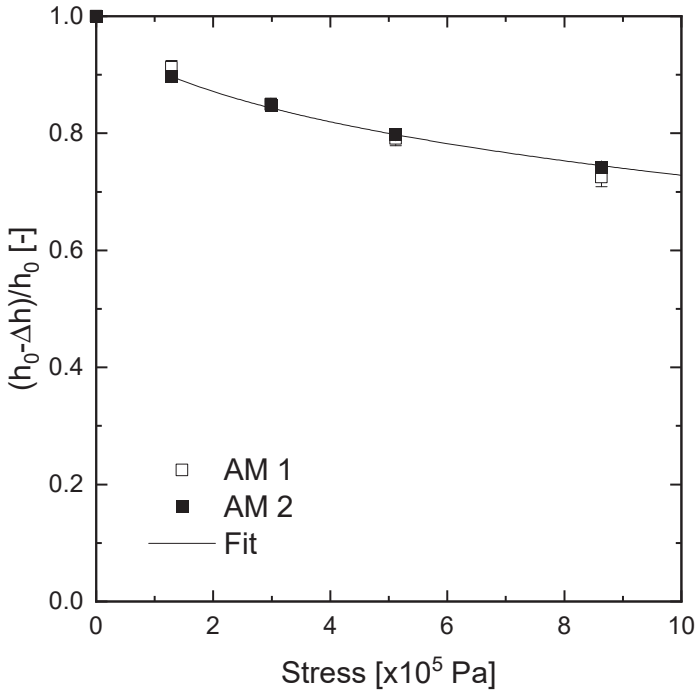

Figure 10.5.: Relative bed height reduction of AM1 and AM2, procedure cf. Section 5.6. The pressure is referred to the solid surface area. Data points are fitted with the Farazdaghi Harris correlation, parameters summarized in Appendix A.4.7 .

of compression on membrane characteristics, such as the permeability, the total pressure drop over the stack and the convective pore diameter were calculated. The results for the membrane configurations shown in Table 10.2, are plotted in Figure 10.6.

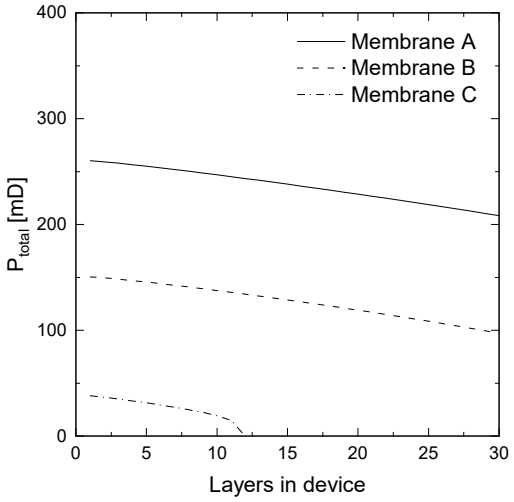

(a) Calculated permeability of the membrane stack

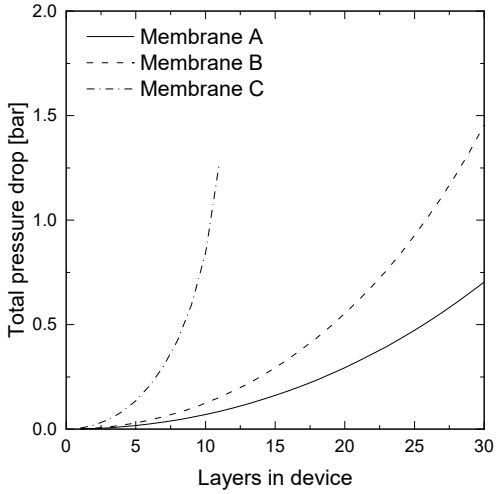

(b) Calculated total pressure drop of the membrane stack

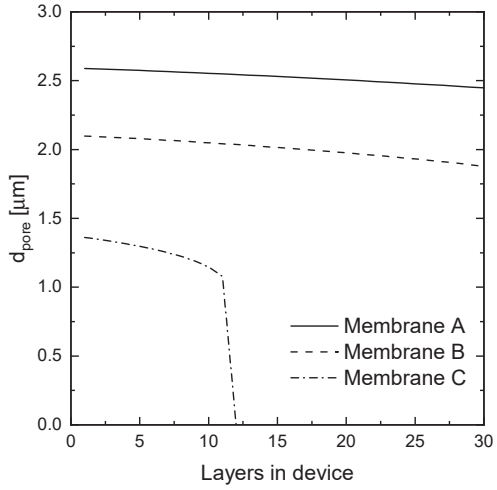

(c) Calculated convective pore diameter of the membrane stack

Figure 10.6.: Calculated membrane characteristics in dependence of the number of layers in a device, calculated with Equation 3.9, at $\dot{V} = 5\,\mathrm{MV/min}$ taking into account membrane deformation due to pressure , cf Figure 10.5. For membrane configuration cf. Table 10.2.

Table 10.2.: Possible porosity, bridge and pore size combinations of agarose membrane [Sart2020]

	ε_c	d_{bridge} [μm]	$d_{pore,0}$ [μm]
Membrane A	0.43	3	2.59
Membrane B	0.38	3	2.10
Membrane C	0.23	3	1.37

In Figure 10.6a the calculated impact of stress on the permeability of the membrane bed is shown. In general the permeability of the stack decreases the more layers are integrated. Due to the increasing bed height, the pressure drop increases and with it the stress, cf. Figure 10.6b. The membrane bed is compressed and the convective pore diameter is reduced, cf. Figure 10.6c. With decreasing convective porosity and pore diameter, the pressure drop over the membrane bed increases and the permeability decreases. For a convective porosity of 0.23, the membrane bed of 12 layers is compressed that much, that the pores are squeezed closed and the membrane becomes impermeable.
In order to meet the pressure drop target of $2\,\mathrm{bar}$, using a bed height of $\approx 8\,\mathrm{mm}$ which corresponds to 30 membrane layers, the raw membrane should have a porosity of $\varepsilon_c = 0.43$ and a mean convective pore diameter of $d_{\mathrm{pore},0} = 2.59\,\mu\mathrm{m}$. This leaves a safety margin of $30\,\%$ to the desired permeability of $150\,\mathrm{mD}$.

10.2. Optimization of the convective porosity

In order to find the trade-off between binding volume and diffusive mass transfer a convective porosity study was performed for different flow rates for membranes with the agarose parameters from Table 6.1. With increasing flow rate, the pressure drop over the membrane increases. In order not to exceed the limit of $2\,\mathrm{bar}$, the convective porosity is increased, which leads to better diffusive mass transfer, due to smaller diffusive pathways, but lower binding volume, due to less binding volume. Each flow rate therefore has an optimum convective porosity leading to the highest $\mathrm{DBC}_{10\,\%}$-value. In Figure 10.7 this effect is shown for a membrane with $6\,\mathrm{wt}\%$ agarose in the bridges. Graphs for other agarose concentrations are summarized in Figure A.14 in the appendix.
The convective porosities leading to the highest $\mathrm{DBC}_{10\,\%}$ for different volumetric flow rates and agarose concentrations in the stationary phase, are plotted in Figure 10.8a. The bridge diameter correlates to the convective porosity according to Equation 6.7. When the convective porosity increases, the bridge diameter decreases. This dependency on the flow rate is shown in Figure 10.8.

The bridge diameter leading to the maximum $\mathrm{DBC}_{10\,\%}$ decreases with increasing flow rate, due to shorter residence times. The bridge diameter increases with the pore diffusion coefficient. Due to the shorter diffusion times needed to reach

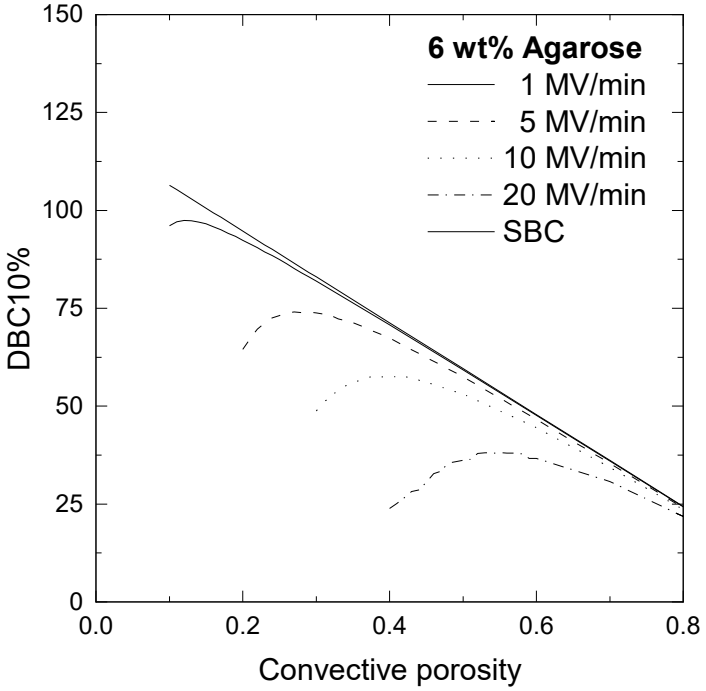

Figure 10.7.: Optimum $DBC_{10\,\%}$ for different convective porosities for a $6\,\mathrm{wt}\%$ agarose membrane material, taking into account a pressure limit at $2\,\mathrm{bar}$

the binding sites, larger bridge diameters are possible. The impact of the feed concentration on the optimum convective porosity and bridge diameter is negligible, cf. Figure A.15 in the appendix.

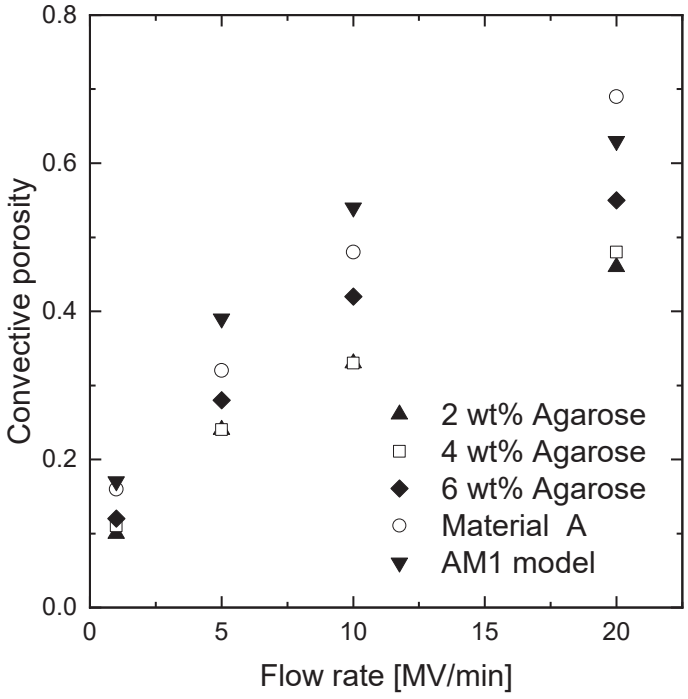

(a) Convective porosities that yield in the maximum $DBC_{10\,\%}$-values for $1\,g/L$

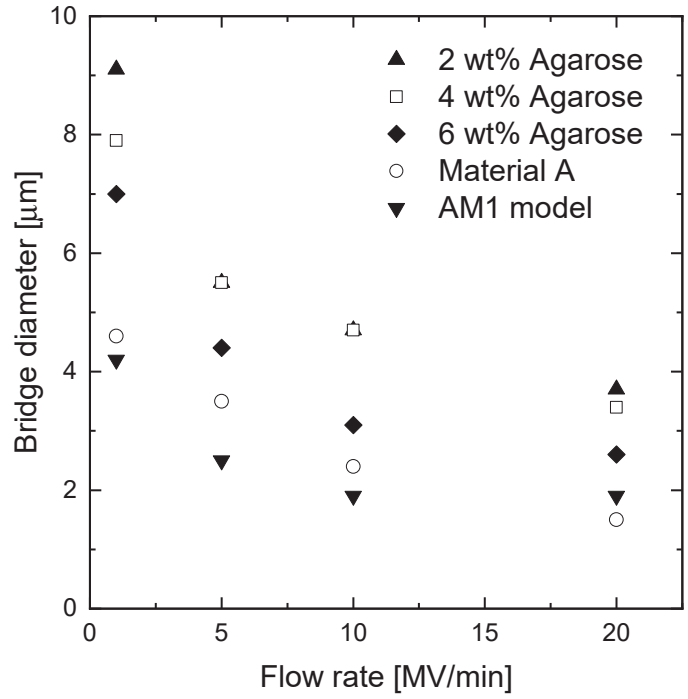

(b) Bridge sizes calculated from the optimum convective porosities for $1\,g/L$

Figure 10.8.: Convective porosities and bridge size diameters for different flow rates leading to maximum $DBC_{10\,\%}$ at a feed concentration of $1\,g/L$

10.3. Conclusion

In this chapter, the membrane design was investigated and optimized. Depending on the diffusive species and the flow rate in the process the membrane bridge diameter, also known as the diffusive pathway is adapted.

- In order to ensure a pressure drop of at maximum $2\,\mathrm{bar}$ the permeability of the membrane bed should be $100\text{-}\,150\,\mathrm{mD}$ at a membrane bed height of $8\,\mathrm{mm}$ and a residence time of $12\,\mathrm{s}$.
- A single layer of the membrane should have a porosity of $\varepsilon_c = 0.43$ and a mean convective pore diameter of $d_{\mathrm{pore}} = 2.59\,\mu\mathrm{m}$ to ensure the specified permeability of $150\,\mathrm{mD}$ and leaving a safety margin for permeability loss during device integration.
- The bridge diameter has to be in the range between $1\,\mu\mathrm{m}$ to $10\,\mu\mathrm{m}$
- Convective porosity and bridge diameter that lead to the maximum $\mathrm{DBC}_{10\,\%}$ are highly depending on the volumetric flow rate (residence time) and the diffusive structure (diffusive mass transfer)

11. Potential analysis for membrane adsorber used in technical processes

In this chapter, dynamic binding capacities at 1 and 10 % of the total breakthrough are shown for different potential membrane materials. Those results are compared to the current status membrane material and conventional resins. Productivities for an exemplary technical process are calculated. The improvement of the productivity, when membrane adsorbers are used instead of conventional beads, is shown.

11.1. Dynamic binding capacities of membrane adsorbers used in technical processes

As shown previously, the structure of membrane adsorbers differs from those in resin columns. In a technical process this leads to an other process behavior. In Figure 11.1 the $DBC_{10\,\%}$ for different residence times are compared for resin and membrane adsorber processes. The experimental data in Figure 11.1a are taken from the respective data sheets. The graph is then simulated using the general rate model. Model parameters are taken from Pabst, Thai and Hunter [Pabs2018]. In Figure 11.1b potential membrane adsorbers, that have a similar diffusive structure to conventional resin material, is modeled and compared to current status membrane material.

Due to smaller diffusive pathways membrane adsorbers can be used at lower residence times than resin packed columns. Commonly, resin based processes are run at residence times of 4 to 8 minutes, whereas membrane adsorbers reach their maximum $DBC_{10\,\%}$ already at residence times of 12 to 20 seconds. By using membrane adsorbers with high binding capacities, the cycle time of a process can be drastically reduced. The shape of the $DBC_{10\,\%}$-curves is dependent on the mass transfer inside the stationary phase: Fast diffusive mass transfer of short diffusive path length lead to constant $DBC_{10\,\%}$ even at very short residence times.

In a process, the loading step is usually stopped before breakthrough occurs. As a criterion to estimate this moment, $DBC_{1\,\%}$ is used. In Figure 11.2 the resulting dynamic binding capacities at 1 % breakthrough for different membrane materials are shown. The agarose structure is simulated with the data presented in Table 6.1 and the membrane characteristics are taken from Section 10.2. The AM1 model

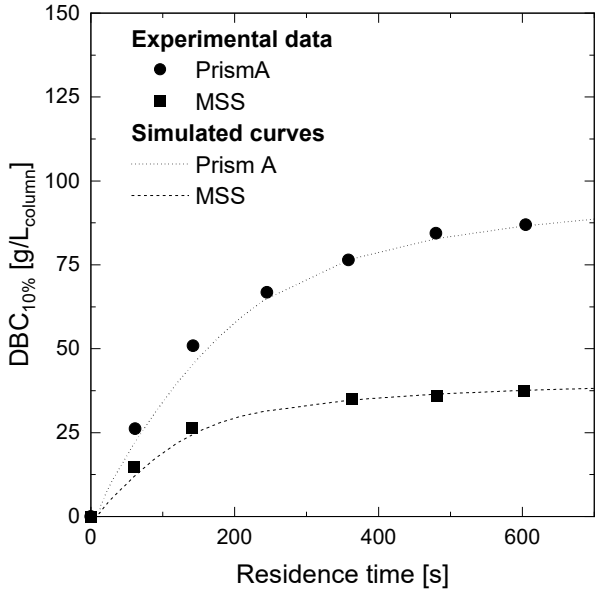

(a) Resin packed columns. Experimental data taken from GE datasheet, model parameters for simulations taken from [Pabs2018].

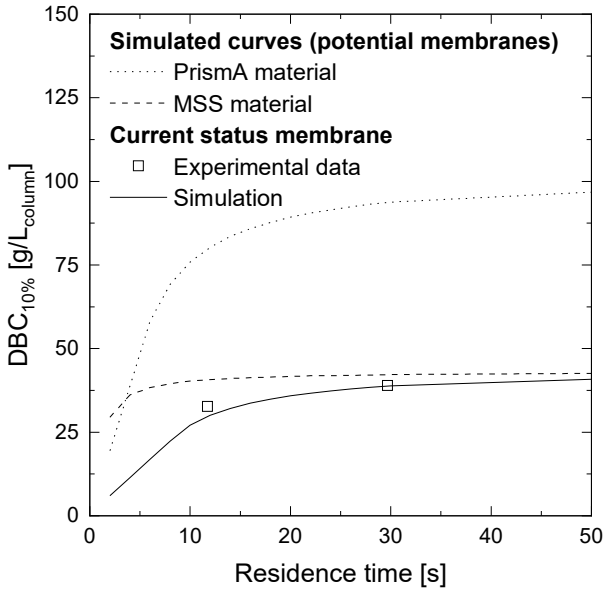

(b) Experimental and simulated data for current status and potential membranes with material characteristics of PrismA and MSS.

Figure 11.1.: Comparison of residence time dependent $DBC_{10\,\%}$ values for resins and membrane adsorbers

membrane material is from an early development state and therefore shows lower $DBC_{1\%}$ than the current status membrane material.

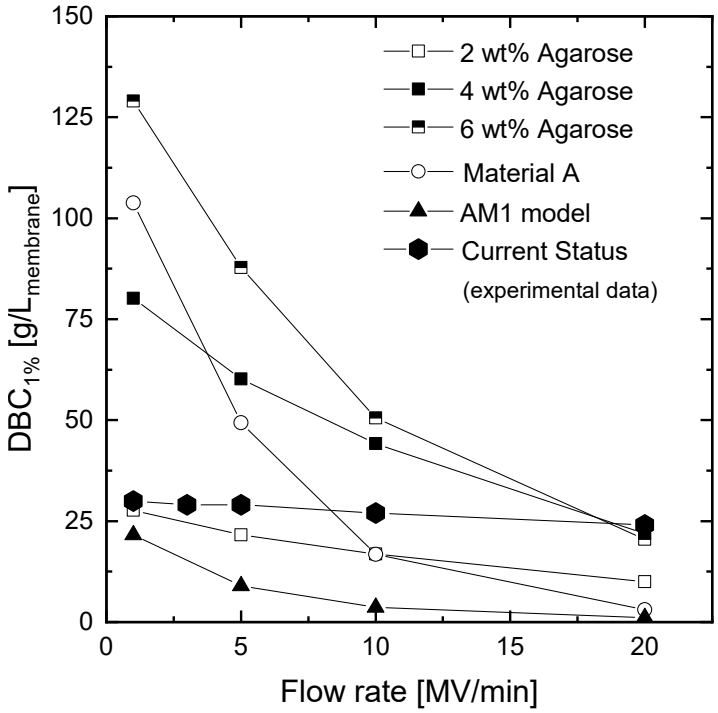

Figure 11.2.: Simulated dynamic binding capacities at 1 % breakthrough for different volumetric flow rates and different membrane adsorbers. The experimental data of the current status membrane is taken from [Sart2020].

The dynamic binding capacities at 1 % breakthrough decrease with increasing flow rate for all membrane materials, due to lower residence times in the adsorber bed, leading to an earlier breakthrough. The $DBC_{1\%}$ values are independent from the concentration of the feed. However, with increasing volumetric flow rate, the dynamic binding capacity gets smaller for all membranes. This is due to diffusive limitation inside the membrane bridges. The three membranes differ in agarose concentration, resulting in different diffusion coefficients, diffusive porosities and static binding capacities, cf. Table 6.1. The effect is reflected in the slope of the curves. The higher the diffusive limitation, the more the $DBC_{1\%}$ curve decreases with increasing flow rate. At low flow rates, 6 wt% agarose membranes and the potential membrane with Material A stationary phase, that have a high specific surface which is available for binding, show the highest $DBC_{1\%}$. The higher the agarose concentration, the steeper the decent of the curve with increasing flow rate. This is due to the poorer accessibility at lower residence times. This leads to

a critical flow rate, at which the binding capacities of lower agarose concentrations have higher $DBC_{1\,\%}$: At $20\,MV/min$ the $4\,wt\%$ agarose material shows a higher $DBC_{1\,\%}$ than the $6\,wt\%$ agarose material.

For the productivity of a process, next to the $DBC_{1\,\%}$ the loading time is important. The loading time decreases with increasing feed concentration, because of the increased driving force for diffusive mass transfer in the membrane bridges.

11.2. Process productivities

Simulations showed, that the impact of the surrounding tubings and valves is negligible when the chromatographic bed and the flow rate are sufficiently large, cf. Figure A.16 in the appendix.

The productivity of different membrane adsorber beds in dependence on the volumetric flow rate was investigated. The results for $DBC_{1\,\%}$ and for the productivity of one cycle for different volumetric flow rates at a feed concentration of $5\,g/L$ are presented in Figure 11.3. The productivities of potential membrane adsorber are compared to the state of the art PrismA bead material from GE.

The productivity shows a maximum for each membrane configuration at a specific flow rate, as there is a trade-off between bound mass and residence time. Due to the diffusive limitation, the optimum flow rate decreases with decreasing pore diffusion coefficient, as does the maximum productivity.
The productivity of a conventional bead process at a flow rate of $0.25\,MV/min$ with PrismA material is $\approx 9\,g/L.h$. This value is highly dependent on the assumed process. With the current status membrane from Sartorius, the productivity at a flow rate of $5\,MV/min$ is already increased by the factor of 22 to about $200\,g/L.h$. With increasing flow rate, the productivity can be further increased. Using an optimal designed membrane adsorber with e.g. $6\,wt\%$ agarose at a flow rate of $5\,MV/min$ and assuming ideal flow distribution in the device, the productivity of the potential chromatography process can be increased by the factor of 60 up to $\approx 560\,g/L.h$. At higher flow rates the productivity can even be increased by the factor of 90 compared to conventional resin processes.

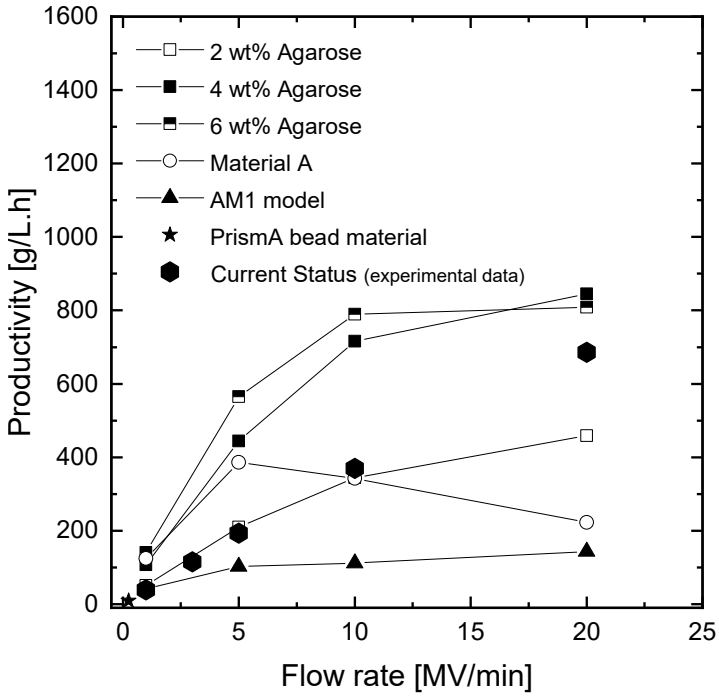

Figure 11.3.: Process productivities of several membrane materials and PrismA bead material for different flow rates at a feed concentration of $c_{\text{Feed}} = 5\,\text{g/L}$. The feed concentration fo the current status experiments was $c_{\text{Feed}} = 0.9\,\text{g/L}$ [Sart2020]. The flow rate for the PrismA bead process is $0.25\,\text{CV/min}$. For membrane configurations cf. Table 6.1 and for the considered process, cf. Section 10.2.

11.3. Conclusion

In this chapter the membrane adsorber process was investigated.

- At residence times from 4 to 8 min $DBC_{10\,\%}$ values up to $80\,g/L_{column}$ are reached with resin chromatography. Using membranes residence times can be reduced to 10 to 20 seconds without loosing binding capacity, because of smaller diffusive pathways.
- The $DBC_{1\,\%}$, indicating that the loading step of the process is stopped, is dependent on the flow rate and the available specific surface for binding. Up to $20\,MV/min$ the highest $DBC_{1\,\%}$ is achieved with a 6 wt% agarose.
- The process productivity is independent of the surrounding system, when the membrane bed is sufficiently high.
- Assuming ideal flow distribution, the process productivity is increased by the factor of 60 for an optimized membrane adsorber compared to conventional state of the art resin processes.

12. Conclusion and outlook

Chromatography steps are primarily employed in the downstream of bioprocesses for the production of biotherapeutics. Conventional resins are limited regarding diffusive mass transfer due to large diffusive pathways. Membrane adsorbers with porous membrane bridge material are an alternative to reduce the mass transfer limitation and the residence time in the chromatographic bed to several seconds without loosing dynamic binding capacity.
In this work, the membrane material is optimized regarding productivity, utilization of the membrane material and mechanic stability, using physical mathematical modeling.

In Chapter 7, the agarose structure was investigated and diffusion coefficients for IgG were determined using resins with an agarose concentration in the range from $2\,\mathrm{wt\%}$ to $6\,\mathrm{wt\%}$. With increasing agarose concentration the diffusive pore diameter decreases, leading to an increased specific surface. Next to the increase of the agarose concentration, the adsorption of IgG leads to a decrease of the diffusive pore diameter. Due to IgG adsorption, the diameter of each pore is reduced by twice the time of the IgG's hydrodynamic diameter leading to a lower IgG diffusivity. The diffusive mass transfer of IgG lies in the range between $\approx 4 \cdot 10^{-12}\,\mathrm{m^2/s}$ and $6.5 \cdot 10^{-12}\,\mathrm{m^2/s}$ for $2\,\mathrm{wt\%}$ to $6\,\mathrm{wt\%}$, respectively. The correlation between the diffusion coefficient and the agarose concentration is described with a modification of the Ogston and the Boyer model. At an agarose concentration of $8\,\mathrm{wt\%}$ there is almost no accessibility of the diffusive pores and the binding capacity decreases drastically.
The design of membrane adsorbers with diffusive membrane bridges for the separation of larger target molecules as e.g. VLPs or viral vectors is of great interest for future research. The scope of this work was to define the limits of the application. With increasing target molecule diameter the pore diffusion coefficient and the pore accessibility decrease. The agarose platform is applicable for molecules with diameters up to $30\,\mathrm{nm}$, using a minimum agarose concentration of $1\,\mathrm{wt\%}$. For larger target molecules convective membrane adsorbers should be used.
The optimum agarose concentration is highly dependent on the diffusivity of the target molecule, the diffusive pathway and the applied volumetric flow rate.

The impact of flow distribution and device integration is investigated in Chapter 8 by residence time distributions. Experiments and CFD simulations showed that the

dead volume in the devices has to be minimized to obtain sharp RTD. Increasing membrane bed height up to 8 mm leads to sharpening of RTD. Beyond that, there is no a significant improvement. Convective porosity and permeability do not have a significant influence on the simulated RTD in the considered range. Using CFD simulations, the impact of the housing and the membrane on the RTD of the device could be separated. In a LP15 device, the influence of the housing dominates the RTD of the total device. When the dead volume is optimized, as in a 3 mL Nano, the impact of the housing on the RTD of the total device can be neglected.

In Chapter 9, breakthrough curves of membrane adsorbers were simulated using the general rate model. To this end the effective pore diffusion coefficient was determined by fitting the simulation to experimental data. The effective pore diffusion coefficient was determined to be $0.9 \cdot 10^{-12}\,\mathrm{m^2/s}$, which is significantly lower than the ones presented in the literature for the used agarose concentration. This might be caused by agarose structure or the fact, that the used 1D model is not capable to describe the influence of flow distribution on breakthrough curves. The impact of the distribution might therefore be lumped into the fitted effective pore diffusion coefficient.
In future work a 3D model of the membrane adsorber could be developed to take into account the different flow through membrane areas and its effect on the breakthrough curve.

The design of the stationary phase was optimized in Chapter 10. In order not to exceed a maximum allowed pressure drop of 2 bar the permeability of the membrane bed should be 100- 150 mD. A single layer of the membrane should therefore have a convective porosity of $\varepsilon_c = 0.43$ and a mean convective pore diameter of $d_{\mathrm{pore}} = 2.59\,\mu\mathrm{m}$. Future research should focus on the impact of device integration on the membrane and the consequences on the diffusive mass transfer in the porous membrane bridges.
The optimal size of the membrane bridges highly depends on the target molecule size, the used agarose concentration and the residence time. In order to ensure the highest possible accessibility, the membrane bridge diameter should be between $1\,\mu\mathrm{m}$ to $10\,\mu\mathrm{m}$ for IgG and agarose concentrations between 2 and 6 wt%.

In the Chapter 11 dynamic binding capacities at 10 % of the total breakthrough of conventional resins and potential membrane materials of different agarose

concentrations are compared. For residence times from 4 to 8 min, $DBC_{10\,\%}$ values up to $80\,g/L_{column}$ are reached with resin chromatography. Using membranes, residence times can be reduced up to 20 s without reducing binding capacity due to smaller diffusive pathways.

A model process is calculated and the productivities for PrismA resins are compared to the potential membrane materials. The $DBC_{1\,\%}$, indicating that the loading step of the process is stopped, is dependent on the flow rate and the available specific surface for binding. The highest $DBC_{1\,\%}$ is achieved with a 6 wt% agarose for flow rates up to 20 MV/min. The process productivity is independent of the surrounding system, when the membrane bed is sufficiently large. In future process considerations, the elution step should be simulated as well: With short elution volumes, the target molecule concentration can be increased and the process time reduced.

Assuming ideal flow distribution, the process productivity can be increased by the factor of 90 for an optimized membrane adsorber compared to conventional state of the art resin processes. With the current status of the membrane, which is still under development, the productivity can already be improved by the factor of 22.

A. Appendix

A

A.1. State of the art

A.1.1. Binding mechanisms

Table A.1.: Separation mechanism used in chromatography [Goed2006a]

Typ	Interactions	Application
Adsorption	surface binding, steric interaction, hydrogen bounds van der waals forces	isomers
Hydrophobic interaction (HIC)	hydrophobic complexes, salination effects	proteins, antibodies
Affinity	biospecific adsorption	antibodies
Ion exchange (IEX)	ionic binding	proteins
Size exclusion (SEC)	steric exclusion	proteins, DNA, viruses

A.1.2. Breakthrough curves

The impact of mass transfer phenomena on the slope of the breakthrough curve is presented in Figure A.1.

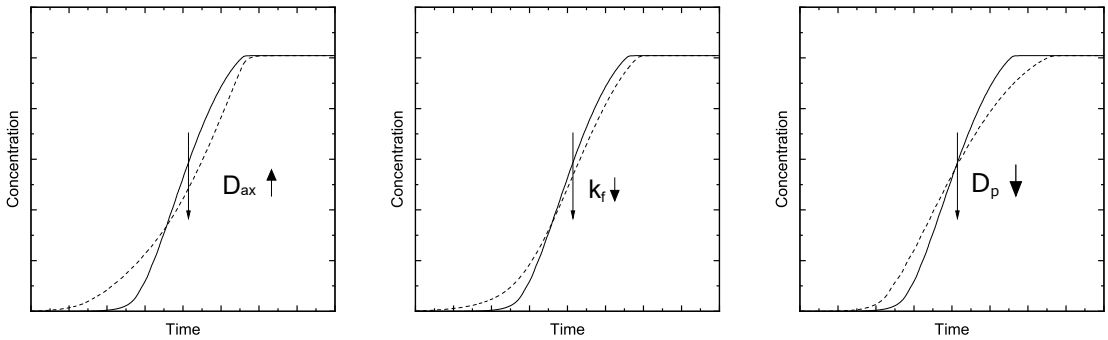

(a) Axial dispersion **(b)** Film diffusion **(c)** Pore diffusion

Figure A.1.: Influence of axial dispersion, film diffusion and pore diffusion on the breakthrough curve

The axial dispersion mainly depends on the packing quality, as well as on the flow rate. With increasing axial dispersion, the deviation from plug flow increases (compare Section 3.2.5) and breakthrough occurs earlier. With decreasing film mass transfer coefficient, the transfer over the boundary layer decreases and the breakthrough curve flattens. A slower diffusive mass transfer in the pores of the stationary phase also shows a premature breakthrough and a flattened curve.

A.1.3. Characterization of column efficiency

Statistical moments

First statistical moment:

$$\mu_t = \frac{\int_0^\infty c \cdot t \mathrm{d}t}{\int_0^\infty c \mathrm{d}t} \tag{A.1}$$

Second statistical moment:

$$\sigma^2 = \frac{\int_0^\infty c \cdot (t - \mu_t)^2 \mathrm{d}t}{\int_0^\infty c \mathrm{d}t} \tag{A.2}$$

The symmetry of the response peak or peak skew can be determined with the third statistical moment:

$$\mathrm{Skew} = \frac{\int_0^\infty c \cdot (t - \mu_t)^3 \mathrm{d}t}{\sigma^3 \int_0^\infty c \mathrm{d}t} \tag{A.3}$$

In case of $\mathrm{Skew} \approx 0$ the peak is symmetrical, for $\mathrm{Skew} > 0.7$ the peak is highly asymmetrical. [Cart2010]

HETP models

The solutions for a response to pulse, step or periodic injections with a linear isotherm and a linear driving force model are summarized in Carta and Jungbauer [Cart2010], Table 8.1.

Models with non-linear isotherms are more difficult to solve and are usually solved by a numerical computer simulation. However, some analytical solutions for

special cases are available to predict the dynamic binding capacity. In case of a rectangular or irreversible isotherm ($\frac{1}{1+K \cdot c_0} \approx 0$), which is relevant in many protein chromatography applications, the ratio of dynamic to equilibrium binding capacity can be described with the following equation [Cart2010]:

$$\frac{\mathrm{DBC}_{10\%}}{\mathrm{EBC}} \approx 1 - \frac{1.03 + 1.3\frac{n_{\mathrm{pore}}}{n_{\mathrm{film}}}}{n_{\mathrm{pore}}}. \tag{A.4}$$

when pore diffusion is dominant Equation A.4 reduces to

$$\frac{\mathrm{DBC}_{10\%}}{\mathrm{EBC}} \approx 1 - \frac{1.03}{n_{\mathrm{pore}}}. \tag{A.5}$$

$n = 2 \cdot N$ is the number of transfer units and is calculated with

$$n_{\mathrm{pore}} = \frac{15 \cdot \frac{1-\varepsilon_{\mathrm{p}}}{\varepsilon_{\mathrm{p}}} \cdot D_{\mathrm{p}} \cdot L}{r_{\mathrm{p}}^2 \cdot u_{\mathrm{int}}} \tag{A.6}$$

and

$$n_{\mathrm{film}} = \frac{3 \cdot \frac{1-\varepsilon_{\mathrm{p}}}{\varepsilon_{\mathrm{p}}} \cdot k_{\mathrm{f}} \cdot L}{r_{\mathrm{p}}^2 \cdot u_{\mathrm{int}}} \tag{A.7}$$

A.1.4. Chromatographic material

Agarose

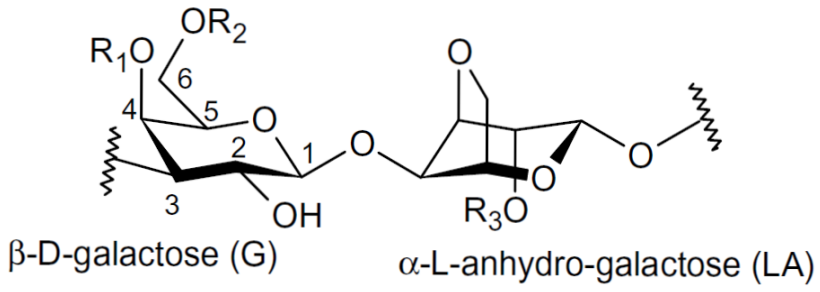

Figure A.2.: Structure of agarose from red seaweed. R_1 = H or SO_3^-; R_2 = H or CH_3; R_3 = H or SO_3^- or CH_3 [Maci2008]

A

Derivation of the Carman-Kozeny correlation

For the estimation of friction numbers and corresponding pressure drops for fixed beds with granular particles, the Ergun equation is used

$$\Psi = \frac{150}{\mathrm{Re}} + 1{,}75 \qquad \text{with} \quad \mathrm{Re} = \frac{\rho \cdot d_\mathrm{p} \cdot u}{\mu}. \tag{A.8}$$

For Reynolds numbers ≤ 1 equation A.8 reduces to $\Psi = \frac{150}{\mathrm{Re}}$. The friction number Ψ is defined as:

$$\Psi = \frac{\varepsilon_\mathrm{c}^3}{(1-\varepsilon_\mathrm{c})^2} \cdot \frac{\Delta p \cdot d_\mathrm{p}}{\rho \cdot u^2 \cdot L_\mathrm{c}} \tag{A.9}$$

Combining the reduced form of equations A.8 and equation A.9 the Carman-Kozeny equation [Darc1856] results:

$$\frac{\Delta p}{L_\mathrm{c}} = \frac{150(1-\varepsilon_\mathrm{c})^2}{\varepsilon_\mathrm{c}^3} \cdot \frac{\mu \cdot u}{d_\mathrm{p}^2} \tag{A.10}$$

Derivation of the law of Hagen-Poiseuille

The forces on a fluid element of the length $\mathrm{d}x$ and the thickness $\mathrm{d}r$ in a tube are shown in Figure A.3. The forces F are induced by pressure and τ describes the between two fluid elements.

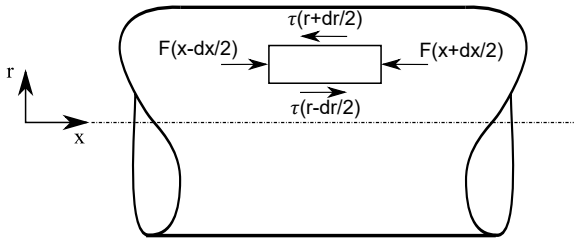

Figure A.3.: Force balance in a tube

Balance of forces on a fluid element in a tube:

$$\begin{aligned}\left(p - \frac{\partial p}{\partial x}\frac{\mathrm{d}x}{2}\right) \cdot 2\pi r \mathrm{d}r - \left(p + \frac{\partial p}{\partial x}\frac{\mathrm{d}x}{2}\right) \cdot 2\pi r \mathrm{d}r + \\ \left(\tau - \frac{\partial \tau}{\partial r}\frac{\mathrm{d}r}{2}\right) \cdot 2\pi \left(r - \frac{\mathrm{d}r}{2}\right) \mathrm{d}x - \left(\tau + \frac{\partial \tau}{\partial r}\frac{\mathrm{d}r}{2}\right) \cdot 2\pi \left(r + \frac{\mathrm{d}r}{2}\right) \mathrm{d}x = 0\end{aligned} \tag{A.11}$$

$$\Leftrightarrow -\frac{\partial p}{\partial x} - \frac{\tau}{r} - \frac{\partial \tau}{\partial r} = 0 \tag{A.12}$$

First integration in radial direction:

$$-\frac{\partial p}{\partial x} = \frac{1}{r}\frac{\partial (\tau \cdot r)}{\partial r} \tag{A.13}$$

$$\Leftrightarrow \int_0^R -r \cdot \frac{\partial p}{\partial x} \mathrm{d}r = \int_0^{\tau R} \mathrm{d}(\tau r) \tag{A.14}$$

$$\Leftrightarrow -\frac{R}{2} \cdot \frac{\partial p}{\partial x} + \frac{C_1}{R} = \tau \tag{A.15}$$

with

$$\tau = -\mu \cdot \frac{\partial u}{\partial R} \tag{A.16}$$

Equation A.15 becomes

$$-\frac{R}{2}\frac{\partial p}{\partial x} + \frac{C_1}{R} = -\mu \cdot \frac{\partial u}{\partial R} \tag{A.17}$$

Second integration in radial direction:

$$\int_0^r \frac{R}{2}\frac{\partial p}{\partial x} + \frac{C_1}{R} \mathrm{d}R = \int_0^u \mu \mathrm{d}U \tag{A.18}$$

$$\Leftrightarrow \frac{1}{4} r^2 \frac{\partial p}{\partial x} + C_1 \cdot \ln(r) + C_2 = \mu \cdot U \tag{A.19}$$

With the boundary conditions

$$U(r = R) = 0 \tag{A.20}$$

$$U(r = 0) \neq 0 \Rightarrow C_1 = 0 \tag{A.21}$$

C_2 is calculated from Equation A.19:

$$C_2 = -\frac{1}{4} r^2 \frac{\partial p}{\partial x} \tag{A.22}$$

The velocity profile of a tube flow results:

$$U(r) = \frac{r^2 - R^2}{4 \cdot \mu} \frac{\partial p}{\partial x} \tag{A.23}$$

By integration of the velocity, the law of Hagen-Poiseuille is derived:

$$\dot{V} = \int_0^R U(r) \cdot 2\pi r \mathrm{d}r \tag{A.24}$$

$$\Leftrightarrow \dot{V} = \frac{\pi \cdot R^4}{8 \cdot \mu} \cdot \frac{\Delta p}{\Delta x} \tag{A.25}$$

Mechanics

The change of length leads to transverse contraction:

$$\varepsilon_\mathrm{x} = \frac{1}{E} \cdot (\sigma_\mathrm{x} - \nu \cdot (\sigma_\mathrm{y} + \sigma_\mathrm{z})) \tag{A.26}$$

$$\varepsilon_\mathrm{y} = \frac{1}{E} \cdot (\sigma_\mathrm{y} - \nu \cdot (\sigma_\mathrm{x} + \sigma_\mathrm{z})) \tag{A.27}$$

$$\varepsilon_\mathrm{z} = \frac{1}{E} \cdot (\sigma_\mathrm{z} - \nu \cdot (\sigma_\mathrm{x} + \sigma_\mathrm{y})) \tag{A.28}$$

where ν is defined as Poisson's ratio and describes the expansion of a material in directions perpendicular to the direction of compression.
In Figure A.4 a force is directed at the membrane with a square base area in z-direction. Due to the device, it is assumed, that no strain is possible in x- and y-direction.

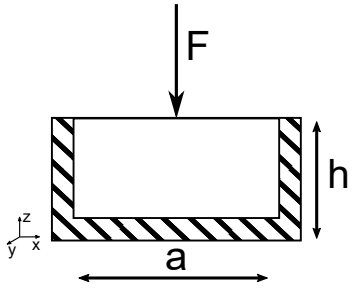

Figure A.4.: Force on a membrane in z-direction

$$\sigma_z = \frac{F}{a^2} \tag{A.29}$$

$$\varepsilon_z = \frac{1}{E} \cdot (\sigma_z - \nu \cdot (\sigma_x + \sigma_y)) \tag{A.30}$$

$$\varepsilon_x = 0 \tag{A.31}$$

$$\varepsilon_y = 0 \tag{A.32}$$

Mathematical conversions lead to

$$\varepsilon_z = \frac{\Delta h}{h} = \frac{\sigma_z}{E} \cdot \left(1 - \frac{2\nu^2}{1-\nu}\right) \tag{A.33}$$

A.1.5. Mass transfer

Open and closed boundary conditions

At closed boundary conditions, the flow pattern changes at the boundaries. There is no flow across the boundary. For open boundary conditions the flow is undisturbed at the boundaries.

Residence time distribution

Pure convection model The pure convection model is applied for $\mathrm{Bo} = \frac{D_0 \tau}{x^2} \to 0$. The Bodenstein number describes the ratio of fluid dynamic residence time ($\tau = V/\dot{V}$) and diffusion time ($t_D = x^2/D_0$). Convectional mass transfer is dominant, whereas axial and radial diffusion are negligibly small. There is no diffusive exchange between the streamlines. This regime is called completely segregated flow. In this case Equation 3.13 reduces to

$$\frac{\partial c}{\partial t} = u(r)\frac{\partial c}{\partial x}. \tag{A.34}$$

The residence time distribution for a fully developed laminar flow is given by

$$E(t) = \frac{\tau^2}{2t^3}. \tag{A.35}$$

The minimum individual residence time is $t_{\text{min}} = 0{,}5\tau$ for the fluid element flowing on the tube axis. Fluid elements near to the wall cause tailing. Further information on this topic can be found in [Emig2017].
The derivation of the residence time distribution for a fully developed laminar flow is given in the following. The radial velocity distribution in the tube is described by:

A

$$u(r) = u_{\text{max}} \left[1 - \frac{r^2}{R^2}\right] \tag{A.36}$$

$$u_{\text{max}} = 2\bar{u} = \frac{2 \cdot \dot{V}}{\pi \cdot R^2} \tag{A.37}$$

The individual residence time t of a fluid element in the tube is

$$t(r) = \frac{L}{u(r)} = \frac{\tau \cdot \bar{u}}{2\bar{u} \cdot \left(1 - \frac{r^2}{R^2}\right)} \tag{A.38}$$

with τ describing the fluid dynamic residence time. A correlation for the sum function of the residence time is given by

$$F(r) = \frac{\int_0^r \mathrm{d}\dot{V}}{\dot{V}} = \frac{\int_0^r u(r) \cdot 2\pi r \mathrm{d}r}{\dot{V}} = 2\frac{r^2}{R^2} - \frac{r^4}{R^4} \tag{A.39}$$

Using Equation A.38 the sum function can be expressed as a function of time:

$$F(t) = 1 - \frac{\tau^2}{4t^2} \tag{A.40}$$

which becomes

$$E(t) = \frac{\tau^2}{2t^3} \tag{A.41}$$

after differentiation with respect to t.

Axial Dispersion model The axial dispersion model is applied for $\text{Bo} = \frac{D_0 t}{x^2} \approx 1$. Diffusion becomes more important and super imposes the convective flow. The diffusive exchange between the streamlines is non negligable for this partial segregated flow, which can be described with the dispersion model. In non-

ideal flow reactors, the radial dispersion can usually be neglected [Emig2017], because the radial concentration gradient is sufficiently small compared to the axial concentration gradient. When the coordinate system is moving with u, Equation 3.13 simplifies to

$$\frac{\partial c}{\partial t} = D_{\text{ax}} \cdot \frac{\partial^2 c}{\partial x^2} \tag{A.42}$$

and the residence time distribution is derived to

$$E(t) = \frac{1}{2} \cdot \sqrt{\frac{\text{Bo}}{\pi \cdot t}} \cdot \exp\left(-\text{Bo}\frac{(1-t)^2}{4 \cdot t}\right). \tag{A.43}$$

For derivation compare [Emig2017], chapter 6. The dispersion coefficient is given as a function of the Bodenstein number (Bo)

$$D_{\text{ax}} = \frac{d^2 \cdot u^2}{192 \cdot D_0} \quad \text{for} \quad \text{Bo} > 10^2 \quad \text{[Tayl1953]} \tag{A.44}$$

$$D_{\text{ax}} = D_0 + \frac{d^2 \cdot u^2}{192 \cdot D_0} \quad \text{for} \quad \text{Bo} < 10^2 \quad \text{[Aris1956]} \tag{A.45}$$

Pure diffusion model The pure diffusion model is applied for $\text{Bo} = \frac{D_0 t}{x^2} \to \infty$. Convective flow is negligibly small compared to diffusion. Equation 3.13 simplifies to

$$\frac{\partial c}{\partial t} = D_{\text{ax}} \cdot \frac{\partial^2 c}{\partial x^2} \tag{A.46}$$

with $D_{\text{ax}} = D_0$. [Emig2017]

The regime depends on the Bodenstein number and ratio of tube length to the diameter of the tracer molecule, cf. Figure A.5.

RTD Models

In literature several methods for the determination of the residence time of the device are presented. A detailed overview is given in the study of Ham and Platzer [Ham2004].

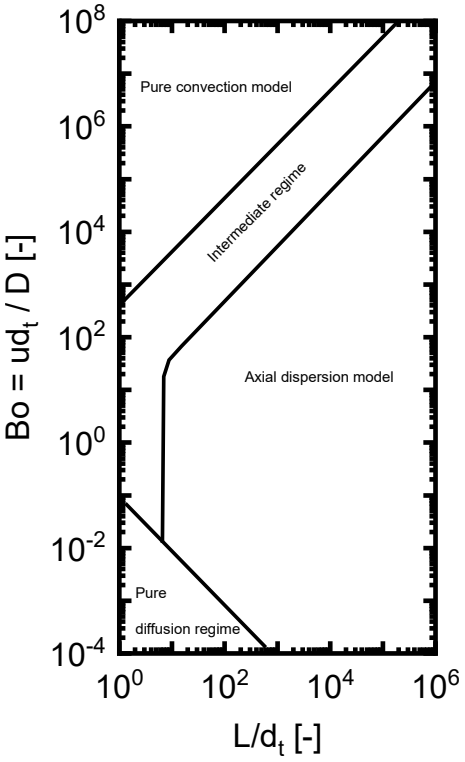

Figure A.5.: Tracer transport regime adapted from [Leve2011] and [Anan1965]

Fourier transformation

$$E(t) = \frac{1}{2\pi} \int_{-\infty}^{\infty} \frac{\int_0^{\infty} c_{\text{out}} \cdot \exp^{-i\omega t}\, \mathrm{d}t}{\int_0^{\infty} c_{\text{in}} \cdot \exp^{-i\omega t}\, \mathrm{d}t} \mathrm{d}\omega \tag{A.47}$$

This method leads directly to the RTD of the device. But as experimental data are transformed, the Fourier transformation leads to a drastic increase of noise. The results are often impractical, but they sometimes can be improved by curve smoothing. An alternative is the use of models.
[Bošk2008; Leve1999]

One-dimensional axial dispersed plug flow model When the flow of the fluid is assumed to be a plug flow which is superimposed with some backmixing, the mass balance over one volume element gives

$$\frac{\partial c}{t} = D_{\text{ax}} \frac{\partial^2 c}{\partial x^2} - u \frac{\partial c}{\partial x}. \tag{A.48}$$

Solving this equation with "open" boundary conditions, cf. Appendix A.1.5, and results in

$$E(t) = \sqrt{\frac{\mathrm{Bo}}{4\pi\tau t} \cdot \exp\left(\frac{-\mathrm{Bo}\cdot\tau}{4t}\left(1-\frac{t}{\tau}\right)^2\right)} \tag{A.49}$$

where Bo is the Bodenstein number ($\mathrm{Bo} = \frac{uL}{D_{ax}}$) and τ the mean residence time. [Leve1999]

Tank in series model The plate model from Martin and Synge [Mart1941] describes the RTD by tanks connected in series. This model can be used, when the dispersion model is used. It gives the best results, when the deviation from a plug flow is not too large.

$$E(t) = \frac{t^{N-1}}{\mu^N} \cdot \frac{N^N}{(N-1)!} \cdot \exp\left(-\frac{tN}{\mu}\right) \tag{A.50}$$

where $N = \frac{\mu_t^2}{\sigma^2}$ is the number of theoretical plates. [Leve1999]

Film transfer

Lewis and Whitman have developed the film theory. A substance is transferred from a stationary wall into a streaming fluid [Lewi1924]. The concentration at the wall is c_0 and decreases to the concentration of the fluid c (compare Figure A.6). The mass transfer takes place in a fluid film of the thickness δ close to the wall. The following assumptions were made:

- rigid boundary layer
- flow parallel to the boundary layer
- mass transfer only in y-direction
- constant concentrations, diffusion coefficients and stationary hydrodynamic conditions
- $u(y = 0) = 0$

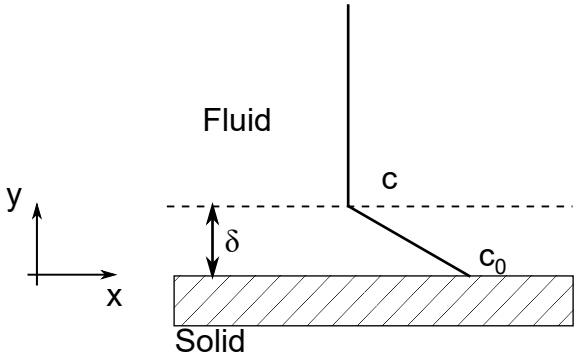

Figure A.6.: Film theory according to [Lewi1924]: Mass transfer in a fluid film close to the wall

A

Diffusion

$$\frac{\partial c}{\partial t} = D \cdot \nabla^2 c \tag{A.51}$$

which becomes

$$\frac{\partial c}{\partial t} = D \left(\frac{\partial^2 c}{\partial x_1^2} + \frac{\partial^2 c}{\partial x_2^2} + \frac{\partial^2 c}{\partial x_3^2} \right) \tag{A.52}$$

for cartesian coordinates. Using cylindrical coordinates Equation 3.17 becomes:

$$\frac{\partial c}{\partial t} = \frac{1}{r} \left\{ \frac{\partial}{\partial r} \left(rD \frac{\partial c}{\partial r} \right) + \frac{\partial}{\partial \theta} \left(\frac{D}{r} \frac{\partial c}{\partial \theta} \right) + \frac{\partial}{\partial z} \left(rD \frac{\partial c}{\partial z} \right) \right\} \tag{A.53}$$

The corresponding equation for spherical coordinates is:

$$\frac{\partial c}{\partial t} = \frac{1}{r^2} \left\{ \frac{\partial}{\partial r} \left(r^2 D \frac{\partial c}{\partial r} \right) + \frac{1}{\sin\theta} \frac{\partial}{\partial \theta} \left(D \sin\theta \frac{\partial c}{\partial \theta} \right) + \frac{D}{\sin^2\theta} \frac{\partial^2 c}{\partial \phi^2} \right\} \tag{A.54}$$

In the following analytical solutions of Equation 3.16 are presented for cartesian and cylindrical coordinates.

A.2. Modeling

Diffusion into different geometries

Plate Considering diffusion into a plate, it is assumed that the mass transfer only takes place in x-direction. In this case, the concentration at both sides of the plate is c_0 and diffusion occurs symmetrically.
The initial condition is

$$c(-L < x < L) = 0 \tag{A.55}$$

and the corresponding boundary conditions are

$$c(x = L) = c_0 \tag{A.56}$$
$$c(x = -L) = c_0 \tag{A.57}$$
$$\frac{\partial c}{\partial x}|_{x=0} = 0 \tag{A.58}$$

The concentration in place x at time t can be calculated using the analytical solution of [Cran1979]:

$$c(x,t) = c_0 - \frac{4 \cdot c_0}{\pi} \cdot \sum_{n=0}^{\infty} \frac{(-1)^n}{2n+1} \cdot \exp\left\{\frac{-D \cdot (2n+1)^2 \cdot \pi^2 t}{4L^2}\right\} \cdot \cos\frac{(2n+1)\pi x}{2L} \tag{A.59}$$

Cylinder A circular cylinder with only radial diffusion is considered. A solution for constant surface concentration and an initial radius dependent concentration inside the cylinder is given literature [Cran1979], [Cuss2009]. When the initial condition

$$c(0 < r < R) = f(r) = c_1(r) \tag{A.60}$$

and boundary conditions

$$c(r = R) = c_0 \tag{A.61}$$
$$\frac{\partial c}{\partial r}|_{r=0} = 0 \tag{A.62}$$

are applied, the analytical solution of Equation A.53 is

$$\frac{c - c_1}{c_0 - c_1} = 1 - \frac{2}{R} \cdot \sum_{n=1}^{\infty} \frac{\exp\left(-D\alpha_n^2 t\right) \cdot J_0(r\alpha_n)}{\alpha_n J_1(a\alpha_n)} \tag{A.63}$$

where α_n are the positive roots of $J_0(r\alpha_n) = 0$. J_0 and J_1 are first kind Bessel functions of order zero and of first order respectively.

A

Hollow cylinder A hollow cylinder with a concentration c_0 in the inner cylinder is considered. For the initial condition

$$c(R_{in} < x < R_{out}) = 0 \tag{A.64}$$

and the boundary conditions

$$c(r = R_{in}) = c_0 \tag{A.65}$$

$$\frac{\partial c}{\partial r}|_{r=R_{out}} = 0 \tag{A.66}$$

the analytical solution can be found in [Cran1979].

Particle For the diffusion into a particle, the initial and boundary conditions of the cylinder are valid. The analytical solution is given in literature [Cran1979].

$$\frac{c - c_1}{c_0 - c_1} = 1 + \frac{2a}{\pi r} \sum_{n=1}^{\infty} \frac{(-1)^n}{n} \cdot \sin\left(\frac{n\pi r}{a}\right) \exp(-Dn^2\pi^2 \frac{t}{a^2}) \tag{A.67}$$

A.2.1. Diffusion into membrane bridges

The structure of the diffusive domains of an agarose membrane, also referred to as membrane bridges, is shown in Figure 6.1.
The surface consists of convex and concave areas which can be described by a mixture of coordinate systems: spheres, slabs, cylinders and hollow cylinders (flow from the center to outer regions).
A selection of analytical solutions for spheres, plates, cylinders and hollow cylinders is given in Appendix A.2. Taking into consideration different geometries with equal

diffusive pathways and equal diffusion coefficients, the concentration in the centre of the geometry (particle and cylinder at $r = 0$, plate at $x = 0$) increases with decreasing speed in the following order: Particle, cylinder, plate. This is due to the rejuvenation in the direction of diffusion. Accordingly, the concentration at R_{out} of the hollow cylinder increases slower than in other geometries. This fact is schematically represented in Figure A.7.

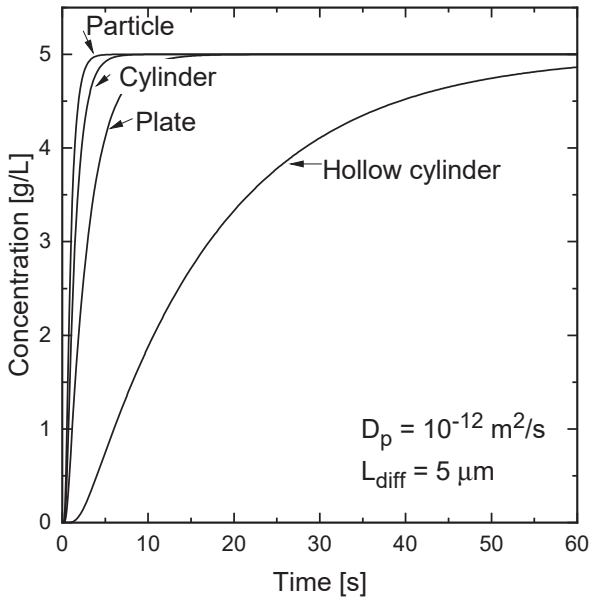

Figure A.7.: Comparison of diffusion into the presented geometries (numerical solution with gProms)

The impact of the diffusive geometry on breakthrough curves is shown in Figure A.8.

Due to the impact of the geometry on the filling speed, breakthrough curves for stationary phases of different geometries differ in steepness. For the description of the diffusive geometries of the membrane, a plate geometry is assumed to fit best.

A.2.2. Calculation of the static binding capacity

The diffusive porosity is assumed to be 0.5. The assumption is based on the data given in the paper of Pabst, Thai and Hunter [Pabs2018]. With that the accessible surface for binding is $12.5\,\mathrm{m}^2/\mathrm{mL}_{\mathrm{acc.volume}}$. The specific static binding capacity is $q^* = 22.4\,\mathrm{mg}/\mathrm{m}^2_{\mathrm{acc.surface}}$. Calculating the specific surface which is available for other

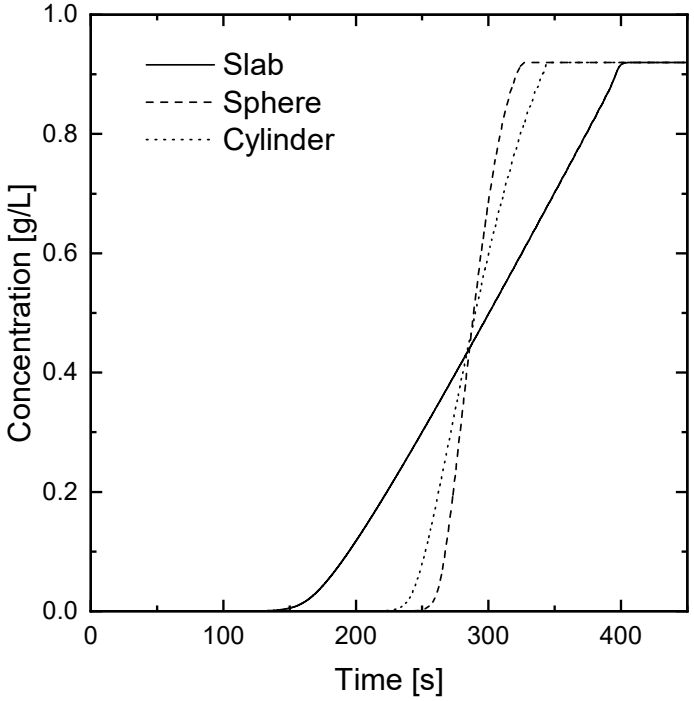

Figure A.8.: Comparison of different diffusive geometries: Slab, sphere and cylinder. Modeling parameters are summarized in Table A.10.

agarose concentrations the static binding capacity is calculated.

A.2.3. Initial and boundary conditions for GRM

At time $t = 0$ the column is assumed to be empty:

$$c_{\mathrm{i}}(t = 0) = 0 \tag{A.68}$$

$$c_{\mathrm{p,i}}(t = 0, r) = 0 \tag{A.69}$$

$$q_{\mathrm{i}}(t = 0, r) = 0 \tag{A.70}$$

The adsorbent stays in the column. Therefore, only in- and outlet boundary conditions of the mobile phase are necessary. Often-times, Danckwert's boundary conditions or "closed boundary conditions" [Danc1953] are used.

A.3. Material and methods

Particle porosity determination

Nitrogen ad- and desorption: In this method, the change of gas pressure caused by nitrogen adsorption and capillary condensation, is measured. The pores are assumed to be rigid and of the same shape, either cylinders or parallel-sided slits. The pore width can be calculated using different exemplary correlation: Kelvin equation, density functional theory (DFT) [Last1993] or the Horvath-Kawazoe equation [Horv1983].

Mercury intrusion porosimetry Mercury does not wet most surfaces and must be forced to enter pores by the application of external pressure. The relationship between pressure and capillary diameter is described by Washburn [Wash1921].

Pore size distribution

The pore size distribution coefficient K_D is calculated by

$$K_D = \frac{V_i - V_{int}}{V_c - V_{int}} \tag{A.71}$$

The pore size is determined with a model which describes the partitioning of the standard compounds into the pores. A random plane model for monodispersed pores is proposed by Giddings et al. [Gidd1968]:

$$K = \exp\left(-s \cdot r_h\right) \tag{A.72}$$

where s describes the specific surface area of the pores and r_h the hydrodynamic radius of the tracer.
Assuming a distribution of pores, the pore partition coefficient can be obtained by integration [Tatá2008]:

$$K_D = \int_0^\infty K \cdot f_v \mathrm{d}r_{pore} \tag{A.73}$$

The probability density function f_v can either be described by a Gaussian relation:

$$f_v = \exp\left(-0{,}5 \cdot \left(\frac{r-\bar{r}}{\sigma}\right)^2\right) \tag{A.74}$$

where $\bar{r}$ is the mean pore radius and σ the standard deviation of the distribution. According to DePhillips and Lenhoff this relation is physically unrealistic as it permits negative values of r [DePh2000]. Using a log-normal distribution, $f_v(r \leqslant 0) = 0$ [Korn2000]:

$$f_v = \frac{1}{\sigma r\sqrt{2\pi}} \cdot \exp\left(-\frac{\ln\left(\frac{r}{\bar{r}}\right)}{2\sigma^2}\right) \tag{A.75}$$

Tatárová et al. pointed out, that the dependence of the normalized partition coefficient versus the solute hydrodynamic radius can often be described by a monodisperse model [Tatá2008]. When a model with pore distribution is applied, attention has to be paid regarding the obtained parameters, as standard deviation and mean pore radius are both fitting parameter and influence each other.

A.3.1. CFD modeling

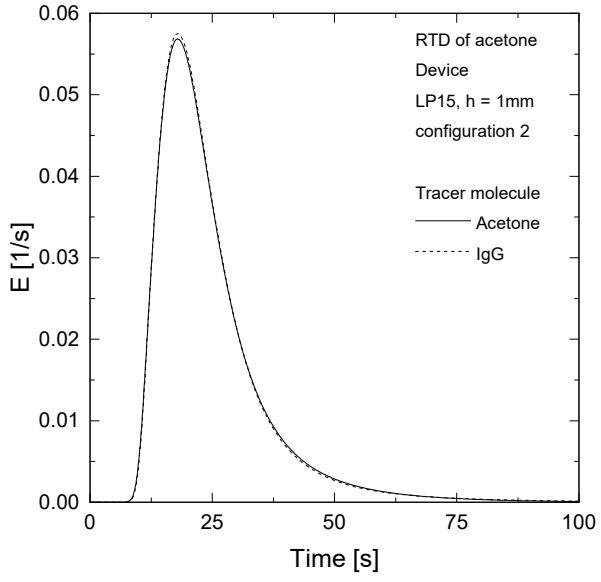

Figure A.9.: Impact of tracer molecule size on the RTD of the device

A.3.2. Membrane experiments

Pressure-flow correlation

Assumptions:

- The agarose volume is constant
- No strain in x or z-direction
- Material compression only influences the convective pore diameter and length

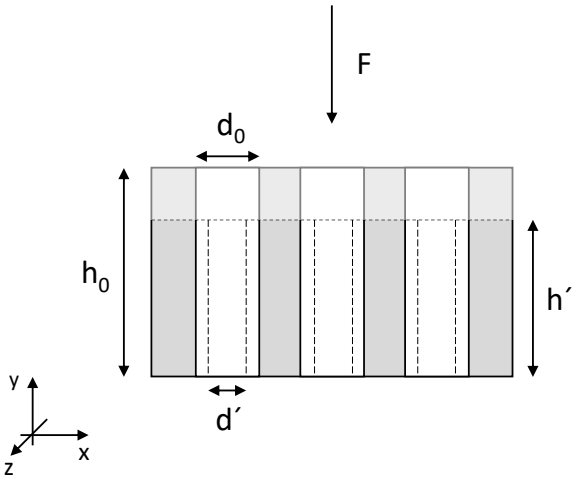

Figure A.10.: Influence of a force applied on a porous membrane

$$\Rightarrow {d'_{\text{pore}}}^2 = \frac{d^2_{\text{pore},0}\left(1 - \frac{1-\varepsilon_D}{\varepsilon}\right)}{\varepsilon_D} \tag{A.76}$$

A.3.3. Simulative approach

A fluid flow through porous media, taking into account viscous shearing stress, is described by the Brinkman equation:

$$\rho\left(\frac{\partial u_{\text{int}}}{\partial t} + u_{\text{int}} \cdot \nabla u_{\text{int}}\right) = -\nabla p + \nabla\left(\eta\left(\nabla u_{\text{int}} + (\nabla u_{\text{int}})^T\right)\right) - \frac{\eta}{\kappa} \cdot u_{\text{int}} \tag{A.77}$$

A.4. Results and discussion

A.4.1. Impact of porosity and permeability on RTD

The impact of the porosity and the permeability on the residence time distribution is shown in Figure A.11. With increasing porosity the RTD slightly shifts to higher times, as more convective volume in the membrane is available. In the considered range, the permeability has no noteworthy impact on the residence time distribution of the acetone tracer in the simulation.

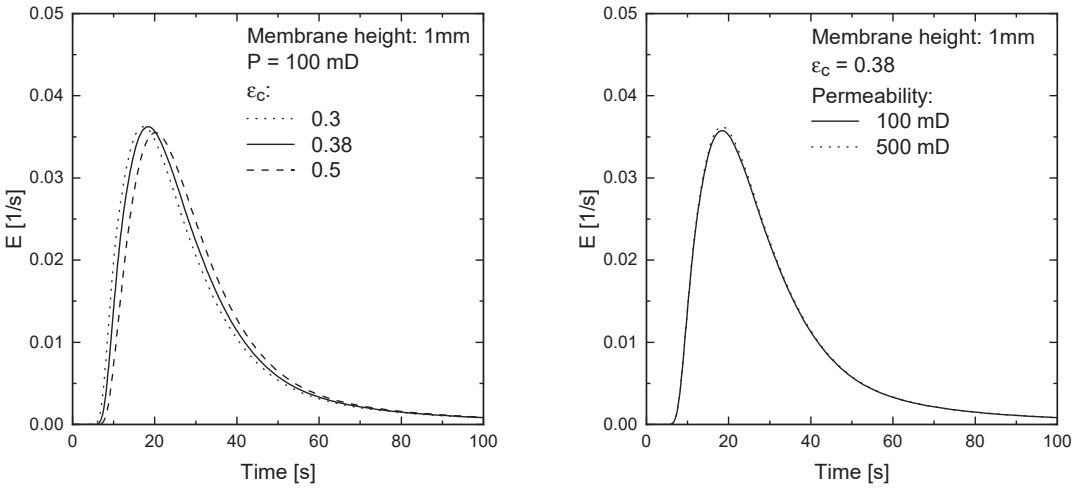

(a) Porosity variation

(b) Permeability variation

Figure A.11.: Simulated tracer peaks, using 2 v% acetone, over membranes with different porosities and permeabilities in a LP15 laboratory device. Bed height $h = 1\,\mathrm{mm}$. Volumetric flow rate $5\,\mathrm{MV/min}$. CFD simulations were performed with configuration 1, cf. Figure 8.5.

A.4.2. Parameters equivalent circuit of the housing

Table A.2.: Parameters for the equivalent circuit of the housing's RTD for a bed height of 1 mm

	Parameter		1 MV/min	5 MV/min	10 MV/min	20 MV/min
CSTR	V	$[\mathrm{m}^3]$	$1.09 \cdot 10^{-6}$	$1.01 \cdot 10^{-6}$	$1.00 \cdot 10^{-6}$	$1.11 \cdot 10^{-6}$
DPFR	D_{ax}	$[\mathrm{m}^2/\mathrm{s}]$	0.0131	0.0282	0.0799	0.1153
	L_{tube}	[m]	2.062	1.890	2.090	1.8584
	A	$[\mathrm{m}^2]$	$2.48 \cdot 10^{-6}$	$2.48 \cdot 10^{-6}$	$2.48 \cdot 10^{-6}$	$2.48 \cdot 10^{-6}$

Table A.3.: Parameters for the equivalent circuit of the housing's RTD for a bed height of 8 mm at a flow rate of 1 MV/min

Parameter			
CSTR	V	$[m^3]$	$1.69 \cdot 10^{-7}$
DPFR	D_{ax}	$[m^2/s]$	$1.01 \cdot 10^{-13}$
	L_{tube}	[m]	$2.00 \cdot 10^{-10}$
	A	$[m^2]$	$2.48 \cdot 10^{-6}$

A.4.3. Modeling the Äkta system at different flow rates

Table A.4.: Results of the parameter fitting for the Äkta Prime system

Parameter			LP15, 1 MV/min 0.9 mL/min	3 mL Nano, 1 MV/min 3 mL/min	LP15, 5 MV/min 4.3 mL/min
CSTR	V	$[m^3]$	$1.30 \cdot 10^{-7}$	$2.28 \cdot 10^{-7}$	$2.62 \cdot 10^{-7}$
DPFR	D_{ax}	$[m^2/s]$	$1.00 \cdot 10^{-4}$	$2.5 \cdot 10^{-3}$	$7.6 \cdot 10^{-3}$
	L_{tube}	[m]	1.25	1.86	2.01

The cross section area of th the DPFR is adapted to the inner diameter of the used tubings in the experiments, which is $2.48 \cdot 10^{-7}\ m^2$.

Table A.5.: Modeling parameters for membrane adsorbers with the AM1 membrane.

	Unit	Equation	3 mL prototype device AM1	LP15 0.5 mL AM1	
Geometry					
V	m^3		$3 \cdot 10^{-6}$	$0.5 \cdot 10^{-6}$	
L	m		$8 \cdot 10^{-3}$	$1 \cdot 10^{-3}$	
ε_c			0.38	0.38	
$\varepsilon_{p,IgG}$		(iSEC)	0.69		
r	m	Distribution shown in Figure 9.2	x1.5	x1	x1
Transport					
$\dot{V}$	MV/min		1.5	1	5
τ	s	$V/\dot{V}$	40	60	12
u_{int}	m/s	Nano: Eq. 6.17; $L_c/(\tau\varepsilon_c)$	$2.36 \cdot 10^{-4}$	$4.38 \cdot 10^{-4}$	$2.19 \cdot 10^{-4}$
D_{ax}	m^2/s	HETP $\cdot\ u_{int}/2$	$1.27 \cdot 10^{-8}$	$1.27 \cdot 10^{-8}$	$8.88 \cdot 10^{-8}$
ρ	kg/m^3		997		
μ	Pa.s		$8.91 \cdot 10^{-4}$		
D_0	m^2/s		$4.50 \cdot 10^{-11}$		
Re		$du\rho/(\mu\varepsilon_c)$	Calculated from bridge size distribution		
Sc		$\mu/(\rho D_0)$	$1.99 \cdot 10^{-4}$		
k_f	m/s	$1.15u_{int}/\varepsilon_c \cdot Re^{-0.5}Sc^{-2/3}$	Calculated from bridge size distribution		
D_p	m^2/s	Parameterfit	$9 \cdot 10^{-13}$		
Adsorption					
K	$m^3/mol.s$		25000		
q_m	mol/m^3		1.20	0.63	0.63

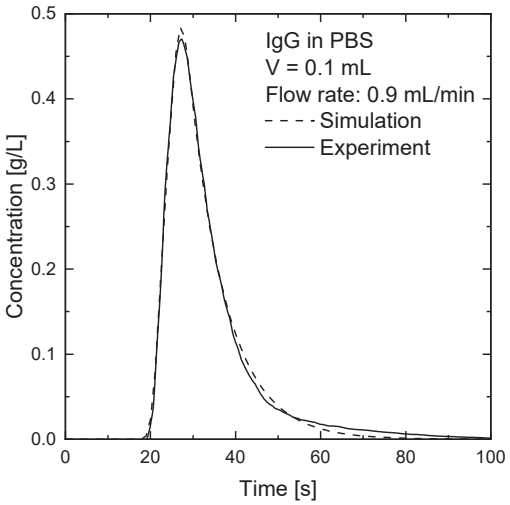

(a) $1\,\mathrm{g/L}$ IgG in PBS at $\dot{V} = 0.9\,\mathrm{ml/min}$

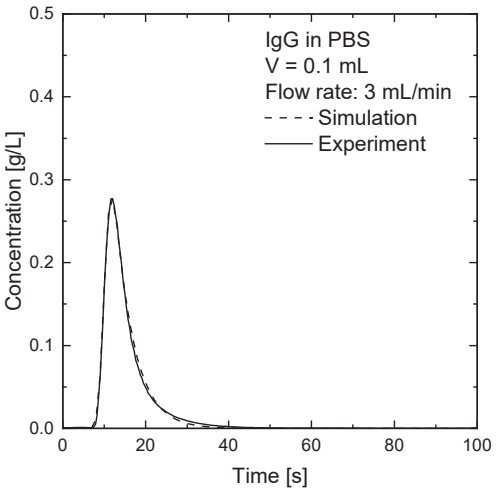

(b) $1\,\mathrm{g/L}$ IgG in PBS at $\dot{V} = 3.0\,\mathrm{ml/min}$

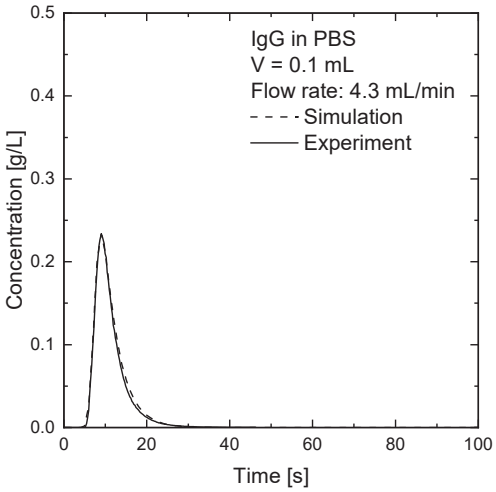

(c) $1\,\mathrm{g/L}$ IgG in PBS at $\dot{V} = 4.3\,\mathrm{ml/min}$

Figure A.12.: Fitted tracer peaks of IgG for the Äkta Prime system at different volumetric flow rates. Parameters are summarized in Table A.4.

A.4.4. Diffusive constraints

Table A.6.: Parameters for the process approach of diffusive constraints

	4 wt% agarose			2 wt% agarose	6 wt% agarose		
Parameter	$\varepsilon_c = 0.3$	$\varepsilon_c = 0.2$	$\varepsilon_c = 0.4$	$\varepsilon_c = 0.3$		$\varepsilon_c = 0.3$	
c_0				1 g/L			
V				$5 \cdot 10^{-7}$ m^3			
A				$5.23 \cdot 10^{-4}$ m^2			
L				$9.56 \cdot 10^{-4}$ m^3			
ρ				997 kg/m^3			
μ				$8.91 \cdot 10^{-4}$ Pa.s			
D_0				$4.5 \cdot 10^{-11}$ m^2/s			
Sc				$1.99 \cdot 10^4$			
τ s		12		12	12	60	6
$\varepsilon_{p,IgG}$		0.58		0.63		0.47	
D_{eff} m^2/s		$5.72 \cdot 10^{-12}$		$6.5 \cdot 10^{-12}$		$3.96 \cdot 10^{-12}$	
q_{max} mol/m^3		1.49		0.68		1.98	
D_{ax} m^2/s	$1.33 \cdot 10^{-8}$	$1.99 \cdot 10^{-8}$	$9.96 \cdot 10^{-9}$	$1.33 \cdot 10^{-8}$	$1.33 \cdot 10^{-8}$	$2.22 \cdot 10^{-8}$	$2.22 \cdot 10^{-7}$
u_{int} m/s	$2.66 \cdot 10^{-4}$	$3.99 \cdot 10^{-4}$	$1.99 \cdot 10^{-4}$	$2.66 \cdot 10^{-4}$	$2.66 \cdot 10^{-4}$	$4.44 \cdot 10^{-4}$	$4.44 \cdot 10^{-3}$
Re	$1.98 \cdot 10^{-3}$	$4.46 \cdot 10^{-3}$	$1.11 \cdot 10^{-3}$	$1.98 \cdot 10^{-3}$	$1.98 \cdot 10^{-3}$	$3.32 \cdot 10^{-3}$	$3.32 \cdot 10^{-2}$
k_f m/s	$3.12 \cdot 10^{-5}$	$4.68 \cdot 10^{-5}$	$2.34 \cdot 10^{-5}$	$3.12 \cdot 10^{-5}$	$3.12 \cdot 10^{-5}$	$4.03 \cdot 10^{-5}$	$1.28 \cdot 10^{-5}$

A.4.5. Membrane characteristic constraints

Table A.7.: Parameters for the model of Ham et al. [Ham2004] used to determine the RTD of different devices with CM membrane

Device	N	M	t_{min}	t_{max}	Error
LP15	2.7222	19	5.5742	31.3889	0.0078
1 ml Nano	2.7062	4	13.9257	149.9958	0.000675
3 ml Nano	2.5431	6	5.6729	15.1120	0.0197
0,8 L device	2.1000	7	9.9466	33.0864	0.00063511

Table A.8.: Parameters for the model of Ham et al. [Ham2004] used to determine the RTD of the membrane and the housing. Calculations based on CFD simulations

Device	N	M	t_{min}	t_{max}	Error
LP15	1.4187	8	5.8412	110.0023	0.0018

A.4.6. Viscosity of IgG solution

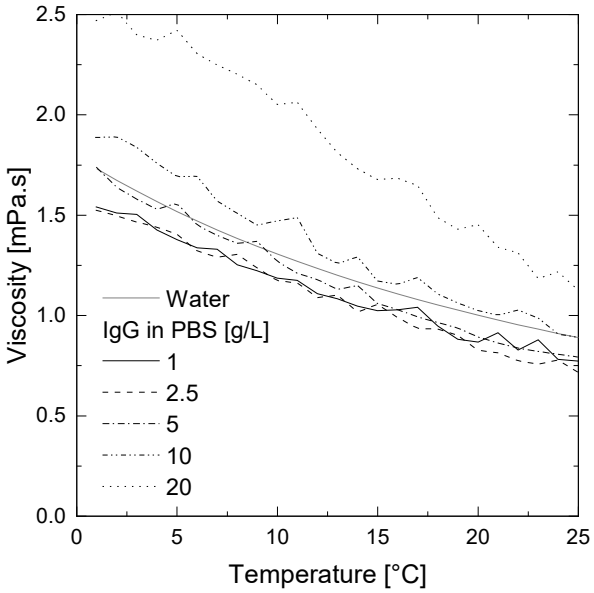

Figure A.13.: Viscosity data for IgG solution measured according to Section 5.1. Viscosity of a $1\,\mathrm{g/L}$ IgG in PBS buffer and water (data taken from the VDI-Wärmeatlas [Step2019])

A.4.7. Membrane stability

Farazdaghi Harris approach:

$$\varepsilon = (a + b \cdot \Delta p^c)^{-1}, \tag{A.78}$$

with Δp in $10^5\mathrm{Pa}$. Parameters are summarized in Table A.9.

Table A.9.: Parameters for the fit correlations

Approach	a	b	c
Farazdaghi Harris	0.99946	$1.32422 \cdot 10^{-4}$	0.57507

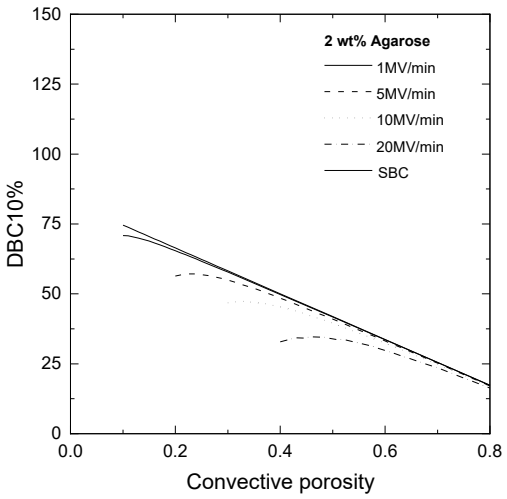

(a) Membrane material 2 wt% agarose

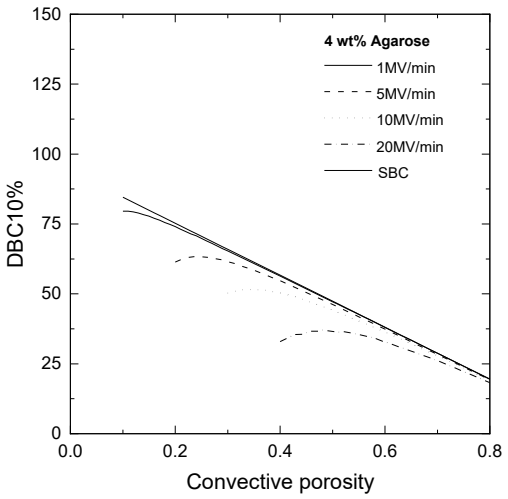

(b) Membrane material 4 wt% agarose

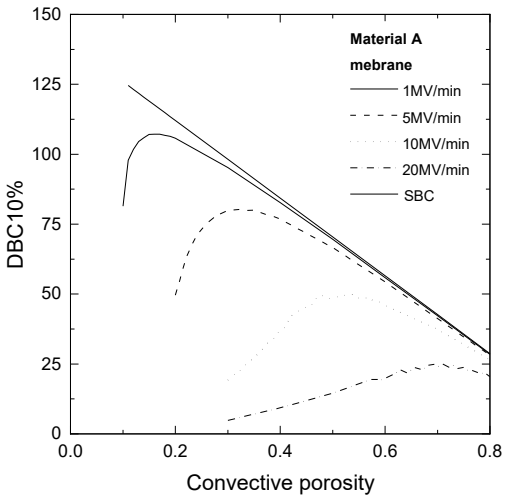

(c) Potential membrane with Material A

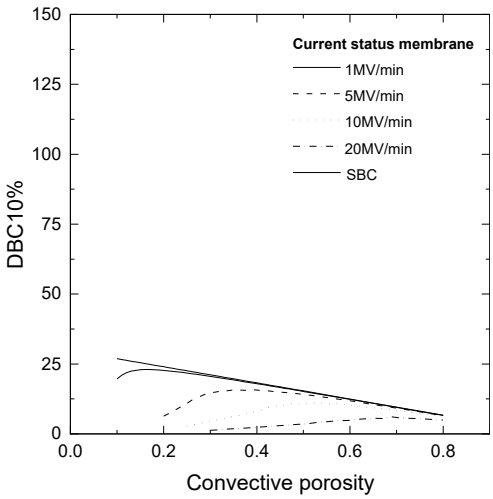

(d) Current status membrane material

Figure A.14.: $DBC_{10\,\%}$-values for different convective porosities showing a trade-off between binding volume and diffusive mass transfer for a feed concentration of 1 g/L. For membrane configurations, cf. Table 6.1

The results in Figure A.15 show exemplary for 6 wt% agarose, that the influence of the feed concentration on the optimum convective porosity and bridge diameter is negligible.

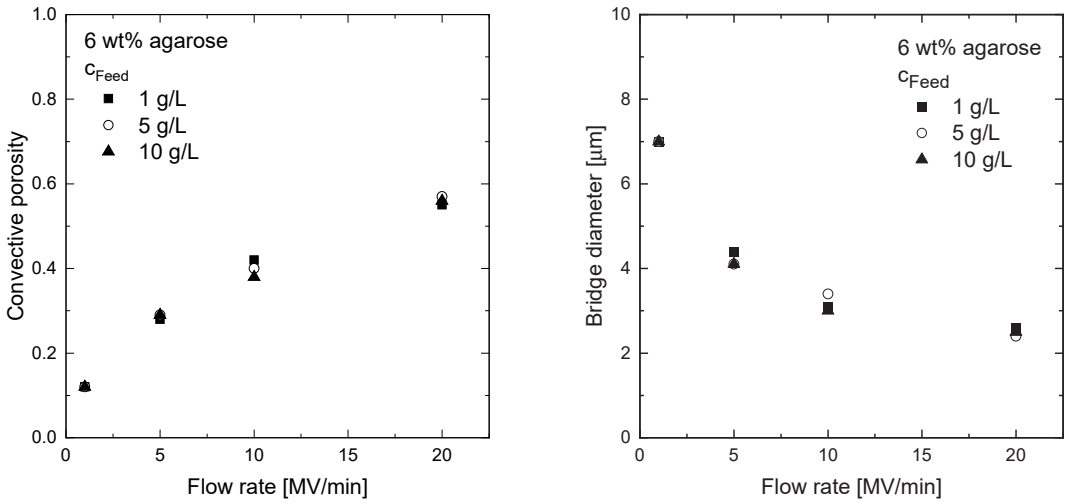

(a) Influence of c_{Feed} on convective porosities that yield in the maximum $DBC_{10\,\%}$-values for 6 wt% agarose

(b) Influence of the feed concentration on bridge diameters that yield in the maximum $DBC_{10\,\%}$-values for 6 wt% agarose

Figure A.15.: Porosities and bridge size diameters for different flow rates leading to maximum $DBC_{10\,\%}$ for 6 wt% agarose at different feed concentrations

A.4.8. Potential analysis on membrane performance

Table A.10.: Modeling parameters for the comparison of diffusive geometries (cf. Figure A.8)

Parameter	Unit	Equation	Value
Geometry			
V	m^3		$1.90 \cdot 10^{-6}$
L	m		$2.69 \cdot 10^{-3}$
A	m^2	V/L	$7.07 \cdot 10^{-4}$
ε_c			0.30
$\varepsilon_{p,IgG}$			0.49
r	m		$2.00 \cdot 10^{-6}$
Transport			
$\dot{V}$	m^3/s	$5\,MV/min \cdot V$	$1.58 \cdot 10^{-7}$
τ	s	$V/\dot{V}$	12
u_{int}	m/s	$L/(\tau\varepsilon_c)$	$7.47 \cdot 10^{-4}$
HETP	m		0.0001
D_{ax}	m^2/s	$HETP \cdot u_{int}/2$	$3.73 \cdot 10^{-8}$
ρ	kg/m^3		997
μ	Pa.s		$8.91 \cdot 10^{-4}$
D_0	m^2/s		$4.50 \cdot 10^{-11}$
Re		$du\rho/(\mu\varepsilon_c)$	$5.57 \cdot 10^{-3}$
Sc		$\mu/(\rho D_0)$	$1.99 \cdot 10^{-4}$
k_f	m/s	$1.15 u_{int}/\varepsilon_c \cdot Re^{-0.5} Sc^{-2/3}$	$5.23 \cdot 10^{-5}$
Adsorption			
K	$m^3/mol.s$		25000
q_m	mol/m^3		0.39

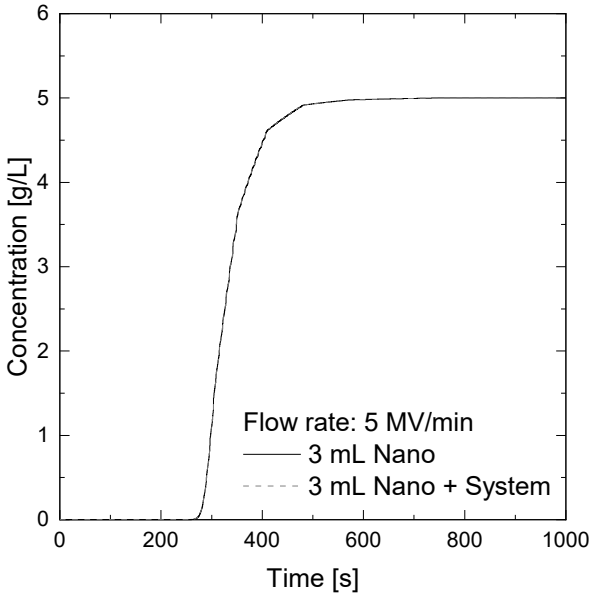

Figure A.16.: Comparison of breakthrough curve of a process without system and with system.

Bibliography

[Afey1990] N. B. Afeyan et al. “Flow-through particles for the high-performance liquid chromatographic separation of biomolecules: perfusion chromatography”. *Journal of Chromatography A* 519.1 (1990). (Cit. on p. 28).

[Alte1997] U. Altenhöner et al. “Parameter estimation for the simulation of liquid chromatography”. *Journal of Chromatography A* 769.1 (1997). (Cit. on p. 40).

[Anan1965] V. Ananthakrishnan, W. N. Gill, and A. J. Barduhn. “Laminar dispersion in capillaries: Part I. Mathematical analysis”. *AIChE journal* 11.6 (1965). (Cit. on pp. 33, 164).

[Ande1958] D. K. Anderson, Hall, and A. L. Babb. “Mutual diffusion in non-ideal binary liquid mixtures”. *The Journal of Physical Chemistry* 62.4 (1958). (Cit. on pp. 23, 73).

[Ande1969] N. S. Anderson et al. “X-ray diffraction studies of polysaccharide sulphates: double helix models for k-and i-carrageenans”. *Journal of molecular biology* 45.1 (1969). (Cit. on p. 22).

[Appl2009] Applied Biosystems. “POROS Perfusion Chromatography Media: Accelerate your process to a new speed”. 2009 (2009). (Cit. on p. 27).

[Aris1956] R. Aris. “On the dispersion of a solute in a fluid flowing through a tube”. *Proceedings of the Royal Society of London. Series A. Mathematical and Physical Sciences* 235.1200 (1956). (Cit. on p. 163).

[Arno1974] S. Arnott et al. “The agarose double helix and its function in agarose gel structure”. *Journal of molecular biology* 90.2 (1974). (Cit. on p. 22).

[Avra2003] M.-E. Avramescu et al. “Preparation of mixed matrix adsorber membranes for protein recovery”. *Journal of membrane science* 218.1-2 (2003). (Cit. on p. 28).

[Bara2019] K. Baran et al. “Effect of flow behavior in extra-column volumes on the retention pattern of proteins in a small column”. *Journal of Chromatography A* 1598 (2019). (Cit. on pp. 33, 39, 73, 87).

[Barb2009] S. Barbe. “Fluid dynamics in Sartobind membrane adsorber systems”. PhD thesis. Hannover: Gottfried Wilhelm Leibniz Universität Hannover, 2009 (cit. on p. 30).

[Bemb2003] I. Bemberis, A. Noyes, and Natarajan Venkatesh. “Column Packing for Process-Scale Chromatography: Guidelines for Reproducibility”. *BioPharm International Guide* (2003). (Cit. on p. 55).

[Bird2015] R. B. Bird et al. *Introductory transport phenomena*. Wiley New York, 2015 (cit. on p. 38).

[Boi2007] C. Boi, S. Dimartino, and G. C. Sarti. “Modelling and simulation of affinity membrane adsorption”. *Journal of Chromatography A* 1162.1 (2007). (Cit. on p. 43).

[Boi2008] C. Boi, S. Dimartino, and G. C. Sarti. “Performance of a new protein a affinity membrane for the primary recovery of antibodies”. *Biotechnology progress* 24.3 (2008). (Cit. on pp. 27, 41).

[Bošk2008] D. Bošković and S. Loebbecke. “Modelling of the residence time distribution in micromixers”. *Chemical Engineering Journal* 135 (2008). (Cit. on pp. 62, 164).

[Boye1992] P. M. Boyer and J. T. Hsu. “Experimental studies of restricted protein diffusion in an agarose matrix”. *AIChE journal* 38.2 (1992). (Cit. on pp. 37, 53, 92, 100).

[Bran1988] S. Brandt et al. “Membrane-based affinity technology for commercial scale purifications”. *Bio/technology* 6.7 (1988). (Cit. on p. 29).

[Brau1971] H. Brauer. “Grundlagen der Einphasen-u Mehrphasenströmungen.” *Aarau u. Frankfurt/Main: Verlag Sauerländer* (1971). (Cit. on p. 22).

[Brie1992] K.-G. Briefs and M.-R. Kula. “Fast protein chromatography on analytical and preparative scale using modified microporous membranes”. *Chemical engineering science* 47.1 (1992). (Cit. on pp. 29, 41).

[Carb1960] J. J. Carberry. “A boundary–layer model of fluid–particle mass transfer in fixed beds”. *AIChE journal* 6.3 (1960). (Cit. on p. 37).

[Cart2010] G. Carta and A. Jungbauer. *Protein chromatography: Process development and scale-up*. John Wiley & Sons, 2010 (cit. on pp. 3, 18, 156, 157).

[Char2012] C. Charcosset. *Membrane processes in biotechnology and pharmaceutics*. Elsevier, 2012 (cit. on p. 29).

[Choe2016] W. Choe, T. A. Durgannavar, and S. J. Chung. “Fc-Binding Ligands of Immunoglobulin G: An Overview of High Affinity Proteins and Peptides”. *Materials* 9.12 (2016). (Cit. on p. 20).

[Cook1999] J. C. Cook et al. “Purification of virus-like particles of recombinant human papillomavirus type 11 major capsid protein L1 from Saccharomyces cerevisiae”. *Protein expression and purification* 17.3 (1999). (Cit. on p. 28).

[Cran1979] J. Crank. *The mathematics of diffusion*. Oxford university press, 1979 (cit. on pp. 35, 167, 168).

[Cuss2009] E. L. Cussler. *Diffusion: Mass transfer in fluid systems*. Cambridge university press, 2009 (cit. on pp. 36, 39, 167).

[Danc1953] P. V. Danckwerts. “Continuous flow systems: Distribution of residence times”. *Chemical engineering science* 2.1 (1953). (Cit. on p. 170).

[Darc1856] H. P. G. Darcy. *Les Fontaines publiques de la ville de Dijon. Exposition et application des principes à suivre et des formules à employer dans les questions de distribution d’eau, etc*. V. Dalamont, 1856 (cit. on p. 158).

[Deem1956] J. J. v. Deemter, F. J. Zuiderweg, and A. van Klinkenberg. “Longitudinal diffusion and resistance to mass transfer as causes of nonideality in chromatography”. *Chemical engineering science* 5.6 (1956). (Cit. on p. 18).

[Demm1999] W. Demmer and D. Nussbaumer. “Large-scale membrane adsorbers”. *Journal of Chromatography A* 852.1 (1999). (Cit. on p. 30).

[Demm2007] W. Demmer et al. *Adsorption membranes, method of producing same and equipment, including the adsorption membranes*. 2007 (cit. on p. 28).

[Demm2016] W. Demmer et al. “Cellulose hydrate membrane, method for the production thereof, and use thereof”. 2016 (cit. on p. 55).

[DePh2000] P. DePhillips and A. M. Lenhoff. “Pore size distributions of cation-exchange adsorbents determined by inverse size-exclusion chromatography”. *Journal of Chromatography A* 883.1-2 (2000). (Cit. on p. 172).

[Dijk2001] M. A. v. Dijk and Winkel, Jan G. J. van de. “Human antibodies as next generation therapeutics”. *Current opinion in chemical biology* 5.4 (2001). (Cit. on pp. 5, 20).

[Dima2011] S. Dimartino, C. Boi, and G. C. Sarti. “A validated model for the simulation of protein purification through affinity membrane chromatography”. *Journal of Chromatography A* 1218.13 (2011). (Cit. on pp. 41, 71).

[Djab1989] M. Djabourov et al. “Small-angle x-ray scattering characterization of agarose sols and gels”. *Macromolecules* 22.1 (1989). (Cit. on pp. 22, 23, 85).

[Dubi1988] P. L. Dubin. *Aqueous size-exclusion chromatography*. Elsevier, 1988 (cit. on p. 58).

[Dubr1995] T. Dubrovsky et al. “Immunological activity of IgG Langmuir films oriented by protein A sublayer”. *Sensors and Actuators B: Chemical* 23.1 (1995). (Cit. on p. 68).

[Ecke2015] Ecker et al., ed. *The therapeutic monoclonal antibody market*. Vol. 1. Taylor & Francis, 2015 (cit. on p. 19).

[Emig2017] G. Emig and E. Klemm. *Chemische Reaktionstechnik*. Springer, 2017 (cit. on pp. 162, 163).

[Ever1972] D. H. Everett. “Manual of symbols and terminology for physicochemical quantities and units, appendix II: Definitions, terminology and symbols in colloid and surface chemistry”. *Pure and Applied Chemistry* 31.4 (1972). (Cit. on p. 15).

[Fran2011] P. Francis, E. von Lieres, and C. A. Haynes. “Zonal rate model for stacked membrane chromatography. I: Characterizing solute dispersion under flow-through conditions”. *Journal of Chromatography A* 1218.31 (2011). (Cit. on p. 43).

[Fran2012] P. Francis, E. von Lieres, and C. Haynes. “Zonal rate model for stacked membrane chromatography part II: Characterizing ion–exchange membrane chromatography under protein retention conditions”. *Biotechnology and bioengineering* 109.3 (2012). (Cit. on p. 43).

[Frer2008] C. Frerick et al. “Simulation of a human serum albumin downstream process incorporating ion-exchange membrane adsorbers”. *Chemical Engineering and Processing: Process Intensification* 47.7 (2008). (Cit. on p. 41).

[GE H2008] GE Healthcare. “Instructions 11-0026-01 AC Affinitiy Chromatography”. (2008). (Cit. on p. 55).

[GE H2017] GE Healthcare. “MabSelect PrismA”. KA553200917DF (2017). (Cit. on p. 27).

[Geba1997] K. H. Gebauer, J. Thömmes, and Kula. “Breakthrough performance of high-capacity membrane adsorbers in protein chromatography”. *Chemical engineering science* 52.3 (1997). (Cit. on p. 41).

[Ghos2006] R. Ghosh and T. Wong. “Effect of module design on the efficiency of membrane chromatographic separation processes”. *Journal of membrane science* 281.1-2 (2006). (Cit. on pp. 30, 34).

[Ghos2014] P. Ghosh et al. “Zonal rate model for axial and radial flow membrane chromatography, part II: Model–based scale–up”. *Biotechnology and bioengineering* 111.8 (2014). (Cit. on p. 43).

[Gidd1968] J. C. Giddings et al. “Statistical theory for the equilibrium distribution of rigid molecules in inert porous networks. Exclusion chromatography”. *The Journal of Physical Chemistry* 72.13 (1968). (Cit. on p. 171).

[Goed2006a] R. Goedecke. *Fluidverfahrenstechnik: Grundlagen, Methodik, Technik, Praxis*. John Wiley & Sons, 2006 (cit. on pp. 15, 155).

[Goed2006b] R. Goedecke. *Fluidverfahrenstechnik: Grundlagen, Methodik, Technik, Praxis*. John Wiley & Sons, 2006 (cit. on p. 38).

[Gorb1988] A. A. Gorbunov, L. Y. Solovyova, and V. A. Pasechnik. “Fundamentals of the theory and practice of polymer gel-permeation chromatography as a method of chromatographic porosimetry”. *Journal of Chromatography A* 448 (1988). (Cit. on p. 58).

[Gott2009] U. Gottschalk. *Process scale purification of antibodies*. Vol. 577.27 PRO. Wiley Online Library, 2009 (cit. on pp. 5, 20).

[Grga2006] E. V. L. Grgacic and D. A. Anderson. “Virus-like particles: passport to immune recognition”. *Methods* 40.1 (2006). (Cit. on p. 20).

[Guen1992] J.-M. Guenet. *Thermoreversible gelation of polymers and biopolymers*. Academic Press London, 1992 (cit. on p. 23).

[Guio1994] G. Guiochon, S. Golshan-Shirazi, and Am Katti. “Fundamentals of nonlinear and preparative chromatography”. In*Fundamentals of nonlinear and preparative chromatography*. Ed. by G. Guiochon and S. Golshan-Shirazi. Academic Press, 1994. (Cit. on pp. 24, 37, 38, 41, 42, 58).

[Gust1996] P.-E. Gustavsson and P.-O. Larsson. “Superporous agarose, a new material for chromatography”. *Journal of Chromatography A* 734.2 (1996). (Cit. on p. 28).

[Gust1998] P.-E. Gustavsson, ed. *Superporous agarose: a new materal for chromatography*. 1998 (cit. on p. 28).

[Hage1996] L. Hagel, M. Östberg, and T. Andersson. “Apparent pore size distributions of chromatography media”. *Journal of Chromatography A* 743.1 (1996). (Cit. on pp. 57, 81).

[Hage2020] F. Hagemann et al. “Modeling hindered diffusion of antibodies in agarose beads considering pore size reduction due to adsorption”. *Journal of Chromatography A* (2020). (Cit. on p. 66).

[Hahn2000] R. Hahn and A. Jungbauer. “Peak broadening in protein chromatography with monoliths at very fast separations”. *Analytical chemistry* 72.20 (2000). (Cit. on p. 28).

[Hahn2005] R. Hahn et al. “Comparison of protein A affinity sorbents: II. Mass transfer properties”. *Journal of Chromatography A* 1093.1-2 (2005). (Cit. on p. 27).

[Ham2004] J.-.-H. Ham and B. Platzer. “Semi–Empirical Equations for the Residence Time Distributions in Disperse Systems–Part 1: Continuous Phase”. *Chemical Engineering & Technology: Industrial Chemistry–Plant Equipment–Process Engineering–Biotechnology* 27.11 (2004). (Cit. on pp. xx, xxi, 34, 62, 74, 163, 177).

[Horv1983] G. Horváth and K. Kawazoe. “Method for the calculation of effective pore size distribution in molecular sieve carbon”. *Journal of Chemical Engineering of Japan* 16.6 (1983). (Cit. on p. 171).

[Hunt2000] A. K. Hunter and G. Carta. “Protein adsorption on novel acrylamido-based polymeric ion exchangers: II. Adsorption rates and column behavior”. *Journal of Chromatography A* 897.1 (2000). (Cit. on p. 40).

[Iber1999] G. Iberer, R. Hahn, and Am Jungbauer. “Monoliths as stationary phases for separating biopolymers: fourth-generation chromatography sorbents”. *LC GC* 17.11 (1999). (Cit. on p. 28).

[Jian2011] Z. Jiang et al. “Purification and immunogenicity study of human papillomavirus 58 virus-like particles expressed in Pichia pastoris”. *Protein expression and purification* 80.2 (2011). (Cit. on p. 28).

[Jin1994] X. Jin, J. Talbot, and N.-.-H. L. Wang. “Analysis of steric hindrance effects on adsorption kinetics and equilibria”. *AIChE journal* 40.10 (1994). (Cit. on p. 71).

[Joha2002] I. Johansson. “IGG separation medium”. US6,399,750 B1. 2002 (cit. on p. 55).

[John1995] E. M. Johnson et al. “Diffusion and partitioning of proteins in charged agarose gels”. *Biophysical journal* 68.4 (1995). (Cit. on p. 67).

[John1996] E. M. Johnson et al. “Hindered diffusion in agarose gels: Test of effective medium model”. *Biophysical journal* 70.2 (1996). (Cit. on p. 37).

[Jung1996] A. Jungbauer. “Insights into the chromatography of proteins provided by mathematical modeling”. *Current Opinion in Biotechnology* 7.2 (1996). (Cit. on pp. 40, 71).

[Jung2008] A. Jungbauer and R. Hahn. “Polymethacrylate monoliths for preparative and industrial separation of biomolecular assemblies”. *Journal of Chromatography A* 1184.1-2 (2008). (Cit. on pp. 27, 28).

[Kata1972] Kataoka and Yoshida,Hiroyuki, Ueyama,Koetsune. “Mass transfer in laminar region between liquid and packing material surface in the packed bed”. *Journal of Chemical Engineering of Japan* 5.2 (1972). (Cit. on p. 38).

[Korn2000] G. A. Korn and T. M. Korn. *Mathematical handbook for scientists and engineers: definitions, theorems, and formulas for reference and review*. Courier Corporation, 2000 (cit. on p. 172).

[Lamb2016] J. Lambour et al. “Converting monoclonal antibody-based immunotherapies from passive to active: Bringing immune complexes into play”. *Emerging microbes & infections* 5.1 (2016). (Cit. on p. 19).

[Last1993] C. Lastoskie, K. E. Gubbins, and N. Quirke. “Pore size distribution analysis of microporous carbons: a density functional theory approach”. *The Journal of Physical Chemistry* 97.18 (1993). (Cit. on p. 171).

[Laur1967] T. C. Laurent. “Determination of the structure of agarose gels by gel chromatography”. *Biochimica et Biophysica Acta (BBA)-General Subjects* 136.2 (1967). (Cit. on pp. 22, 23, 67).

[Leve1999] O. Levenspiel. “Chemical reaction engineering”. *Industrial & engineering chemistry research* 38.11 (1999). (Cit. on pp. 164, 165).

[Leve2011] O. Levenspiel. *Tracer technology: Modeling the flow of fluids*. Springer Science & Business Media, 2011 (cit. on pp. 33, 164).

[Lewi1924] W. K. Lewis and W. G. Whitman. “Principles of gas absorption”. *Industrial & Engineering Chemistry* 16.12 (1924). (Cit. on pp. 165, 166).

[Ley2018] A. Ley et al. “Characterization of a macro porous polymer membrane at micron-scale by Confocal-Laser-Scanning Microscopy and 3D image analysis”. *Journal of membrane science* 564 (2018). (Cit. on pp. 54, 118).

[Li1998] Z. Li, Y. Gu, and T. Gu. “Mathematical modeling and scale-up of size-exclusion chromatography”. *Biochemical Engineering Journal* 2.2 (1998). (Cit. on p. 42).

[Lier2010a] E. v. Lieres and J. Andersson. “A fast and accurate solver for the general rate model of column liquid chromatography”. *Computers & chemical engineering* 34.8 (2010). (Cit. on p. 71).

[Lier2010b] E. v. Lieres, J. Wang, and M. Ulbricht. “Model based quantification of internal flow distributions from breakthrough curves of flat sheet membrane chromatography modules”. *Chemical Engineering & Technology: Industrial Chemistry–Plant Equipment–Process Engineering–Biotechnology* 33.6 (2010). (Cit. on pp. 41, 43, 61).

[Liu1994] H.-.-C. Liu and Fried. “Breakthrough of lysozyme through an affinity membrane of cellulose–cibacron blue”. *AIChE journal* 40.1 (1994). (Cit. on pp. 34, 105).

[Liu2014] J. K. H. Liu. “The history of monoclonal antibody development–progress, remaining challenges and future innovations”. *Annals of Medicine and Surgery* 3.4 (2014). (Cit. on p. 19).

[Maci2008] J. S. Maciel et al. “Structural characterization of cold extracted fraction of soluble sulfated polysaccharide from red seaweed Gracilaria birdiae”. *Carbohydrate Polymers* 71.4 (2008). (Cit. on pp. 22, 157).

[Mari2012] P. A. Marichal–Gallardo and M. M. Alvarez. “State–of–the–art in downstream processing of monoclonal antibodies: Process trends in design and validation”. *Biotechnology progress* 28.4 (2012). (Cit. on pp. 5, 20).

[Mart1941] A. J. P. Martin and R. L. M. Synge. “A new form of chromatogram employing two liquid phases: A theory of chromatography. 2. Application to the microdetermination of the higher monoamino-acids in proteins”. *Biochemical Journal* 35.12 (1941). (Cit. on pp. 18, 33, 165).

[Mc M2017] M. Mc Manaway. “Affinity chromatography devices”. WO2017014817A1. 2017 (cit. on p. 28).

[McCu2003] J. T. McCue et al. “Evaluation of protein-A chromatography media”. *Journal of Chromatography A* 989.1 (2003). (Cit. on p. 40).

[Mert2011] O. Merten and M. Al-Rubeai, eds. *Viral Vectors for Gene Therapy*. Springer, 2011 (cit. on p. 21).

[Moul2016] D. R. Mould and B. Meibohm. “Drug development of therapeutic monoclonal antibodies”. *BioDrugs* 30.4 (2016). (Cit. on p. 19).

[Ogst1973] A. G. Ogston, B. N. Preston, and J. D. Wells. “On the transport of compact particles through solutions of chain-polymers”. *Proceedings of the Royal Society of London. Series A. Mathematical and Physical Sciences* 333.1594 (1973). (Cit. on p. 36).

[Pabs2018] T. M. Pabst, J. Thai, and A. K. Hunter. “Evaluation of recent Protein A stationary phase innovations for capture of biotherapeutics”. *Journal of Chromatography A* 1554 (2018). (Cit. on pp. 25, 40, 58, 61, 68, 79, 80, 85, 86, 91, 119, 141, 142, 169).

[Pfau2013] E. L. Pfaunmiller et al. “Affinity monolith chromatography: a review of principles and recent analytical applications”. *Analytical and bioanalytical chemistry* 405.7 (2013). (Cit. on p. 28).

[Phel2007] J. P. Phelps, N. Dang, and L. Rasochova. “Inactivation and purification of cowpea mosaic virus-like particles displaying peptide antigens from Bacillus anthracis”. *Journal of virological methods* 141.2 (2007). (Cit. on p. 28).

[Plew2018] J. Plewka et al. “Antibody adsorption in protein–A affinity chromatography–in–situ measurement of nanoscale structure by small–angle X–ray scattering”. *Journal of separation science* (2018). (Cit. on pp. 23, 24).

[Plue1999] A. Pluen et al. “Diffusion of macromolecules in agarose gels: Comparison of linear and globular configurations”. *Biophysical journal* 77.1 (1999). (Cit. on pp. 37, 67).

[Renk1954] E. M. Renkin. “Filtration, diffusion, and molecular sieving through porous cellulose membranes”. *The Journal of general physiology* 38.2 (1954). (Cit. on p. 36).

[Rope1995] D. K. Roper and E. N. Lightfoot. “Estimating plate heights in stacked-membrane chromatography by flow reversal”. *Journal of Chromatography A* 702.1-2 (1995). (Cit. on p. 43).

[Samb1989] J. Sambrook, E. F. Fritsch, and T. Maniatis. *Molecular cloning: a laboratory manual*. Vol. Ed. 2. Cold spring harbor laboratory press, 1989 (cit. on p. 53).

[Sarf1997] F. T. Sarfert and M. R. Etzel. “Mass transfer limitations in protein separations using ion-exchange membranes”. *Journal of Chromatography A* 764.1 (1997). (Cit. on pp. 41, 71).

[Sart2020] Sartorius. “Internal communication at Sartorius Stedim Biotech GmbH”. 2020 (cit. on pp. 47, 65, 133, 143, 145).

[Satt1995] K. Sattler. *Thermische Trennverfahren: Grundlagen, Auslegung, Apperate. VCH-Verlagsgesellschaft*. 1995 (cit. on p. 15).

[Schm2006] H. Schmidt-Traub. *Preparative chromatography: Of fine chemicals and pharmaceutical agents*. John Wiley & Sons, 2006 (cit. on pp. 3, 15, 21, 22, 24, 40, 41, 57, 58).

[Shuk2007] A. A. Shukla et al. “Downstream processing of monoclonal antibodies—application of platform approaches”. *Journal of Chromatography B* 848.1 (2007). (Cit. on pp. 5, 20).

[Step2019] P. Stephan et al. *VDI-Wärmeatlas*. Springer-Verlag, 2019 (cit. on p. 178).

[Suen1992] S.-Y. Suen and M. R. Etzel. “A mathematical analysis of affinity membrane bioseparations”. *Chemical engineering science* 47.6 (1992). (Cit. on pp. 34, 41).

[Tall2002] U. Tallarek, F. C. Leinweber, and A. Seidel–Morgenstern. “Fluid dynamics in monolithic adsorbents: phenomenological approach to equivalent particle dimensions”. *Chemical Engineering & Technology: Industrial Chemistry–Plant Equipment–Process Engineering–Biotechnology* 25.12 (2002). (Cit. on p. 28).

[Tatá2008] I. Tatárová et al. “Characterization of pore structure of chromatographic adsorbents employed in separation of monoclonal antibodies using size-exclusion techniques”. *Journal of Chromatography A* 1193.1-2 (2008). (Cit. on pp. 171, 172).

[Tatá2009] I. Tatárová et al. “Characterization of pore structure of a strong anion-exchange membrane adsorbent under different buffer and salt concentration conditions”. *Journal of Chromatography A* 1216.6 (2009). (Cit. on p. 30).

[Tayl1953] G. I. Taylor. “Dispersion of soluble matter in solvent flowing slowly through a tube”. *Proceedings of the Royal Society of London. Series A. Mathematical and Physical Sciences* 219.1137 (1953). (Cit. on p. 163).

[Teje1999] A. Tejeda et al. “Optimal design of affinity membrane chromatographic columns”. *Journal of Chromatography A* 830.2 (1999). (Cit. on p. 30).

[Vaňk2010] K. Vaňková, P. Ačai, and M. Polakovič. “Modelling of fixed-bed adsorption of mono-, di-, and fructooligosaccharides on a cation-exchange resin”. *Biochemical Engineering Journal* 49.1 (2010). (Cit. on p. 40).

[Walt2000] W. Walther and U. Stein. “Viral vectors for gene transfer”. *Drugs* 60.2 (2000). (Cit. on p. 21).

[Wash1921] E. W. Washburn. “The dynamics of capillary flow”. *Physical review* 17.3 (1921). (Cit. on p. 171).

[Wils1966] E. J. Wilson and C. J. Geankoplis. “Liquid mass transfer at very low Reynolds numbers in packed beds”. *Industrial & Engineering Chemistry Fundamentals* 5.1 (1966). (Cit. on p. 38).

[WL G2017] W.L. Gore & Associates, Inc. “Gore Protein Capture Device with Potein A: For Drug Discovery Applications”. (2017). (Cit. on p. 27).

[Yang1999] H. Yang, M. Bitzer, and M. R. Etzel. “Analysis of protein purification using ion-exchange membranes”. *Industrial & engineering chemistry research* 38.10 (1999). (Cit. on pp. 41, 43).

[Yau1980] W. W. Yau and D. D. Bly, eds. *Effect of solute shape or conformation in size exclusion chromatography*. American Chemical Society, 1980 (cit. on p. 58).

[Youn1980] M. E. Young, P. A. Carroad, and R. L. Bell. “Estimation of diffusion coefficients of proteins”. *Biotechnology and bioengineering* 22.5 (1980). (Cit. on p. 35).

[Yu2014] M. Yu et al. “Improving stability of virus-like particles by ion-exchange chromatographic supports with large pore size: Advantages of gigaporous media beyond enhanced binding capacity”. *Journal of Chromatography A* 1331 (2014). (Cit. on pp. 25, 40).